Aus dem Institut für Aktive Polymere Helmholtz-Zentrum Hereon

Study on manufacturing of multifunctional bilayer systems

zur Erlangung des akademischen Grades
"Doctor rerum naturalium"
(Dr. rer. nat.)
in der Wissenschaftsdisziplin
„Materialien in den Lebenswissenschaften“

Kumulative Dissertation

eingereicht an der
Mathematisch-Naturwissenschaftlichen Fakultät der Universität Potsdam

von
Mersa Saatchi
aus Teheran, Iran

2023, Potsdam

Supervisors:
PD Dr. Axel Neffe, Universität Potsdam
Prof. Dr. Svetlana Santer, Universität Potsdam

Reviewers:
Prof. Dr. Sabine Beuermann, Clausthal University of Technology
Prof. Dr. Friedrich Jung, Brandenburg University of Technology

Date of final exam: 17.07.2023

https://doi.org/10.25932/publishup-60196
https://nbn-resolving.org/urn:nbn:de:kobv:517-opus4-601968

Statement of Originality

I, Mersa Saatchi, formally submit the dissertation entitled “Study on manufacturing of multifunctional bilayer systems“ to the Department of Mathematics and Natural Sciences, University of Potsdam, Germany, for acquirement of the academic degree of Doctor of Natural Sciences (Dr. rer. nat.) in Materials for life science.

I, hereby declare that the work presented in this dissertation is my own original work based on the research carried out at Helmholtz-Zentrum Geesthacht, Institute of Active Polymers in Teltow, Germany, from Jun 2011 to Jun 2015 under the supervision of Prof. Dr. Andreas Lendlein. The thesis was written in 2022 under supervision of PD Dr. Axel Neffe.

To the best of my knowledge and belief, it contains no material previously published or written by another person, except were due reference is made in the thesis itself. Neither the dissertation, nor any section, has been previously submitted for a degree or other qualification to any other university or institution. Any contribution made to the research by other, with whom I worked at Helmholtz-Zentrum Geesthacht or elsewhere, is explicitly acknowledged in the thesis.

Mersa Saatchi

Acknowledgements

The practical work as well as the writing and publishing of 3 papers presented in this thesis was carried out in 2011-2015 at the Institute of Biomaterial Science, Helmholtz-Zentrum Geesthacht and financially supported by German federal ministry of education and research under a grant of collaboration Tianjin University–Helmholtz-Zentrum Geesthacht. (No. Grant. 0314596).

I would like to thank Prof. Dr. Andreas Lendlein for accepting me at HZG, for introducing me to the world of biomaterial science, for his guidance while doing research and writing publications. I would also like to acknowledge my department head Dr. Marc Behl for his suggestions and advices during my Ph.D. time

For personal reasons, I could only finish writing of the thesis and the fourth manuscript in 2022. In this regard, my whole gratitude goes to PD Dr. Axel Neffe for supporting me with a new opportunity to finish my Ph.D., as well as for his fabulous supervision in writing my thesis. The completion of my Ph.D. would have never been possible without his support. In addition, I would like to appreciate the presence of Dr. Karola Lützow during the withdrawal and restarted again encouraging me to finish this chapter of my life.

A special thank goes to Dr. Diana Tartakowska, Dr. Mohsen Dabestani and Dr. Maria Balk for encouraging me to overcome my doubts, to rewrite my thesis and to finalize my Ph.D. after 7 years of gap.

I would like to express my gratitude to the persons who were teaching me, supporting me, assisting me or were simply present during those years, Dr. Ulrich Nöchel, Robert Jezorski, Mario Rettschlag, Mario Zahn, Nicole Schneider, Susanne Schwanz, Dr. Hans-Jürgen Kosmella for the great atmosphere in the lab, and the BAP group in general, Dr. Thomas Weigel, Yvonne Pieper, Manuela Keller, Dr. Liang Fang, Dr. Victor Izraylit and Dr. Yue Liu.

I appreciate Dr. Michael Schroeter for his kind guidance to complete all the student tasks during my Ph.D. study and also Dr. Karolin Schmälzlin for her important assistance concerning the publication issues.

The assistance provided by Mrs. Vera Milkereit regarding my administration issues such as visa is greatly appreciated.

I would like to appreciate MacroBio Graduate School for funding my exchange lab in France.

I would like to extend my gratitude to Prof. Billon and Dr. Combeaud at CEMEF campus of Paris Tech for providing me equipment for my project in France.

Besides, I never forget the strong support of my colleagues during my four years in Teltow: Thank you Lucile, Steffi, Christian, Simi, Maria, Candy, Mira, Pengfei, Wan, Sho, Magda, Tilman, Li, Fabian, Harshal, Konstanze, Stefan, Ehsan, Marián, Tim and Timm, Julia, Yaser, Farhan and all international students who showed me their culture in those time.

Furthermore, I would like to acknowledge Dr. Diana Tartakowka and Dr. Marco Müller for their warm support in my settling down in Berlin in 2011.

I owe my deepest gratitude to my mother Dr. Fereshteh Navadeh, my father Darioush Saatchi and my brother Daniel Saatchi for their sincere love encouraging me to make my dreams come true.

Content

Abstract

Layered structures are ubiquitous in nature and industrial products, in which individual layers could have different mechanical/thermal properties and functions independently contributing to the performance of the whole layered structure for their relevant application. Tuning each layer affects the performance of the whole layered system.

Pores are utilized in various disciplines, where low density, but large surfaces are demanded. Besides, open and interconnected pores would act as a transferring channel for guest chemical molecules. The shape of pores influences compression behavior of the material. Moreover, introducing pores decreases the density and subsequently the mechanical strength. To maintain defined mechanical strength under various stress, porous structure can be reinforced by adding reinforcement agent such as fiber, filler or layered structure to bear the mechanical stress on demanded application.

In this context, this thesis aimed to generate new functions in bilayer systems by combining layers having different moduli and/or porosity, and to develop suitable processing techniques to access these structures.

Manufacturing processes of layered structures employ often organic solvents mostly causing environmental pollution. In this regard, the studied bilayer structures here were manufactured by processes free of organic solvents.

In this thesis, three bilayer systems were studied to answer the individual questions.

First, while various methods of introducing pores in melt-phase are reported for one-layer constructs with simple geometry, can such methods be applied to a bilayer structure, giving two porous layers?

This was addressed with Bilayer System 1. Two porous layers were obtained from melt-blending of two different polyurethanes (PU) and polyvinyl alcohol (PVA) in a co-continuous phase followed by sequential injection molding and leaching the PVA phase in deionized water. A porosity of 50 ± 5% with a high interconnectivity was obtained, in which the pore sizes in both layers ranged from 1 µm to 100 µm with an average of 22 µm in both layers. The obtained pores were tailored by applying an annealing treatment at relevant high temperatures of 110 °C and 130 °C, which allowed the porosity to be kept constant. The disadvantage of this system is that a

maximum of 50% porosity could be reached and removal of leaching material in the weld line section of both layers is not guaranteed. Such a construct serves as a model for bilayer porous structure for determining structure-property relationships with respect to the pore size, porosity and mechanical properties of each layer. This fabrication method is also applicable to complex geometries by designing a relevant mold for injection molding.

Secondly, utilizing $scCO_2$ foaming process at elevated temperature and pressure is considered as a green manufacturing process. Employing this method as a post-treatment can alter the history orientation of polymer chains created by previous fabrication methods. Can a bilayer structure be fabricated by a combination of sequential injection molding and $scCO_2$ foaming process, in which a porous layer is supported by a compact layer?

Such a construct (Bilayer System 2) was generated by sequential injection molding of a PCL ($T_m \approx 58$ °C) layer and a PLLA ($T_g \approx 58$ °C) layer. Soaking this structure in the autoclave with $scCO_2$ at $T = 45$ °C and $P = 100$ bar led to the selective foaming of PCL with a porosity of 80%, while the PLA layer was kept compact. The $scCO_2$ autoclave led to the formation of a porous core and skin layer of the PCL, however, the degree of crystallinity of PLLA layer increased from 0 to 50% at the defined temperature and pressure. The microcellular structure of PCL as well as the degree of crystallinity of PLLA were controlled by increasing soaking time.

Thirdly, wrinkles on surfaces in micro/nano scale alter the properties, which are surface-related. Wrinkles are formed on a surface of a bilayer structure having a compliant substrate and a stiff thin film. However, the reported wrinkles were not reversible. Moreover, dynamic wrinkles in nano and micro scale have numerous examples in nature such as gecko foot hair offering reversible adhesion and an ability of lotus leaves for self-cleaning altering hydrophobicity of the surface. It was envisioned to imitate this biomimetic function on the bilayer structure, where self-assembly on/off patterns would be realized on the surface of this construct.

This was realized in Bilayer System 3, consisting of a crosslinked poly[ethylene-*co*-(vinyl acetate)] (cPEVA) substrate and a 10 nm gold metal film, in which a reversible bidirectional shape memory effect (rbSME) was encoded into the substrate before deposition of the gold film. In stress-free thermal cycles, parallel wrinkles ($\lambda = 1.5 \pm 0.2$ µm and $A = 190 \pm 10$ nm) appeared at 60 °C and disappeared at 25 °C. Employing this concept on a pre-patterned surface led to the formation of self-assembly multi-patterns, where at 25 °C diamond-like patterns appeared, which transformed into parallel wrinkles at 60 °C. The potential application of such a function can be smart surfaces in different disciplines. To exploit such a bilayer structure in biomedical applications, a substrate showing rbSME around physiological temperature is required. To do so, copolymer networks from Oligo(ε-caprolactone) and *n*-butyl acrylate were also synthesized, which exhibited rbSME between 20 °C and 37 °C.

In summary, developing layered constructs having different properties/functions in the individual layer or exhibiting a new function as the consequence of layered structure can give novel insight for designing layered constructs in various disciplines such as packaging and transport industry, aerospace industry and health technology.

Zusammenfassung

Schichtstrukturen sind in der Natur und in Industrieprodukten allgegenwärtig, wobei die einzelnen Schichten unterschiedliche mechanische/thermische Eigenschaften und Funktionen haben können, die unabhängig voneinander zur Leistungsfähigkeit der gesamten Schichtstruktur für die jeweilige Anwendung beitragen. Die individuelle Abstimmung jeder einzelnen Schicht wirkt sich auf die Leistungsfähigkeit des gesamten Schichtsystems aus.

Poren werden in verschiedenen Bereichen eingesetzt, in denen eine geringe Dichte, aber eine große Oberfläche erforderlich ist. Außerdem können offene und miteinander verbundene Poren als Übertragungskanal für chemische Gast-Moleküle dienen. Die Form der Poren beeinflusst das Kompressionsverhalten des Materials. Außerdem verringert sich durch das Einbringen von Poren die Dichte und damit die mechanische Festigkeit. Um eine definierte mechanische Festigkeit unter verschiedenen Belastungen aufrechtzuerhalten, kann eine poröse Struktur durch Zugabe von Verstärkungsmitteln wie Fasern, Füllstoffen oder einer Schichtstruktur verstärkt werden, um die mechanische Belastung bei der geforderten Anwendung zu gewährleisten.

In diesem Zusammenhang zielte diese Arbeit darauf ab, neue Funktionen in zweischichtigen Systemen durch die Kombination von Schichten mit unterschiedlichen Modulen und/oder Porosität zu erzeugen und geeignete Verarbeitungstechniken zu entwickeln, um diese Strukturen zu erreichen.

Bei der Herstellung von Schichtstrukturen werden häufig organische Lösungsmittel verwendet, die meist eine Umweltbelastung darstellen. Daher wurden die hier untersuchten Doppelschichtstrukturen mit Verfahren hergestellt, die frei von organischen Lösungsmitteln sind.

In dieser Arbeit wurden drei Doppelschichtsysteme untersucht, um die einzelnen Fragen zu beantworten.

Erstens: Während verschiedene Methoden zur Einführung von Poren in der Schmelzphase für einschichtige Konstruktionen mit einfacher Geometrie bekannt sind, stellt sich die Frage, ob solche Methoden sich auf eine zweischichtige Struktur anwenden lassen und somit zwei unterschiedlich poröse Schichten ergibt?

Dies wurde mit dem Zweischichtsystem 1 untersucht. Zwei poröse Schichten wurden durch das Mischen in der Schmelze von zwei verschiedenen Polyurethanen (PU) und Polyvinylalkohol (PVA) in einer co-kontinuierlichen Phase erhalten. Es folgte sequentielles Spritzgießen und das Entfernen der PVA-Phase durch „Leaching“ in entionisiertem Wasser. Es wurde eine Porosität von 50 ± 5 % mit einer hohen Interkonnektivität erzielt, wobei die Porengrößen in beiden Schichten zwischen 1 µm und 100 µm lagen, mit einem Durchschnittswert von 22 µm in beiden Schichten. Die erhaltenen Poren wurden durch Tempern bei entsprechend hohen Temperaturen von 110 °C und 130 °C optimiert, wodurch die Porosität konstant gehalten werden konnte. Der Nachteil dieses Systems besteht darin, dass eine maximale Porosität von 50 % erreicht werden konnte und dass die Entfernung durch „Leaching“ des PVAs im Schweißnahtbereich beider Schichten nicht gewährleistet ist. Ein solches Konstrukt dient als Modell für eine zweischichtige poröse Struktur zur Bestimmung der Struktur-Eigenschafts-Beziehungen in Bezug auf Porengröße, Porosität und mechanische Eigenschaften der einzelnen Schichten. Diese Herstellungsmethode ist auch auf komplexe Geometrien anwendbar, es muss lediglich eine entsprechende Form für das Spritzgießen entworfen werden.

Zweitens: die Verwendung des scCO$_2$-Schäumungsverfahrens bei erhöhter Temperatur und erhöhtem Druck wird als umweltfreundlicher Herstellungsprozess betrachtet. Durch den Einsatz dieser Methode als Nachbehandlung kann die Historie der Ausrichtung der Polymerketten, die durch frühere Herstellungsmethoden entstanden ist, verändert werden. Kann eine zweischichtige Struktur durch eine Kombination aus sequentiellem Spritzgießen und scCO$_2$-Schäumverfahren hergestellt werden, bei der eine poröse Schicht von einer kompakten Schicht getragen wird?

Ein solches Konstrukt (Bilayer System 2) wurde durch sequentielles Spritzgießen einer PCL-Schicht ($T_m \approx 58$ °C) und einer PLLA-Schicht ($T_g \approx 58$ °C) erzeugt. Das Einweichen dieser Struktur in scCO$_2$ im Autoklaven bei $T = 45$ °C und $P = 100$ bar führte zum selektiven Aufschäumen von PCL mit einer Porosität von 80%, während die PLA-Schicht unverschäumt blieb. Die Behandlung im scCO$_2$-Autoklav führte zur Bildung einer porösen Kern- und Hautschicht des PCL, während der Kristallinitätsgrad der PLLA-Schicht bei der definierten Temperatur und dem definierten Druck von 0 auf 50 % anstieg. Die mikrozelluläre Struktur von PCL sowie der Kristallinitätsgrad von PLLA wurden durch die Erhöhung der Einweichzeit gesteuert.

Drittens verändern Falten auf Oberflächen im Mikro-/Nanomaßstab die Eigenschaften, die mit der Oberfläche zusammenhängen. Falten bilden sich auf der Oberfläche einer zweischichtigen Struktur mit einem nachgiebigen Substrat und einem steifen dünnen Film. Die Falten waren jedoch nicht reversibel. Darüber hinaus gibt es in der Natur zahlreiche Beispiele für dynamische Falten im Nano- und Mikromaßstab, wie z. B. Gecko-Fußhaare, die eine reversible Adhäsion ermöglichen, und die Fähigkeit von Lotusblättern, sich selbst zu reinigen, indem sie die Hydrophobizität der Oberfläche verändern. Diese biomimetische Funktion sollte auf der Doppelschichtstruktur nachgeahmt werden, wobei auf der Oberfläche dieses Konstrukts selbstorganisierende On/Off-Muster realisiert werden sollten.

Dies wurde in dem Bilayer-System 3 realisiert, das aus einem vernetzten Poly[ethylen-*co*-(vinylacetat)]-Substrat (cPEVA) und einer 10 nm dicken Goldschicht besteht, wobei ein reversibler bidirektionaler Formgedächtniseffekt (rbSME) in das Substrat vor der Beschichtung mit Gold kodiert wurde. In spannungsfreien thermischen Zyklen traten parallele Falten ($\lambda = 1{,}5 \pm 0{,}2$ µm und $A = 190 \pm 10$ nm) bei 60 °C auf und verschwanden bei 25 °C. Die Anwendung dieses Konzepts auf eine vorgemusterte Oberfläche führte zur Bildung von selbstorganisierenden Mehrfachmustern, wobei bei 25 °C diamantartige Muster erschienen, die sich bei 60 °C in parallele Falten verwandelten. Die potenzielle Anwendung einer solchen Funktion können intelligente Oberflächen in verschiedenen Disziplinen sein. Um eine solche Doppelschichtstruktur in biomedizinischen Anwendungen zu nutzen, ist ein Substrat erforderlich, das rbSME bei physiologischer Temperatur zeigt. Zu diesem Zweck wurden auch Copolymer-Netzwerke aus Oligo(ε-Caprolacton) und n-Butylacrylat synthetisiert, die rbSME zwischen 20 °C und 37 °C aufwiesen.

Zusammenfassend kann gesagt werden, dass die Entwicklung geschichteter Konstrukte mit unterschiedlichen Eigenschaften/Funktionen in den einzelnen Schichten oder mit einer neuen Funktion als Folge der geschichteten Struktur neue Erkenntnisse für den Entwurf geschichteter Konstrukte in verschiedenen Disziplinen wie der Verpackungs- und Transportindustrie, der Luft- und Raumfahrtindustrie und der Gesundheitstechnologie liefern kann.

List of Abbreviations

°	Degree of angles
°C	Degree Celsius
A	Amplitude of wrinkles
AD	Actuator domains
AFM	Atomic force microscopy
BA	*n*-butyl acrylate
CIE	Crystallization-induced elongation
cPEVA	Crosslinked poly[ethylene-*co*-(vinyl acetate)]
2D	Two-dimension
2DFFT	2D-fast Fourier transformation
3D	Three-dimension
DMTA	Dynamic mechanical thermal analysis
DOC	Degree of crystallinity
DSC	Differential scanning calorimetry
E	Young's modulus
E_f	Young's modulus of film
E_s	Young's modulus of substrate
E_flex	Flexural or bending modulus
E_comp	Compressive elastic modulus
f	film

g	Gram
G	Gel content
GPC	Gel permission chromatography
h	Hour
h_f	Thickness of film
h$\bar{M}_\mathrm{n}$	Higher number average molar mass
^{1}H-NMR	Proton nuclear magnetic resonance
IPN	Interpenetrating polymer network
kV	Kilovolts
l$\bar{M}_\mathrm{n}$	Lower number average molar mass
M_c	Molar mass of network chain segment
$\bar{M}_\mathrm{n}$	Number average molar mass
$\bar{M}_\mathrm{w}$	Weight average molar mass
mA	Milliampere
min	Minute
mm	Millimeter
MD	Machine direction
MIC	Melting-induced contraction
MIM	Microcellular injection molding
MMA	Methyl methacrylate
MPa	Mega Pascal
N	Newton
N	Speed of screw

n-BA	*n*-butyl acrylate
OCL	Oligo(ε-caprolactone)
OCL-BA	Crosslinked networks of oligo (ε-caprolactone) and *n*-butyl acrylate
PBAT	Poly[(butylene adipate)- *ran*-terephthalate]
PBS	Poly (butylene succinate)
PCL	Poly(ε-caprolactone)
PDMS	Poly(dimethylsiloxane)
PEG	Poly(ethylene glycol)
PEO	Polyethylene oxide
PLLA	Poly(*L*-lactide)
PLGA	Poly[(lactic)-*co*-(glycolic acid)]
PLW	Parallel wrinkles
PTHF	Polytetrahydrofuran
PU	Polyurethane
PVA	Polyvinyl alcohol
Q	Degree of swelling
Q_{ef}	Fixation efficiency
rbSME	Reversible bidirectional shape-memory effect
RMP	Reversible multi-patterns
$\mathrm{scCO_2}$	Supercritical carbon dioxide
SB	Simultaneous biaxial stretching
SEQB	Sequential biaxial stretching
SEM	Scanning electron microscopy

SME	Shape-memory effect
SMP	Shape-memory polymer
SGD	Shifting-geometry determining domain
SCF	Super critical fluid
t	Time
t_{r}	Recovery time
T	Temperature
T_{cyl}	Cylinder temperature
T_{fix}	Fixation temperature
T_{g}	Glass transition temperature
T_{prog}	Programming temperature
T_{m}	Melting temperature
$T_{\mathrm{m,\ onset}}$	Begin of melting transition
$T_{\mathrm{m,\ offset}}$	End of melting transition
ΔT_{m}	Melting temperature range
T_{mid}	temperature located between T_{sep} and $T_{\mathrm{m,\ onset}}$
T_{mold}	Temperature of mold
T_{sep}	Separation temperature
T_{high}	Programming temperature
T_{low}	Fixation temperature
T_{rec}	Recovery temperature
T_{sw}	Switching temperature
TD	Transverse direction

TSME	Triple shape-memory effect
US1	Uniaxial direction in X-axis
US2	Uniaxial direction in Y-axis
WAXS	Wide angle X-ray scattering
µCT	x-ray computed microtomography
µm	Micrometre
wt%	Weight percentage
σ	Stress
ε	Strain
ε_b	Elongation at break
$\varepsilon_{\mathrm{prog}}$	Programming strain
$\varepsilon_{\mathrm{rev}}$	Reversible strain
ε_{y}	Applied strain in Y-axis
λ	Wavelength of wrinkles
θ_{adv}	Advancing angle
θ_{rec}	Receding angle
ρ	Apparent density of compact layer
ρ_{p}	Apparent density of porous layer
υ_{c}	Cross-linking density

List of Figures

Chapter 1. Introduction

Layered Structure

Numerous examples of layered structures are arising in nature and man-made manufactured products, in which the layers can be in different sizes and geometries. The sandwich structure of composites (Figure 1) used in automobile and aerospace industries, laminated paperboard for packaging industries, coated tablets in pharmaceutical industries, and multi-layer tubes in pipe industries are some examples of man-made layered systems. Blood vessels[1], intervertebral discs[2], skin[3], and osteochondral tissue[4,5] are significant examples for biologically relevant layered structures that inspire biomimetic systems (Figure 1).

In all layered systems, each layer fulfills one demand of an object referring to its application or performance. Materials are selected or created by nature based on their mechanical and/or surface properties. Fibers or porous structures with their various morphologies are implemented in each layer to generate anisotropy of modulus or to decrease the density. As an example in nature, in a healthy blood vessel, the thin inner layer of the blood vessel called intima involves one layer of endothelial cells and subendothelial connective tissue and it does not affect highly the mechanical properties of the blood vessel as the whole structure. The cells of this layer allow blood and other fluids to flow smoothly and holds cells and fluid within the vessel lumen. In addition, this layer act as a biological filter for pathogens activating the biological function of inflammation.[6] The middle layer (the thickest layer) is composed of smooth muscle cells and elastic fibers and engages the vessel wall in the active contraction. This layer alters the diameter of the blood vessel to regulate the blood flow and blood pressure. The outer layer called adventitia consisted of collagen and elastin fibers. Loaded stress introduces crystallinity in collagen fibers exhibiting high Young's modulus (E) and stiffness. Figure 1 illustrates the different layered structures created by nature or industry having simple or more complicated geometry. [7]

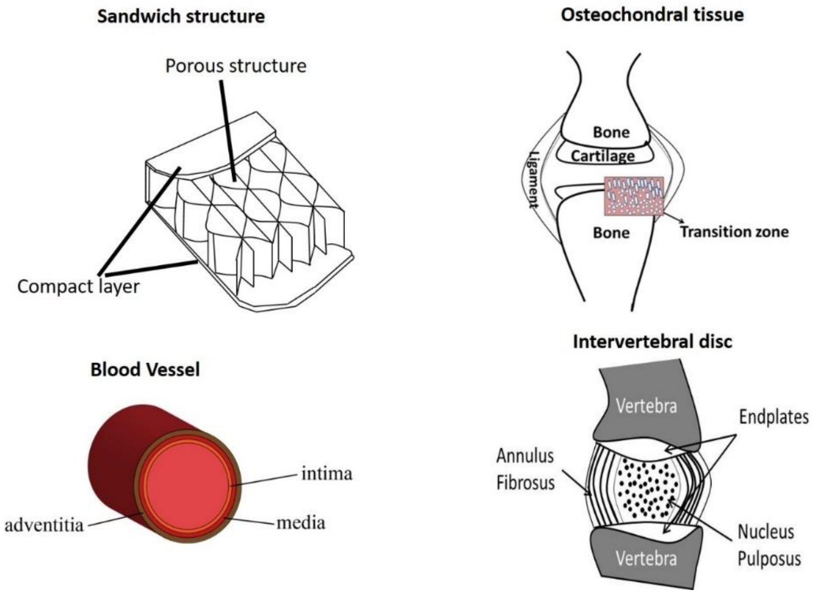

Figure 1.Simple schematic layered structure examples of a hand-made construct (sandwich structure) and natural layered structures in the human body.

Multifunctionality in Polymer Material

In materials science, the term multifunctionality[8-9] is perceived as a link among interdisciplinary fields, where different functions are implemented into the studied material based on demanded application. Multifunctionality has tremendous potential applications[10] employed in actuators, sensors, robotics, health technologies as well as metamaterials. Functionality is a performance or an encoded program implemented into materials by a combination of polymer processing technology and polymer morphology established either by chemical (molecular structure, phase morphology) or physical methods and it is disclosed in certain conditions or upon external stimuli (e.g. temperature, light, pH, solvent, electrical signals, chemical ionic concentration). Structural function, stimuli-sensitivity, controlled drug delivery, controlling guiding cellular behavior, and degradability can be addressed as different functions, which are employed in health technology and biomedical applications.

Integration of multifunctionality can be achieved by two approaches; an orthogonal arrangement of functions (Figure 2A), where each function is independent of the others. The challenge of a such array is that the introduction of each function would not interfere with the other one or erase the last established one. The second approach is called sequential coupled functions (Figure 2B), where the outcome of one function would act as a stimulus or a new environment (condition) for the next function and the performance of each function is displayed in a domino-wise manner. In both cases, employed functions should be compatible with defined applications.[9]

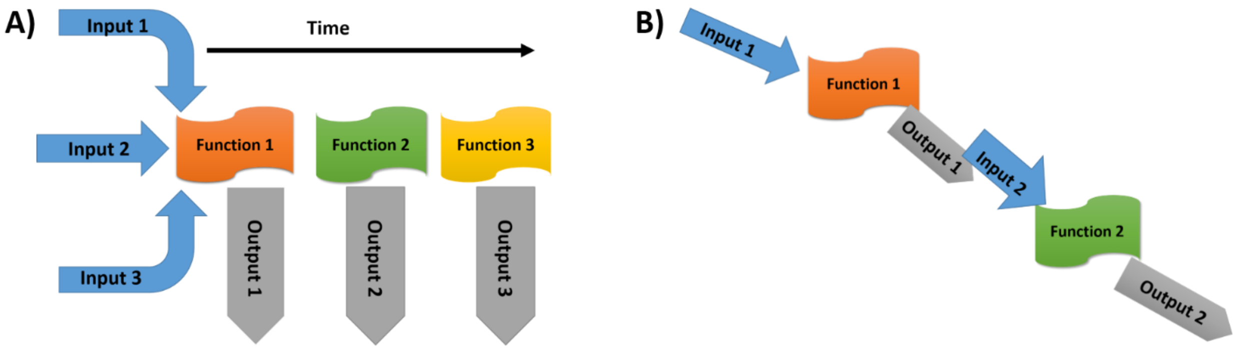

Figure 2. Multifunctionality can be designed either in A) Orthogonal , or B) Sequentially coupled functions array.

One example of the multifunction multilayer system is a multifunctional bilayer microstent used as a glaucoma drainage device[11]. Combination of a tubular structure (function), small orifices sizes for drainage function, drug release function, and hydrolytic degradation function were implemented in the bilayer tubular construct and can be classified as an orthogonal multifunction implement used in health technology.

The design and development of new multifunctional products should be integrated into a manufacturing process enabling scale-up and rapid prototyping, which is a big challenge[10]. This work is mainly focused on manufacturing methods of bilayer structures offering potential functions that can be scaled up into higher numbers and more complex geometries.

Porous structure

Introducing pores into the system either interconnected (open cell) or isolated (closed cell) gives the benefits of low density (direct ratio to porosity) and large specific surface to the material. Moreover, the presence of void or space within material acts as transferring channel for guest chemical molecules. This structure gives novel properties and can be applied in the mechanical, thermal, electrical, and acoustical fields. In regenerative medicine, the interconnected porous structure is a requirement for the formation of scaffolds as a guidance for stem cells.[12] Various methods have been developed for introducing pores into polymer material: solvent-casting, particulate leaching, gas foaming, fiber meshes, phase separation, melt molding and emulsion freeze-drying. New methods are also invented for complex structures, such as solid freeform fabrication (SFF), three-dimensional printing (3DP), stereolithography (SLA), fused deposition modeling (FDM), 3D plotter, and phase–change Jet printing. However, utilizing organic solvents in most of the mentioned methods is inevitable.[13]

Table 1 addresses the fabrication processes of multilayered porous constructs utilized as scaffolds in biomedical field, where in all researched processes, an organic solvent was applied. Having trace of organic solvent in a prototype for health technology should be avoided. To overcome this issue, using no organic solvent is the key to guaranteeing no residue solvent remains in the end products.

Table 1. An overview of manufacturing methods for preparation of multilayer scaffolds.

Methods	**References**
solvent casting, salt leaching method	Mikos et al., 1993[14]
freeze-drying, ice micro particles	Mao et al., 2003[15]
compression molding, particulate leaching, salt leaching	Ghosh et al., 2008[16]
electrospinning	Yunos et al., 2013[17]

Employing fabrication processes in a melt-phase of polymers such as injection molding and extrusion can be a solution to avoid organic solvent in the system. Introducing porosity in the melt-phase process is obtained by different approaches. Closed cells[18] are obtained via salt leaching[18,19] In 2020, different sizes of NaCl particles as porogen were added to the polymer melt of Poly [(*L*-lactide)-*co*-(ε-caprolactone)] (PLCL). This investigation revealed that the efficiency of NaCl as porogen is not dependent on the porogen particle size, but on the initial amount of blending.[19] Moreover, the interconnected pores in the melt-phase are obtained by a method, which was introduced by Washburn[20], in which two immiscible polymers were co-extruded. One of the polymer phases was soluble in water. Subsequent immersion of the blends in water caused the removal of the water-soluble phase in order to introduce voids into the system. In the case of the co-continuous phase, close to the inversion point, where two phases are fully continuous, interconnected pores can be formed after leaching. Nevertheless, the disadvantage of this process is achieving a maximum porosity of 50% - 60%. The shape of pores obtained from this method is characterized as cylindrical one, and it is completely different from other methods where the larger pores are interconnected through small gates. This approach was tested by using the poly(lactic-*co*-glycolic acid)/PVA[21], PLLA/Polystyrenes, and PCL/PEO.[22] Furthermore, the shape of interconnected pores via leaching method in the co-continuous phase could be varied from homogenous-isotropic structure to oriented and gradient co-continuous structure by altering the process parameters. This last mentioned structure, which was bio-inspired by nature in the bones and bamboos, was investigated in the morphology of a co-continues blend of PBAT/PBS investigated in 2021.[23]

Injection Molding Process

Injection molding is one of the high-speed, automated manufacturing processes dealing with the melt-phase of polymers offering the fabrication of scaling up and complex geometry articles in small or big sizes. This manufacturing process offers high repeatability and reliability in product manufacturing and can be applied to different materials. Layered structures having different materials can be formed either by co-continuous injection molding or over-injection moldings, in which the layers are connected either by a hot weld line or a cold weld line, respectively.[24] In general, a weld line is the outcome of an autohesion process established of direct self-bonding between 2 surfaces of distinct polymers in the closed surface under elevated temperature ($T > T_g$) and extended to the depth in a scale of 10 - 100 Ångstrom. Hence, estimation of the bonding strength in the welding mechanism is challenging to be evaluated by direct measurement.[25]

In addition, to avoid air bubbles in the final products produced by injection molding and extrusion (melt-based process), the granulates are generally dried prior to feeding into the hopper of the injection molding (Figure 3). In 2006, Haugen et al.[26] took benefits from moistures in granulars in a conventional injection molding process. The remaining water in the pellets along with 40% wt. of NaCl particles were used as a foaming agent and porogen, respectively.

Furthermore, there is also a versatile technology called microcellular injection molding[27] (MIM), which blends atmospheric gas (Nitrogen or CO_2) at high pressure (supercritical state) with the melt polymer to obtain a single homogenous phase of the polymer-gas solution while processing. This technique is also considered a green technology for introducing pores into the system using no organic solvent. Figure 3 compares the constructs of conventional and microcellular injection molding. The cycle of both types of machinery comprises plastic injection, filling and holding, cooling and solidification, and mold opening and ejection. Pores are generated by the MIM in the order of following stages: supercritical fluid (SCF) mixing and diffusion (presented in Figure 3C), cell nucleation, cell growth, and solidification, where all the last three phases are taken place after injection into the mold. These stages are the result of sudden dropping pressure at the nozzle, which leads to thermodynamic instability and consequently generation of the numerous microstructures. The obtained foam structures from this technique are in a way that cores are porous and outer layers are compact (porous core and skin-layer), which is called sandwich structure (Figure 1). The formation of the skin layer happens in the filling and cooling stage inside of the mold, where the cells have no time to grow as exposed to the low mold temperature[28]. In addition, the created cells are observed as round and distorted, which are formed in the cooling and filling stage, respectively. The obtained mean pore diameter of this technology is reported in the range of 2 - 10 µm.[28]

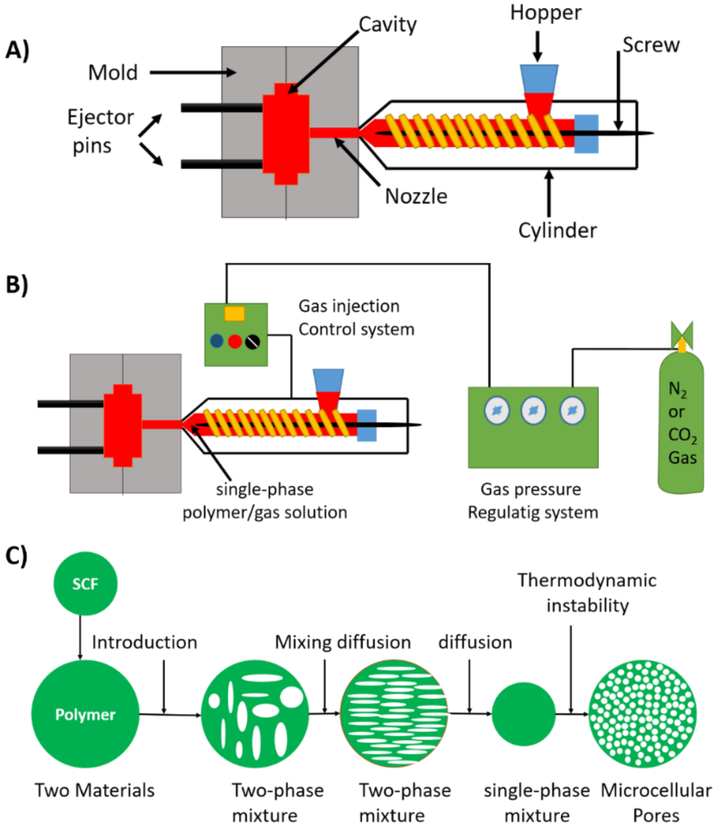

Figure 3. A) Schematic of a conventional injection molding. The mold can be designed for complex and different sizes of products. B) Schematic of a microcellular injection molding equipped with a supercritical gas source. The cycle of both processes consists of plastic injection, filling and holding, cooling and solidification, mold opening and ejection. C) Illustration presents the stages of diffusing gas in the supercritical state with the molten phase of polymer inside of the cylinder before injection to the mold cavity.

The combination of the aforementioned methods (salt leaching + polymer leaching and foaming agent) is also investigated[29-30], where a microcellular injection molding process was utilized, in which the foaming agent was applied during the formation process.

Another approach to introduce pores in the melt-phase of a polymer is adding a foaming agent as a post-treatment. Exploiting of supercritical carbon dioxide ($scCO_2$)[31] foaming process as the post-treatment step can be also addressed as a green-solvent process, where the usage of potentially toxic organic solvent is minimized. This method provides a porous core and skin surface and is based on the diffusion and solubility of $scCO_2$ in the polymer matrix lowering their tendency to chain rotation (plasticization), which yields a drop of glass transition temperature (T_g). Reduction of $scCO_2$ gas pressure to atmospheric one causes the decrease of solubility of the gas. This step leads to the generation of nucleus growing to form the pores and fixation of pores structure, which is taken place by rising of T_g as $scCO_2$ leaves the polymer. Hence, the pores are trapped in the material and cannot grow. By this method, a structure with a porous core and skin face is obtained. The materials used in this technique should be in an amorphous state.[32] The structure and homogeneity of pores are controlled by variation of the parameters such as pressure, temperature, soaking time, and the type of venting. The maximum obtained porosity can be reached up to 80%. Furthermore, interconnectivity and pore size of obtained foam from this approach are the functions of the rheological and crystallization behavior of the materials, which are correlated to the M_w and viscosity of the material at elevated temperature and pressure[33,34]. In addition, in 2020, a $scCO_2$ foaming process was applied on an immiscible blend of PCL and PLGA to investigate the effect of the immiscible phase on the obtained pore structure.[35]

Nevertheless, in all previous studies, a bilayer porous structure was not fabricated by leaching out one phase from co-continuous phase in convention injection molding.

Moreover, porosity decreases mechanical strength, which is correlated to the density of the pores, estimated by Equation 1.

Equation 1

$$E = E_0 \left({}^{\rho}/_{\rho_0} \right)$$

, where E and E_0 are the elastic moduli of the porous and compact layer and ρ and ρ_0 are the density of the pores and compact layer, respectively.

Having high porosity of more than 90% leads to very low mechanical strength. Improving the mechanical strength of porous products can be obtained by incorporating reinforcing agents, such as fillers[36], fibers[37], coating[38] and layered structure[39] concerning the end-use of the products, which are frequently utilized in the enhancement of the mechanical strength of products.

Porous structure with layered reinforcing agents can be obtained by inserting bilayer constructs into the $scCO_2$ autoclaves. However, the first formation process of bilayer constructs in melt-phase affects the formation of the porous structure of bilayer constructs, due to the history orientation of polymer chains in the first process, which can be exposed to the elevated temperature and pressure in the autoclave. In 2020, Sanz-Horta et al.[40] explored the fabrication of a screw-like scaffold generated by 3D printers and $scCO_2$ foaming process of multi-materials of PLLA in the center as an axis and PCL layers around the PLLA. In addition, Song et al.[41] also examined the bilayer membrane of PCL/ PLGA created by hot-pressure in an autoclave of $scCO_2$.

To my knowledge, the influence of the scCO2 process as post-treatment on a bilayer structure produced by injection molding was not studied. Injection molding offers flexibility in the complex design of products in layers in a fast automated way and applying the scCO2 process as post-treatment could be a potential green fabrication method to manufacture a selective foaming layer in layered products, while the MIM technique doesn't provide this benefit to layered structures.

The microcellular products can be utilized in various fields, such as packaging, transport, construction, oil-water separation and as scaffolds in tissue engineering. A layered structure as a reinforcing agent can be demanded as support in such applications, in which the product is bearing the bending or compression deformation.

Formation of wrinkles on the surface of a bilayer structure

Observing dynamic micro or nano patterns in nature such as gecko foot hair providing reversible adhesion[42], an ability of lotus leaves for self-cleaning by altering hydrophobicity[43], counterfeit traits in animals by tuning the transparency and coloration[44], fluid-drag reduction in shark skin[45], dynamic wrinkles on the human fingers skin after long exposure to the moisture and fading upon drying[46] are inspiring for scientists to explore and recreate the dynamic wrinkles on surfaces. The potential applications of such dynamic wrinkles are optical grating, stretchable electronics, smart adhesion[47], anti-fouling[48], anti-counterfeiting products[49], anti-glare film[46], smart windows for energy saving in architecture and vehicle application and triboelectric nanogenerator (TENG), where micro/nano patterns on surface increase charge density and performance.[50] Wrinkles can also be utilized in biomedical field. In 2022, wrinkles on gold (Au) film on Poly(dimethylsiloxane) (PDMS) substrate was employed for aligning cardiac tissue and enhancing contractile properties, where wrinkles of Au surface enhanced the electrical conductivity of cell to cell interaction.[51]

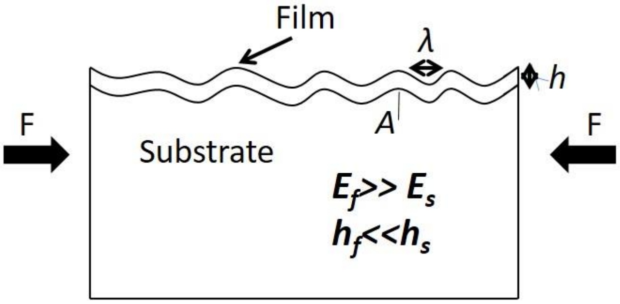

Figure 4. A Schematic presenting stiff film/compliant substrate at a wrinkled state induced by compressive strain. (λ: wavelength, *A*: amplitude, *h*: the thickness of the film, *F*: compressive force)

Wrinkles as micro or nano patterns on the surface can be obtained in three different categories: layered structure, homogenous film (polymer gels) and gradient system[50], where Figure 4 depicts the simple layered structure, where a rigid film is supported by a soft elastic substrate. Wrinkling on such a layered system is formed by thermal expansion mismatch (thermally induced wrinkles), externally applied compressive force (mechanically induced wrinkles) and differential swelling (swelling induced wrinkles).[52] The thin layer film in the bilayer structure can be created either by physical treatment such as oxygen plasma exposure and ultraviolet/ozone treatment[53] on the top of the substrate (mostly used PDMS) or by deposition of a thin layer of metal such as gold, silver or aluminum on elastomeric or shape-memory polymer (SMP) substrates.[54] Different topographies can be generated ranging from homogenous one-dimension wrinkling patterns induced by uniaxial strain to complex wrinkling patterns such as square checkerboard, hexagonal, triangular, and herringbone modes, which are the results of biaxial compressive strains. [55-56]

Wrinkles are characterized by wavelength (λ) and amplitude (A). Equation 2 states the correlation between the λ and the properties of the film (f) and substrate (s) (their Poisson ratio and Young's modulus), and the thickness of the film (h). In addition, the A is dependent (Equation 3) on the h_f and the critical strain (ε_c), which is the minimum strain required for the formation of wrinkles. It is reported that the strain as low as 2.6% induced by SME on the substrate is sufficient to generate wrinkles.[57]

Equation 2
$$\lambda = 2\pi h \left[\frac{E_s}{3E_f}\right]^{1/3}$$

Equation 3
$$A = h\left[\frac{\varepsilon}{\varepsilon_c} - 1\right]^{1/2}$$

Equation 4
$$\varepsilon_c = \frac{1}{4}\left[\frac{3E_f}{E_s}\right]^{2/3}$$

Referring to aforestated equations, topographies are dependent on the thickness (h) and Young's modulus (E_f) of the film. Having a gradient thickness and a gradient modulus of a film provided by gradient crosslinks leads to the formation of hierarchical wrinkles on the surface.[47] However, the uniform thickness and elasticity of the film display parallel stripes of homogenous patterns on the surface. Moreover, topography of substrates triggers more diverse hierarchical wrinkling than flat substrates.[58] In 2017, hierarchical wrinkles were obtained on a nearly hemispherical bilayer structure fabricated under hydraulic loading.[59] On bilayer structures having gradient properties of the film, the direction of the compressive strain (perpendicular or parallel) to the gradient direction resulted in different sorts of hierarchical wrinkles.[47]

Dynamic (active) micro or nano wrinkles were reported in bilayer structures with different stimuli such as moisture[46], heat, near infrared light[60], visible light[61], reductant[62], voltage[63] or solvent responsive[44], where the film was modified by interpenetrating polymer network (IPN)[62]or crosslinked polymers[46]. Such a self-assembly pattern was not reported on a bilayer structure, where film consisted of metal. Such reversible patterns on a surface of metal can be practical in applications, where conductivity of surface is also demanded in some electrical applications or a metal surface is required in a specific structure.

Shape-memory polymers (SMP) are utilized in wrinkling studies, either as substrate[56], film[64] or even nanoparticles covered by Au film[65]. Employing reversible and ability to recover to permanent shape of SMP resulted in the achievement of repeatable and reversible wrinkles, however, in one cycle, which means one-way effect was utilized.[66-67]

Self-assembly reversible wrinkles using SMP was reported in 2019, where non-uniform symmetric localized wrinkles were observed in a bilayer structure having a recovered programmed SMP substrate covered with a 150 nm Al film. Joule heating via a wire embedded in the substrate was utilized as a stimulus to create localized wrinkles and applied as a micromirror.[68] Studying on recovery time and recovery temperature of SMP as a substrate in a bilayer structure also resulted in the microscale hierarchical wrinkles, wherein a specific recovery temperature and recovery time, wrinkles were transformed from nanoscale to microscale.[69]

The presence of wrinkles influences all surface properties such as bonding, wetting, friction, surface roughness, reflection, drag, and adhesion.

Shape-Memory Effects (SME)

SME in polymers is considered as the ability to recover from a deformed "programmed" shape (called encoding or programming) to its permanent shape. This unique function offers significant capabilities in different fields ranging from surgical stents to aerospace industries.[70] Generally, an SME is encoded in polymer networks consisting of netpoints connecting switching domains. Netpoints maintain the permanent shape and are classified into chemical (covalent bonds) or physical (intermolecular interaction) netpoints. From a thermodynamic point of view, controlled storage of entropy elastic energy via crystallization or vitrification of switching domains and subsequent release of energy exhibit shape changes.[71] The SME is considered as a function of material coming from polymer morphology, molecular architecture and specific processing triggered by various stimuli such as heat, moisture, light, IR, electric field and alternating magnetic field. Defining temperatures for encoding shapes via thermal stimulus is determined based on the second curve of DSC (Differential Scanning Calorimetry), in which a mechanical deformation (temporary shape) called programming strain ($\varepsilon_{\mathrm{prog}}$) is applied at an elevated temperature of T_{prog} (temperature of programming) above a switching transition temperature ($T_{\mathrm{prog}} > T_{\mathrm{trans}}$) and the deformation is fixed at a temperature below the switching transition temperature ($T_{\mathrm{fix}} < T_{\mathrm{trans}}$) (Figure 5A). Furthermore, for polymer networks having more than one thermal transition temperature (Figure 5B), T_{prog} can be attributed to the highest thermal transition temperature, assigned to the T_{m} of the netpoints and the second highest transition temperature, which could be T_{g} or T_{m} is correlated to the switching domains.

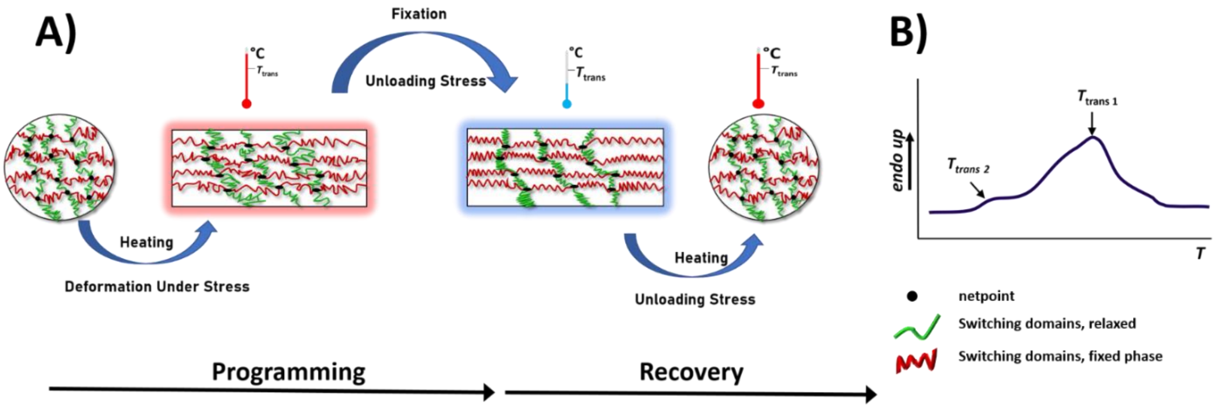

Figure 5. A) A scheme depicting a molecular mechanism for the classic SME for the copolymer network having netpoints and switching domains. B) The second curve of DSC (Differential Scanning Calorimetry) of networks having two different transition temperatures. The DSC curve works like a temperature map pointing out assigned temperatures for programming (T_{prog}), fixing (T_{fix}) and switching (T_{sw}) temperatures based on the thermal transition temperatures of the studied material.

A conventional triple shape-memory effect (TSME) can be realized by encoding in two different steps at two different temperatures assigned to the switching domains and the subsequent two recovery phases (Figure 6). To obtain a TSME, a copolymer network having multiple well-separated thermal transition temperatures or a broad ΔT_{m} is required.[72] The conventional SME is a one-way effect in a free-standing state or displayed the reversibility in cycles under external stress position.[73]

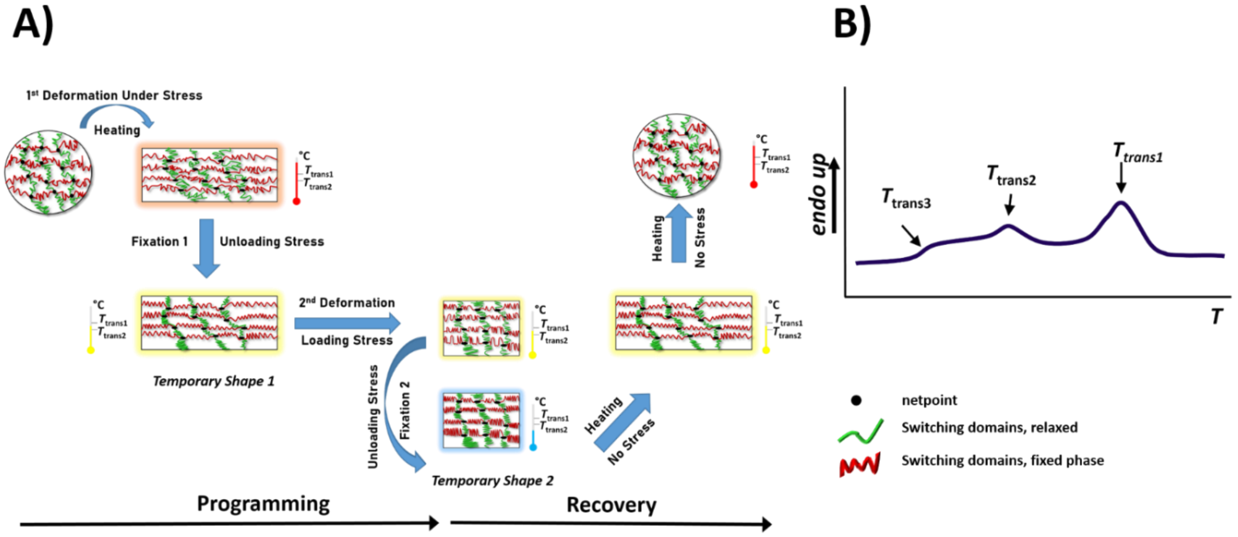

Figure 6. An illustration of the TSME of a copolymer network. TSME can be implemented in networks having either multiple well-separated thermal transition temperatures or within a broad ΔT_{m} obtained on the second heating run of the DSC curve.

Furthermore, the reversible bidirectional shape-memory effect (rbSME)[74] is demonstrated in semi-crystalline copolymer networks having a broad ΔT_{m}. An area under the curve of a broad ΔT_{m} indicates a degree of crystalline having a distribution of different sizes of crystalline domains. Defined T_{sep} within ΔT_{m} (Figure 7) separates the crystalline domains into large and small crystallite sizes, in which large crystalline domains serve as a skeleton and fix a first temporary shape calling shifting-geometry determining domains (SGDs) and small crystallite sizes act as actuator domains (ADs). Cooling networks from T_{sep} to T_{low} causes the exothermic crystallization process and amorphous ADs become oriented along the large crystalline domains stabilizing the second temporary shape[75]. On the other hand, heating from T_{low} to T_{sep} yields to gain elastic entropy and results in the recoiling of ADs causing shrinkage. This mechanism is called crystallization-induced elongation (CIE) and melting-induced contraction (MIC).

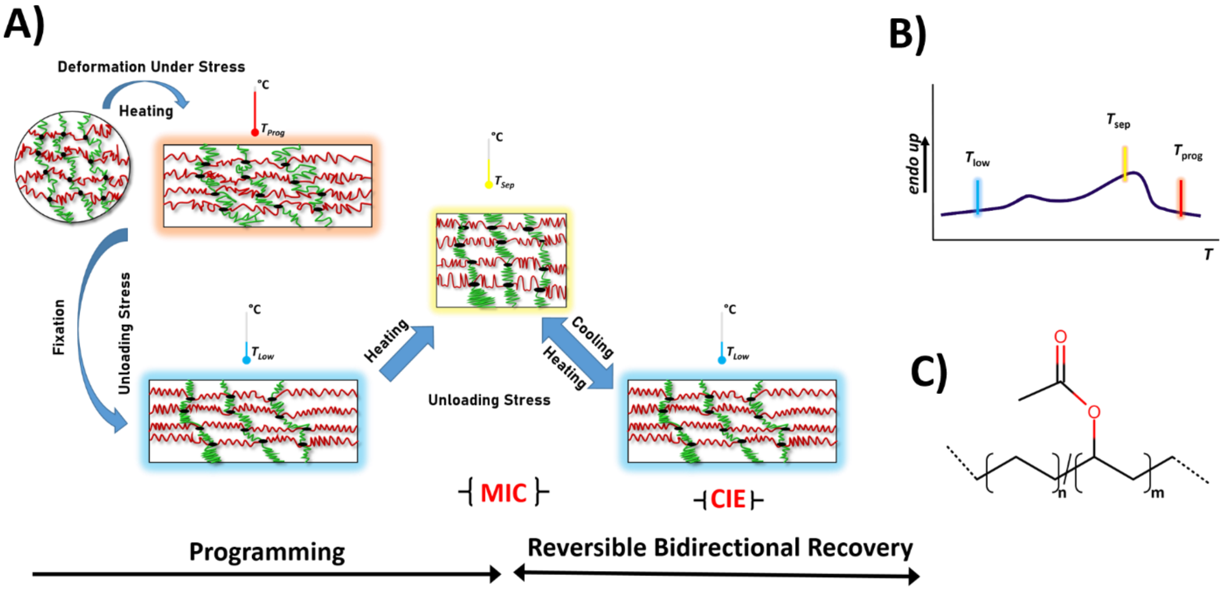

Figure 7. A schematic showing the rbSME of copolymer networks having a broad ΔT_m indicates a distribution of small and large crystalline sizes. The imposed melting-induced contraction (MIC) upon heating and crystallization-induced elongation (CIE) upon cooling of the ADs are presented.[76] C) rbSME was exhibited firstly on cPEVA.

Besides, for gaining bidirectional actuators, in addition to crystalline domains (the broad ΔT_m), a certain weight content of amorphous domains is also needed.[72] rbSME was reported in 2013 for the first time and was shown on covalently cross-linked poly [ethylene-*co*-(vinyl acetate)] called cPEVA (Figure 7C) under stress-free conditions in multicycles (120 thermal cycles) between 25 °C and 75 °C).[72] Because of the repetition of the rbSME, such a smart behavior could be promising for applications such as artificial muscles in different fields, where a muscle-wise response is demanded.[77]

Nevertheless, this effect is reported at temperatures, which are not relevant to physiological one as T_{sep} is normally higher than body temperature. Employing rbSME for health technology requires designing the triggering temperature around 37 °C. A body temperature activating rbSME has been realized in a few semi-crystalline polymer networks such as Poly(ethylene glycol) (PEG) and *n*-butyl acrylate networks reported in 2017[78] and polytetrahydrofuran (PTHF) and PEG studied in 2021[79]. To my knowledge, there is no study reported networks, in which triggering temperatures for rbSME were designed between room temperature and body temperature, which these temperatures are beneficial for health technology.

Chapter 2. Aim and Strategy

The aim of this thesis was to generate new functions in bilayer systems through combining layers of different moduli and/or porosity and to develop suitable processing techniques to access these structures.

In particular, the following structures and effects were targeted (Figure 8):

i. A bilayer structure, where each layer with a different Young's modulus has pores. ($E_1/E_2 < 10$), utilizing a solvent-free process as a sustainable and a melt-phase process in order to apply the suggested process on a complex geometry with porous layered structure.
ii. A bilayer structure, where one layer is porous and one layer is compact acting as a reinforcement agent increasing the mechanical strength in bending deformations ($10 < \mathrm{E}_1/E_2 < 10^4$), utilizing a solvent-free and a melt-phase process in order to apply the suggested process on a complex geometry layered structure with a selective porous layer.
iii. A bilayer structure, having a thick compliant substrate and a thin metal film ($10^4 < E_1/E_2$), in which employing rbSME on the substrate would lead to the formation of reversible topographies in nanoscale on the metal surface.

In addition, materials for each layer were chosen based on their repeatedly utilizations in medical technology and were reported as non-toxic in biological systems. In addition, manufacturing processes such as injection molding and extrusion (melt-phase process) require materials having high M_w to bear high shear stresses.

In the first part of the thesis, manufacturing and characterization of bilayer structures are conducted in a way that one or two layers are porous and both layers consisted of the polymeric material. System 1 and system 2 are fabricated by sequential injection molding. Here, the sequential injection molding of two different materials and introduction of the pores through different methods are opted as the scale-up fabrication methods, in which the studied method can be adjusted to produce bilayer structures in small and large complex geometries for different applications.

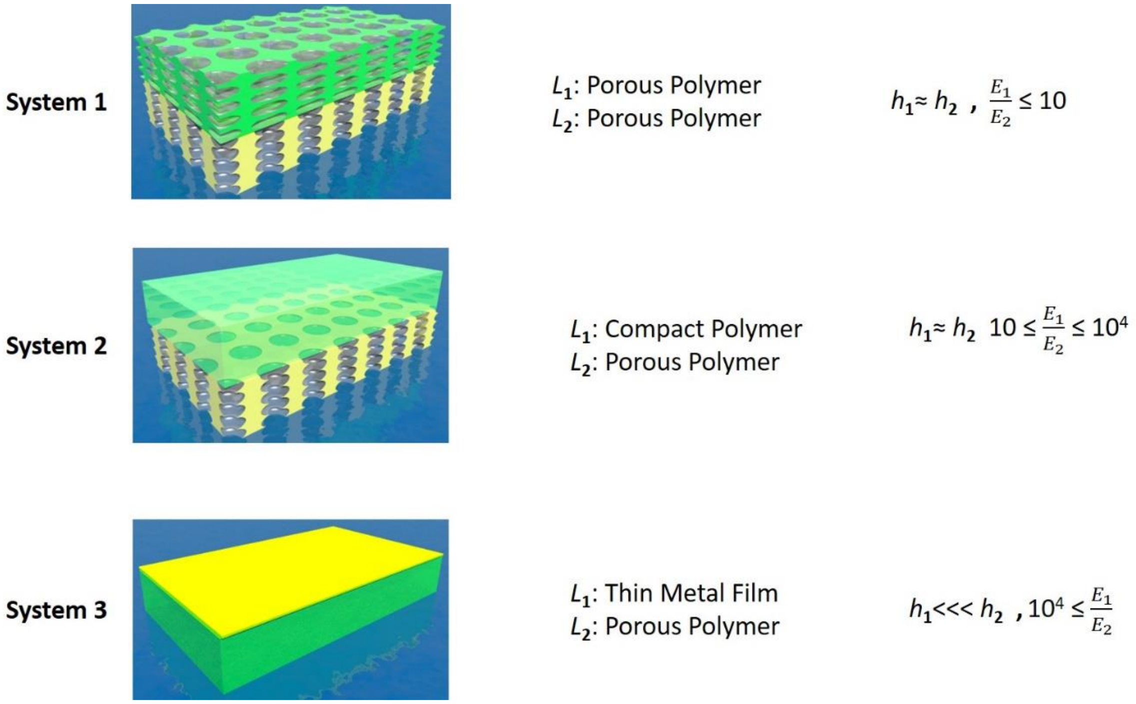

Figure 8. An illustration of three bilayer systems explored in this dissertation. *L* stands for layers. *h* is the thickness of each layer and *E* is Young's modulus.

System 1

Polymer Porous Layer - Polymer Porous Layer $E_1/E_2 < 10$

To produce the matrix of system 1, two commercial aliphatic polyether-based thermoplastic polyurethanes (Tecoflex® EG-100A and Tecoflex® EG-72D) composed of methylene isocyanate, poly (oxytetramethylene) glycol, and 1, 4-butanediol called Tecoflex® were selected for each layer (Figure 9). The letter A and D refer to the shore hardness scale tests, where A is specified for the flexible and rubbery type of material and D indicates the harder type. Since Tecoflex® consists of hard domains, soft domains, and a mixed-phase with suitable thermal transition, it can be programmed to show a shape-memory effect (SME). This was investigated for the layered structures.[80] Thermal and mechanical properties such as E and T_g of copolymers are governed by the mixed phase varied by changing the hard to soft segment ratio, in which Tecoflex® EG-100A and Tecoflex®-EG-72D are composed of 41% and 58% hard domains, respectively. Both grades of Tecoflex® are suitable for melt manufacturing processes such as injection molding and extrusion, where high shear stress is applied. Moreover, the aforementioned grades are also highly recommended by suppliers for manufacturing medical and healthcare devices. It was hypothesized that by dissolving one phase of co-continuous melt blend in water after the manufacturing process, the bilayer porous structure with different elasticity in each layer would be obtained in a solvent-free process.

To introduce pores via the creation of a co-continuous blend, polyvinyl alcohol (PVA) was opted for the selective polymer extraction, as it is water soluble. Due to its water solubility, PVA is considered a green-leaching material not requiring potentially toxic organic solvents for dissolving this phase. Besides, in the case of using the obtained porous material in healthcare applications, any residual PVA after the leaching stage is not considered harmful, as PVA is often employed in intrinsically biocompatible systems.[21]

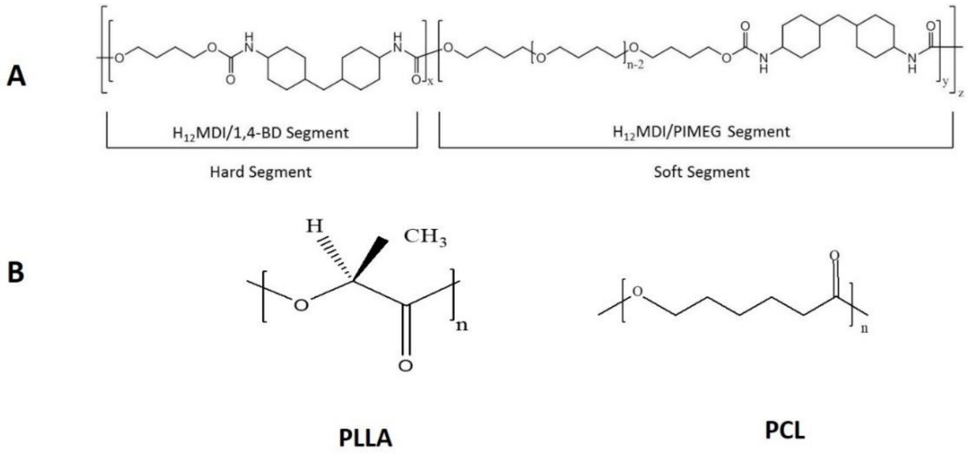

Figure 9. A) Chemical structure of Tecoflex® employed in the bilayer system 1, in which Tecoflex®-100A and Tecoflex®-72D are composed of 41% and 58% of the hard segment, respectively. B) Chemical structure of poly (*L*-lactic acid) and poly (*ε*-caprolactone) employed in the bilayer system 2.

System 2

Polymer Porous Layer – Polymer Compact Layer $10 < E_1/E_2 < 10^4$

To fabricate system 2, in which one layer is compact and the other one is porous, considering the assigned ratio of *E*, Poly-*L*-lactic acid (PLLA) and Poly (*ε*-caprolactone) (PCL) (Figure 9), based on their difference in mechanical and thermal behavior were selected for compact and porous layer, respectively. Both PLLA and PCL are biodegradable and are often utilized in medical technology due to their biological safety.[81] Both materials are commercially available and were purchased from suppliers. The T_m of PCL is ≈ 58 °C overlapping with the T_g of PLLA (≈ 58 °C). At room temperature, PLLA is in the glassy state having a Young's modulus (*E*) of 1700 MPa while PCL is in the rubbery state having a *E* of 300 MPa. The introduction of pores into the PCL layer was yielded by exposure of the PCL-PLLA bilayer structure to $scCO_2$ in an autoclave at defined temperature and pressure. It was hypothesized that the solubility of $scCO_2$ would be different in the two different polymers, which under optimized conditions should allow to selectively foam one of the two layers.

Pores and porosity are characterized for system 1 by applying ImageJ software on obtained images from scanning electron microscopy (SEM) and calculation of density, respectively. For system 2, the shape of pores and porosity are estimated by SEM and X-ray computed microtomography (µCT), respectively. Mechanical tests would give information about the effect of pores and the influence of $scCO_2$ autoclave on the mechanical behavior of the layers and the bonding strength between layers. For this purpose, tensile test, compression test and T-peel test are performed for individual layers and bilayer constructs, respectively. Wide angle X-ray scattering (WAXS) provides information about the effect of the $scCO_2$ autoclave process on the growth of crystalline in the compact layers.

System3

Polymer Porous Layer – Polymer Compact Layer $10 < E_1/E_2 < 10^4$

The third part of this thesis is focused on generating reversible wrinkles (switch on/off) on a surface of a bilayer structure of a 10 nm gold film and a 1 mm substrate of cPEVA. It was hypothesized that by empowering rbSME on the substrate at defined temperatures, the reversible compression strain would apply to a bilayer structure, which would yield the formation of reversible wrinkles in the nano scale on the gold surface. Moreover, it was hypothesized that employing on/off wrinkles on a pre-patterned surface would lead to the formation of reversible multi patterns. To harvest this function on the surface, the substrates of cPEVA are programmed in uniaxial, sequential and simultaneous bi-directions by a thermomechanical tensile machine prior to the sputtering of the 10 nm gold film. T_{high}, T_{sep}, T_{low} and T_{mid} within a broad ΔT_{m} are defined by differential scanning calorimetry (DSC). The dimensions of formed wrinkles (wavelength (λ) and amplitude (A)) on the surface of the gold film are quantified by applying 2D-fast Fourier transformation (2DFFT) on SEM images and atomic force microscopy (AFM) at defined temperatures. To fathom the mechanism of oriented crystalline domains in the substrates on the imposed strains on the gold film, WAXS is utilized to study the formation of the orientation of crystalline domains at the defined temperatures. In addition, understanding the relationship between imposed compressive strain and temperature on the programmed substrates requires studies in a cyclic temperature stress-free condition. Finally, exploiting this *in-situ* on/off wrinkles and multi-pattern wrinkles in medical technology compels adjusting rbSME and switching temperature around physiological temperature (≈ 37 °C). To answer this question, the last part of this thesis focused on the synthesis of semi-crystalline co-polymer networks having a broad ΔT_{m} around body temperature. The melting transition temperature of oligo(ε-caprolactone) (OCL) is shifted to the lower temperature range by combining different molecular weights of OCL in a network of OCL and *n*-butyl acrylate (BA). The actuation performance of OCL segments are conducted in cyclic thermomechanical experiments. To define T_{prog}, T_{low} and T_{sep} and $\varepsilon_{\mathrm{prog}}$, DSC and tensile tests are performed on the synthesized networks. Finally, rbSME are quantified ($\varepsilon_{\mathrm{rev}}$) by cyclic thermomechanical test. To fathom the contribution of the degree of crystallinity and average lateral crystal size of OCL actuation domains to exhibit rbSME at specified temperatures, WAXS experiments are performed at specified temperatures.

Chapter 3. Organization of the thesis

This cumulative thesis is divided into 10 chapters and 1 appendix explaining the results of studies performed for fabrication of three distinct bilayer systems.

The subject of each chapter is briefly described here for better clarity of the scientific work. In addition, short summary of the manuscripts and the author's contribution is provided for chapter 4-7.

Chapters

Chapter 1	contains the introduction and the research back ground of this thesis.
Chapter 2	provides motivation and aims and describes strategies of the research.
Chapter 3	explains the organization of the thesis having brief summaries of the publications with the list of attributed 3 publications and one unpublished manuscript.
Chapter 4	describes an organic solvent free method for preparation of bilayer porous structure having different PUs in each layer via extrusion, sequential injection molding, and leaching processes. In addition, applying annealing process at two different temperatures prior to the leaching process inducing coarsening effect on the binary blend, which led to the variation of pores size, while the porosity was kept constant.
Chapter 5	presents an organic solvent free method for manufacturing the bilayer structure of PLLA and PCL layer via sequential injection molding. The selectively foaming process was applied on PCL layer upon exposure to the $scCO_2$ foaming process. In addition, the influence of variation of foaming process interval time on the porous structure as well as compressive mechanical properties of PCL layer, and tensile properties of PLLA layer were explored.
Chapter 6	described a general approach to have reversible wrinkles on a bilayer structure having a substrate with rbSME and a thin gold layer. Furthermore, reversible multi-pattern was obtained by exploiting a programming of sequential biaxial stretching on the mentioned substrate.

Chapter 7	exhibits two polymer networks exhibiting the rbSME around human body temperature for the first time. Moreover, it was proven that the skeleton domains could be even provided by orientational memory of the oriented domains.
Chapter 8	covers a comprehensive discussion of the scientific achievement.
Chapter 9	concludes the result and outlook of the work as well as indicating limitation and suggestion for further investigation.
Chapter 10	covers all references cited in this work.
Appendix	shows published version of all manuscripts as well as an unpublished manuscript.

Publication

1) **Saatchi, M.**, Behl, M. and Lendlein, A. (2013), Manufacturing and Characterization of Controlled Foaming of Single Layers in Bilayer Constructs Differing in Pore *Morphology*. *Macromol. Symp*., 334: 33–39.

2) **Saatchi, M**., Behl, M. and Lendlein, A. (2014), Double Layer Porous Structures by an Injection Molding/Particulate Leaching Approach. *Macromol. Symp.*, 346: 100–107.

3) **Saatchi, M.,** Behl, M., Nöchel, U. and Lendlein, A. (2015), Copolymer Networks From Oligo(ε-caprolactone) and *n*-Butyl Acrylate Enable a Reversible Bidirectional Shape-Memory Effect at Human Body Temperature. *Macromol. Rapid Commun.*, 36:880-884.

Unpublished material

Saatchi, M., Nöchel, U., Behl, M., and Lendlein, A. A General Approach Toward Multi-Pattern Memory Effect via Reversible Bidirectional Shape-Memory Substrates.

Chapter 4. Double Layer Porous Structures by an Injection Molding/Particulate Leaching Approach

Mersa Saatchi[1, 2, 3], Marc Behl[1, 3], and Andreas Lendlein[1, 2, 3]

1. Institute of Biomaterial Science and Berlin-Brandenburg Center for Regenerative Therapies, Helmholtz-Zentrum Geesthacht, Kantstraße 55, 14513 Teltow, Germany

2. Institute of Chemistry, University of Potsdam, 14469 Potsdam, Germany

3. Tianjin University–Helmholtz-Zentrum Geesthacht, Joint Laboratory for Biomaterials and Regenerative Medicine

This work is published in:

Macromolecular Symposia, 2014, 346(1): 100-107.

DOI: 10.1002/masy.201400158

PUBLICATION (Appendix)

Contribution to the publication

My contribution to this work are

- Literature research:
    - Study of demands of multilayer scaffolds utilized in regenerative medicine
    - Study of requirements of scaffolds
    - Study of various preparation methods of scaffolds
    - Study of particulate leaching method for introduction of pores
    - Study of the annealing effect on the coarsening phenomena in polymer blends
- Study design:
    - Selection of non-toxic polyether urethanes (PU) and polyvinyl alcohol (PVA) as candidate materials for fabrication of bilayer scaffolds
    - Comparison of the experimental results of bilayer structure with theoretical result of elastic modulus of composite materials
    - Investigation of the annealing process on PU/PVA polymer blends for study the effect of coarsening phenomena and pores morphology
- Experimental work:
    - Fabrication of bilayer scaffolds via extrusion, sequential injection moulding, and leaching process under different thermal conditions
    - Characterization of material properties: determination of hard segment ratio of two different PUs by means of ^{1}H-NMR; determination of mechanical properties of each layer as well bilayer structure by means of tensile tests at 37 °C; characterization of pores morphology by scanning electron microscopy and analysis the pores images by ImageJ software, estimation of porosity by determination of density
- Analysis and interpretation of experimental data in text paragraph, tables, and figures
- Writing the first version of manuscript, revised and finalized in cooperation with co-authors

Short summary of the publication

Scaffolds as a temporary substitute for the extracellular matrix should provide interconnected pores and often require a multilayer design to mimic the geometry and biomechanics of the target tissue. Here, it was explored whether bilayer porous structures can be obtained by a process free of organic solvents and how the individual layers contribute to the overall elastic properties. Porous layers were obtained from polyurethane (PU) blends with polyvinyl alcohol (PVA), which were immersed in water after sequential injection molding. Pore sizes in both layers ranged from 1 µm to 100 µm with an average of 22 ± 1 µm at a porosity of 50 ± 5% in combination with a high interconnectivity. The pore sizes were tailored by applying an annealing treatment, while the porosity was kept constant. Mechanical properties of the individual layers and the double layer constructs as determined by tensile tests suggested that the overall elasticity of the compact bilayer construct and porous bilayer construct was in agreement with the predicted overall elasticity according to the rule of mixtures. The porous bilayer model system will serve as a basis for determining structure-property relationships with respect to pore size, porosity as well as mechanical properties of individual layers and in this way enable a knowledge-based design of layered scaffolds. At the end, this bilayer system is a small example of multifunctional multilayer system having structural function in a layered structure.

Chapter 5. Manufacturing and Characterization of Controlled Foaming of Single Layers in Bilayer Constructs Differing in Pore Morphology

Mersa Saatchi[1, 2, 3], Marc Behl[1, 3], and Andreas Lendlein[1, 2, 3]

1. Institute of Biomaterial Science and Berlin-Brandenburg Center for Regenerative Therapies, Helmholtz-Zentrum Geesthacht, Kantstraße 55, 14513 Teltow, Germany

2. Institute of Chemistry, University of Potsdam, 14469 Potsdam, Germany

3. Tianjin University–Helmholtz-Zentrum Geesthacht, Joint Laboratory for Biomaterials and Regenerative Medicine

This work is published in:

Macromolecular Symposia, 2013, 334(1): 33-39.

DOI: 10.1002/masy.201300151

PUBLICATION (Appendix)

Contribution to the publication

My contribution to this work are

- Literature research:
  - Study of various methods of preparation scaffolds used in regenerative medicine
  - Study of different methods for reinforcement of scaffolds
  - Study of new methods for preparation bilayer structures and selectivity foaming of one layer within bilayer structure in an organic solvent-free process
  - Study of the supercritical carbon dioxide ($scCO_2$) foaming process and influence of the different process parameters on the pores morphology
- Study design:
  - Selection of poly(*L*-lactide) (PLLA) and poly(ε-caprolactone) (PCL) as two different biocompatible materials used in preparation of bilayer constructs
  - Selection of sequential injection molding and $scCO_2$ foaming process as fabrication processes employed for this system
  - Investigation of variation of time interval foaming process on the pores morphology
- Experimental work:
  - Preparation of bilayer scaffolds via sequential injection molding
  - Preparation of selective foamed layer via $scCO_2$ foaming process
  - Characterization of the individual layers: determination of molecular weight of PCL and PLLA after each process, characterization of thermal properties by DSC after each process, investigations of mechanical properties using tensile tests for PLLA layers and compression tests for PCL layers, characterization of morphology by scanning electron microscopy; performance of T-peel test for bilayer structures
- Analysis and interpretation of experimental data in text paragraph, tables, and figures
- Writing the first version of manuscript, revised and finalized in cooperation with co-authors

Short summary of the publication

Bilayer porous constructs from degradable polymers are considered as scaffold materials with beneficial elastic properties for cell culture application in tissue engineering. Layered scaffolds from biodegradable materials can be classified as multifunctional multilayer systems having combination of structural, stimuli-sensitivity as well as degradability function in one system. Here, it was explored whether such bilayer constructs, in which only one layer was porous while the other layer enhanced the compressive mechanical properties could be created by specific foaming of one layer with supercritical carbon dioxide ($scCO_2$). The bilayer constructs of a poly(*L*-lactide) (PLLA) and a poly(ε-caprolactone) (PCL) layer were prepared by sequential injection molding and subsequent specific foaming with $scCO_2$. Foaming conditions of T = 45 °C and P = 100 bar resulted in the formation of a porous PCL layer and a non-porous PLLA layer. When the time intervals of the foaming process were increased the pore size was increased and the shape of the pores was changed from a circular to an unidirectional lamellar shape, which reduced the compressive elastic modulus of the porous PCL layer. Furthermore, the foaming process increased the adhesion force between the PLLA and PCL layers, which was attributed to a higher degree of diffusion of molten PCL into the PLLA layer. In summary, it was demonstrated that $scCO_2$ foaming process is a suitable method for the creation of layered scaffolds with only one foamed layer, in which the compressive elastic modulus and pores morphology of single porous layers can be controlled by the time interval of $scCO_2$ process.

Chapter 6. A General Approach Toward Multi-Pattern Memory Effect via Reversible Bidirectional Shape-Memory Substrates

Mersa Saatchi, Ulrich Nöchel, Marc Behl, and Andreas Lendlein

Institute of Active Polymers and Berlin-Brandenburg Center for Regenerative Therapies, Helmholtz-Zentrum Hereon GmbH, Kantstraße 55, 14513 Teltow, Germany

This work has not been published yet.

Manuscript (Appendix)

Contribution to the manuscript

My contribution to this work are

- Literature research:
  - Study of different structures on the surfaces such as wrinkles and patterns.
  - Study of different approaches and parameters affecting the wrinkles formation
  - Study of mechanical behaviour of gold films
  - Study of characterization methods for quantifying wrinkles
  - Study on reversible patterns in nature
  - Study of wrinkles fabricated by substrates having SME
- Study design:
  - Selecting a substrate showing rbSME and characterization of the substrate
  - Investigation of different programming strain modes on formation of patterns in a bilayer system
- Experimental work:
  - Compounding, substrate formation, programming in different strain modes, sputtering gold film on the programmed substrate
  - Characterization of substrate: determination of gel content and swelling behaviour; characterization of thermal and mechanical properties by DSC and tensile tests; estimation of cross-link density based on Mooney-Rivlin equations; characterization of rbSME by means of thermo-mechanical cycles and determination of attributed parameters
  - Characterization of wrinkles in bilayer structure by means of SEM and 2DFFT method
  - Preparation samples for WAXS, contact angle measurements and AFM
- Analysis and interpretation of experimental data in text paragraph, tables and figures
- Writing the draft version of manuscript

Short summary of the publication

A simple approach to achieve reversible uniaxial wrinkles in a bilayer structure utilizing a substrate showing a reversible bidirectional shape-memory effect (rbSME), in which the formed wrinkles can be tuned by variation of separation temperature (T_{sep}) was demonstrated. Furthermore, reversible multi-patterns (RMP) (i.e. complex and parallel wrinkles) can be formed by applying the concept of reversible uniaxial wrinkles on a pre-patterned surface. This was achieved by conducting sequential biaxial (SEQB) stretching (programming) on a substrate having a broad melting temperature transition, which led to the formation of permanent wrinkles obtained by the first recovery of a triple shape-memory effect and temporary wrinkles caused by the rbSME. In this way, the application spectrum of rbSME can be extended to tunable material surfaces that are relevant in applications such as photonics, electronics, and aerodynamics.

Chapter 7. Copolymer Networks From Oligo(ε-caprolactone) and *n*-Butyl Acrylate Enable a Reversible Bidirectional Shape-Memory Effect at Human Body Temperature

Mersa Saatchi[1, 2, 3], Marc Behl[1, 3], Ulrich Nöchel[1], and Andreas Lendlein[1, 2, 3]

1. Institute of Biomaterial Science and Berlin-Brandenburg Center for Regenerative Therapies, Helmholtz-Zentrum Geesthacht, Kantstraße 55, 14513 Teltow, Germany

2. Institute of Chemistry, University of Potsdam, 14469 Potsdam, Germany

3. Tianjin University–Helmholtz-Zentrum Geesthacht, Joint Laboratory for Biomaterials and Regenerative Medicine

This work is published in:

Macromolecular Rapid Communications, 2015, 36 (10):880-884.

DOI:10.1002/marc.201400729

PUBLICATION (Appendix)

Contribution to the publication

My contribution to this work are

- Literature research:
    - Study of the rbSME and the principle of working
    - Study of the influence of the different molecular weight chain in thermal properties and shape-memory properties of networks
- Study design:
    - Selection of the mixture of OCLs with various chain lengths and different ratio of BA.
    - Investigation of the upper limit of $\triangle T_m$ as actuator domain for rbSME
    - Confirmation of exploiting the networks at relevant physiological temperature
- Experimental work:
    - Synthesis and purification of networks OCL-BA with varied chemical composition of OCLs and BA in the starting material mixture
    - Characterization of material properties: determination of gel content and swelling behaviour; characterization of thermal and mechanical properties by DSC and tensile tests; estimation of crosslink density based on Mooney-Rivlin equations; characterization of rbSME by means of thermo-mechanical cycles and determination of attributed parameters; performance of demonstration; preparation of networks for WAXS investigations.
    - Analysis and interpretation of experimental data in text paragraph, tables and figures
    - Writing the first version of manuscript, revised and finalized in cooperation with co-authors

Short summary of the publication

In this study, a new discovered bidirectional shape-memory effect (rbSME), which is classified as a stimuli-sensitivity function was adjusted to the human body temperature in order to exploit this fabulous effect in tremendous biomedical applications. The strategy was based on the reduction of the melting temperature range (ΔT_m) of the actuating oligo(ε-caprolactone) (OCL) domains in copolymer networks from OCL and *n*-butyl acrylate (BA), where the reversible effect can be adjusted to the human body temperature. In addition, it was investigated whether a rbSME in the temperature range close or even above $T_{m,offset}$ could be obtained.

Two series of networks having mixtures of OCLs revealed broad melting temperature ranges (ΔT_m) from 2 °C to 50 °C and from -10 °C to 37 °C, respectively. In cyclic, thermomechanical experiments the rbSME could be tailored to display pronounced actuation in a temperature interval between 20 °C and 37 °C. This adjusted function can be used in a multilayer structure, which induces one function needed for biomedical applications.

Chapter 9. Discussion

In this chapter, the findings obtained from the work presented in chapters 4 to 7 are discussed and compared with the current state-of-the-art. Exploring the fabrication methods for double layer structures having hybrid materials with different properties and functions is the dominant aim of this thesis.

Generally, reproducibility of fabrication methods is a key factor for nominating an approach in a large scale and mass production. Here, conventional melt-based formation processes such as extrusion and mini-injection molding were employed in the creation of the bilayer systems 1 and 2. In this study, a conventional lab-scale mini injection molding was used in a sequential manner to create the double layer structure as it is described in our works.[82,83]

System 1

Firstly, the focus on bilayer structures was fabricating a system to be employed in a health-oriented technology. Utilizing PLLA and PCL as biodegradable and non-toxic polymers was estimated costly for the first bilayer system. Hence, to avoid wasting material, an economical commercial medical grade polyether urethane (Tecoflex® EG72D and Tecoflex® 100A) was chosen for the creation of the bilayer system 1.

The melt-based process has the advantage of avoiding solvents in the formation process. To introduce pores into the bilayer system 1, PVA as water solvable leaching material was blended in a co-continuous phase into two polyurethanes separately, and after sequential injection molding, the PVA was washed out by immersion in water. 50% porosity was expected from the system as the contribution of PVA in the blend of PVA and PU of each layer was 50%. As the image of SEM (scanning electron microscope) exhibited, the obtained pores from the co-continuous blend were open and interconnected. Measurement of porosity proved that porosity was 50%. However, complete removal of PVA cannot be guaranteed. In the case of applying such a system in health technology, having traces of PVA in the system is harmless because of the non-toxicity of PVA. The morphology of obtained pores was tailored by applying an annealing process as a post-treatment before the leaching step, which had no effect on porosity but led to the decrease of the average pores diameter from 23 ± 10 µm with no annealing time to 20 ± 9 µm by 1 hour annealing time at 110 °C and 15 ± 8 µm for 1 hour annealing time at 130 °C for a layer having Tecoflex®-

EG72D as the matrix. In the softer layer having Tecoflex®-100A as the matrix, the average pore diameter reduced via the annealing process from 22 ± 12 µm with no annealing time to 20 ± 10 µm annealed at 110 °C for 1 hour and 17 ± 9 µm annealed at 130 °C for 1 hour. The obtained pore shape from this method can be varied to gradient and oriented structure by applying gradient shear stress and gradient shear temperature in the process of injection molding, which was studied in the morphology of co-continues blend of PBAT/PB reported in 2021.[23] Given such a gradient and an oriented structure to pores would affect the elongation at break as well as compression modulus of the product.

Anisotropic pores were also reported to be achieved by empowering fixed drawing ratio as a post-treatment for manipulation of the blend morphology and architectures before washing PEO phase of the co-continuous blend of PCL/PEO.[29]

Additionally, in 2006, Haugen et al.[26] took benefits from moistures in granulars in a conventional injection molding process instead of drying the granulates before feeding to the hopper. The moistures in the pellets along with 40% wt. of NaCl particles were used as a foaming agent and porogen, respectively. The obtained pores were also interconnected and open and the average diameter of the pores and the porosity were 270 ± 90 µm and 64%, respectively. Because of the thermal stability of NaCl ($T_m \approx 800$ °C) in the range of polymer process temperature (≈ 180 °C), the introduced process heat was not able to alter the particle size of salt as the leaching material. However, the high temperature of processing compelled the water to evaporate, but it was trapped in the melt due to the low diffusibility. As a result of the high pressure in the nozzle of injection molding and dissolving water in the molten polymer, water reached the supercritical state, in which both gas and liquid phases co-exist. Upon injecting into the mold having a lower temperature, a thermodynamically unstable state was reached via a rapid drop of pressure, which led to the formation of closed and well-distributed cells in the matrix. The subsequent immersion in water caused the salt particles to dissolve and led to the interconnected pores. In the study of Haugen, the effect of various parameters of injection molding on the tailoring of the mean pores diameter and porosity was also investigated. It was found that the mean pore diameter dropped from 270 µm to 10 µm, where the injection speed was increased from 3 mm/s to 5 mm/s, while the porosity remained unchanged. It was also shown that the increase of injection pressure, plasticize speed, cylinder, and mold temperature raised the mean pore diameter. On the other hand, increasing the plasticizing pressure from 5 bar to 10 bar affected the mean pore diameter grew from 25 µm to 340 µm. Although the increase of pressure did not affect the porosity, however, caused the narrower pore distribution pore size. Porosity was also kept constant by changing the H_2O concentration, nonetheless, the increase in cylinder and mold temperature showed the enhancement of the pore mean diameter and also porosity.

The injection molding employed in this study and the aforementioned investigations was conventional mini–lab injection molding. However, utilization of high pressure and temperature and high injection rate leads to the degradation of the temperature-sensitive polymers and generates low-quality products. To overcome this problem, temperature-sensitive polymers can be processed by microcellular injection molding (MIM). Adding fine fillers to the polymers melt as porogen increases the quality of the pores and acts as an efficient cell nucleation agent, enhancing the size of the pores.[84] Kramschuster et al.[85] blended PLA and PVA in a co-continuous phase and utilized salt as porogen in the MIM to obtain a highly porous structure employed as a scaffold in tissue engineering. The achieved porosity structure for this sensitive-temperature polymer from such a combination system was reported 75% with a mean pore diameter of 200 µm. In this case, the combination of PVA and salt as porogen was the way to overcome the formation of the solid-skin layer by MIM. Comparing the dimension of the obtained bilayer system 1 before and after leaching process (Figure 10A) exhibited a shrinkage of the dimension in the direction of the flowing melt, and swelling in the perpendicular direction of flow. These dimension changes should be considered for designing a mold and the exact required size of end-user products. Nevertheless, MIM compared to the sequential conventional injection molding and leaching process manufactures the increased dimension stability for the porous construction.[86]

Lastly, to the best of my knowledge, no other study in the literature investigated the formation of double layer porous structure via the co-continuous approach created by sequential injection molding similar to our investigation for the bilayer system 1.[83] Utilizing sequential injection molding in the formation of the bilayer porous structure could be conducted in an assembly section of manufacturing products, whether the first layer (or item) can be fabricated in another production line, which requires the relevant injection die with precise geometry. Moreover, removal of leaching material from the co-continuous phase from double layer structures provides interconnected pores on the skin and core of each layer. Nevertheless, the drawback of this method is that the obtained porosity is around 50% - 60% and removal of leaching materials from the core section of layers, which are located close to the weld line of bilayers cannot be guaranteed.

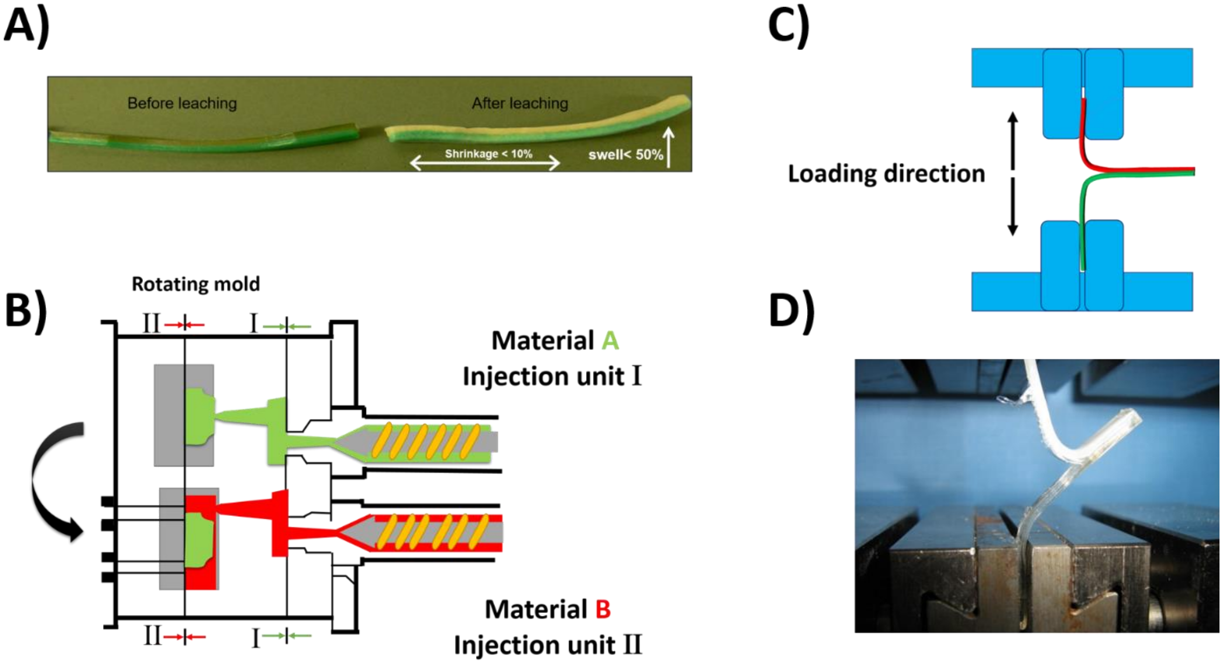

Figure 10. A) The system 1 has shrinkage in the direction of flow and swell in the perpendicular direction after injection and leaching process. B) A simple illustration presenting the over-injection molding in two steps from two different gates. C) A schematic presenting the T-peel test for measuring the bonding strength of two layers. D) The measured T-Peel test on the bilayer system 2 before foaming process using tensile machine by author, performed in 2012.

System 2

The bilayer system 2 was produced by employing a sequential injection molding of PCL and PLLA layer and consequently immersion in the autoclave of $scCO_2$ as a post-treatment of a separate batch process at T = 45 °C and P = 100 bar. A selective porous layer of the PCL layer with mean pore diameter of 190 ± 90 µm and porosity of 80 ± 5% within the bilayer structure was achieved. It is important to highlight that, while the selective foaming of one layer was exactly what was envisioned, it was still lucky that the first initial defined parameters of the autoclave worked out. It can be anticipated that, by adjusting the pressure and the temperature parameters of $scCO_2$ autoclave, both the PCL and the PLLA layer can be foamed.

More investigation showed that although PLLA was not foamed, however, the applied condition allowed growing of crystallites in PLLA, which did not occur in the short time of injection molding. The obtained structure in the foamed PCL layer was a porous core and solid skin layer. According to another report, a foam of PLLA with a high porosity up to 93% was obtained at a temperature of 100 °C - 140 °C during the foaming process, where the lower temperature generated the interconnected open cells, while the higher temperature led to the formation of closed cells.[87]

In 2020, Sanz-Horta et al.[40] explored the fabrication of a screw-like scaffold generated by 3D printers of multi-materials of PLLA in the center as an axis and PCL layers were around the PLLA axis. The obtained structure was immersed in the $scCO_2$ autoclave under T varying between 31 °C -35 °C and P of 200 bar. The PLLA axis was not altered, however, the PCL part was foamed with a skin-layer and porous core similar to my observation. To overcome this limitation on the skin layer, a post-treatment of the breath-figure was applied to the skin layer. Exploiting of the combination of $scCO_2$ and breath-figure mechanism led to the formation of the internal mean pore diameter of 2 -12 µm and external mean pore diameter of 80 - 300 µm in the PCL phase of multi-material of PCL-PLLA product.

The breath-figure technique as a self-assembly method is vastly used to induce microspores or honeycomb structure on the surface of the film either by using polymer solution or dip-coating in the appropriate solvent for a solid-polymeric product.[88]

In the aforementioned literature[40], when the temperature of the foaming process was increased from 31 °C to 35 °C, the PCL part as the control item was completely swollen and deformed from the original 3D-printed item. Nevertheless, as the temperature was increased from 31°C to 33 °C, the total shape of the PLLA internal axis and the external PCL shell was not altered indicating the presence of PLLA improved the resistance of the object during the foaming process to not lose its original form. The same approach was also taken place in our bilayer system 2, where the presence of the PLLA layer in the bilayer of PCL-PPLA hindered the deformation of the PCL layer in the swollen phase in 4 directions. As the PLLA layer was attached to the PCL layer via welding line, the swelling was restricted to the free side, where not limited by the PLLA layer.[82]

Also, in 2020, a study of the employment of the $scCO_2$ foaming process was performed (T = 50 °C, P = 200 bar) on a phase-separated immiscible melt-blend of PCL and PLGA, where the ratio of the dispersed phase of PLGA was increased up to 30%.[35] This investigation showed that the droplet phases of PLGA performed as a heterogeneous nucleating agent during the foaming process leading to the increase of pore number and shrinkage of pore size, where the foamed pure PCL showed large circular pores of 74 ±12 µm mean pore diameter. The contribution of PLGA in the melt-blend of PCL/PLGA up to 30% changed the shape of the pores from regular circles to fully polygons with a mean pore diameter of 13± 3 µm.

In addition, comparing studies revealed an influence of rheological and crystallization behavior on the interconnectivity and pore size of obtained foam, which is dependent on the M_ws. Karim et al.[89] obtained structures of foamed PCL having an M_w of 120 kDa at T = 40 °C and P = 100 bar resulting in a pore size around 260 µm. Chen et al. [33] reached pores of 60 µm and a porosity of less than 75% under the same condition, when the M_w of PCL was 80 kDa. Furthermore, Song et al.[34] compared the pores of PCL with different M_w of 27, 54, 100 and 219 kDa at T = 50 °C and P = 10 bar. The results showed that PCL with M_w = 27 kDa exhibited favorable interconnected pores with sizes of 70 – 180 µm and 90% porosity. This study highlighted the delay of crystallization and increase of the viscosity and the melt temperature by increasing the M_ws in the foaming process.

Song et al.[41] also examined the bilayer membrane of PCL/PLGA created by hot-pressure in an autoclave of $scCO_2$ at a fixed pressure of 150 bar and varying temperature of 40 °C -70 °C. Under the same conditions, PCL with low viscosity formed macrospores of 80 – 100 µm with high porosity (> 90%), while PLGA having high viscosity reached a microspores structure with a mean pore diameter of less than 10 µm and lower porosity (<80%).

The sequential injection molding in the lab was chosen as the fabrication method for this work, as it resembles over-injection molding process in mass production in different industries. Over-injection molding (Figure 10B) is a complex multi-stage operation, whereby the contact surface of a base becomes part of the mold in the formation process and operates in the following stages: preheating of mold, insertion of the base in mold, base heating, injection of new part over the inserted item, cooling of the mold, ejection of part from mold, cooling in air.[90,91] The advantage of sequential injection molding or over-injection molding is to avoid using extra adhesion between layers, which can be nominated as a green-process. Moreover, this process is able to fabricate layered structures from a wide range of materials including soft plastic such as urethanes and thermoplastics and hard plastics such as nylon and polycarbonate employed in each layer.

Whether in co-injection molding, where 2 molten phase streams are injected simultaneously into a mold from 2 distinct gates or in over-injection molding, in which one molten polymer flow is injected over the fixed piece, the formation of a weld line and its quality is inevitable. In the first process, the weld line is labeled as a flowing weld line (adjacent flow/hot weld line) and the latter type of injection molding generates the stagnating weld line (cold weld line).[24] The location of the weld line is estimated as the Achilles' heel area of the finished product and the formation of the weak interface between interfaces influences mechanical and optical properties and also the appearance of the finished injection molding products. This infirm interface can also increase the probability formation of cracks and interfacial fracture in the environmental stress-filed.

Diverse factors such as surface condition, where the weld line is located, the temperature of the cylinder (T_{cyl}), the temperature of the mold (T_{mold}), the pressure of the process, and the holding time can affect the quality of the weld line. All along the studies of the fabrication of the systems 1 and 2, the order of the sequential injection molding was performed in a way that T_{cyl} and T_{mold} would be in tune with the rang of T_{m} of the second flow and the T_{g} of the item, which was previously inserted into the mold. The intensity of bonding strength in the location of the weld line is defined by two main procedures.[92] A) Intimate contact expresses the first physical contact between 2 surfaces in over-injection molding. This mechanism occurs at a temperature close to the melting point at elevated pressure, where the second flow is injected over the item into the mold. B) Self-diffusion contact of macromolecules, which is happening just for thermoplastics and takes place in the case of having sufficient energy for motion and diffusion into another surface. This step is performed if the second flowing injected stream is in contact at T_{g} or T_{c} of the amorphous and crystalline polymer, respectively. Here, during the formation of the bilayer system 2, T_{mold} in the second run of injection PLLA over PCL was designed to be 30 °C, which was not close to the T_{g} or T_{m} of PLLA and PCL, respectively (≈ 58 °C). On the one hand, the first intimate contact was performed inside of the closed mold while injection molding, but because of not adequate time inside of the mold, the self-diffusion was not followed up. On the other hand, exposure to the $scCO_2$ autoclave as the post-treatment at $T = 45$ °C and $P = 100$ bar provided time for diffusion and motion of macromolecules. In this regard, the result of the T-peel test (Figure 10C, D) revealed the enhancement of the bonding strength from 6 ± 1 N to 15 ± 4 N, before and after the foaming process, respectively. The self-diffusion procedure was also proved by the SEM image of the intersection of the bilayer system 2.

Characterization of pores morphology

Pore morphology of pores structure can be assessed by distinct characterizations including porosity, pore size, pore shape, surface area to volume ratio, interconnectivity, anisotropy, strut thickness and permeability. Estimation of the above-mentioned features is determined by the potential application of the products and calculated by various techniques such as SEM, mercury porosimetry, gas pycnometry and absorption as well as micro-computed tomography (µCT). Fathoming of virtues and pitfalls of each technique equips the researchers with the know-how to combine the aforesaid methods to obtain comprehensive data for analysis. Here, for the bilayer system 1, SEM along with ImageJ software was utilized to evaluate pore size, pore shapes and qualitative interpretation of interconnectivity. Also, the porosity was determined by calculating the apparent density of products before and after the leaching process. For the bilayer system 2, pores shapes, anisotropy and interconnectivity were assessed by SEM. In addition, porosity and pore sizes were computed by µCT.[93] In 2022, a semi-automated pores size MATLAB algorithm, PoreScript, was introduced. This new method was employed in different porous structures generated by various scaffold fabrication methods having different pore sizes and shapes to demonstrate the versatility of this new tool. The result of this PoreScript is comparable with the manual measurement.[94]

In the bilayer system 2, the foamed PCL layer is reinforced by the compact PLLA layer, where the flexural or bending modulus (E_{flex}) of the whole bilayer system 2 is enhanced and distinct in all three directions of the bending. Figure 11 A and B present two positive and negative bending modes, where the dispersion of applied tension and compression strain are varied on the bilayer construct. In these cases, the weld line is parallel to the neutral axis and not essentially overlapping with the weld line. Figure 11C displays the third posture, where the neutral axis is perpendicular to the weld line. Assessment of the incorporation of a layered reinforced agent into bilayer structure requires numerical study such as finite element method to evaluate the optimum thickness ratio of the compact layer to the porous one as well as the location of the compact layer in the foamed product based on the compression and tension stress distribution on the product at the time of utilization.

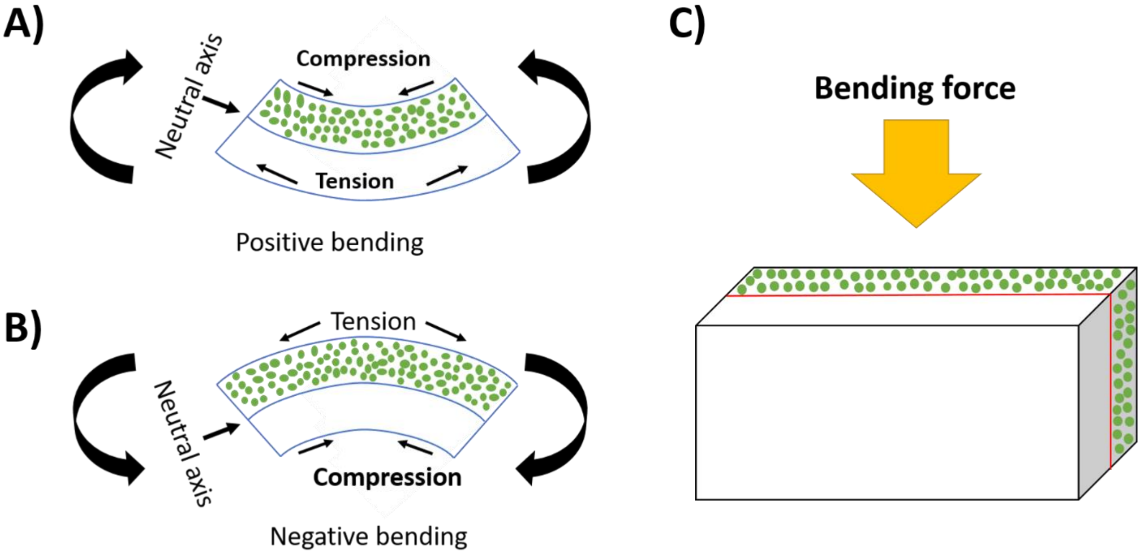

Figure 11. An illustration presenting 3 different modes of bending deformation applied on a bilayer structure, where a compact layer acts as a reinforced agent. In the A and B bending modes, the neutral axis is parallel to the weld line, however, the neutral axis is perpendicular to the weld line in the C state.

Hence, the suggested approaches in this thesis are feasible mass processes for the creation of bilayer porous structure as well as selective-porous layer in multi-materials products. Designing the appropriate die and mold for complex geometry is an advantage of exploiting sequential injection molding for polymers, that are not temperature-sensitive.

System 3

Metal Thin Film- Polymer Compact Layer $10^4 < E1/E2$

Dynamic micro or nano wrinkles are ubiquitous in nature and inspiring for researchers to embed this phenomenon into technologies to create a smart surface. Dynamic wrinkles, where the patterns on the surface are changed in cycles from wrinkles (hierarchical or homogenous) to complete flat and vice versa direction, are explored in bilayer structures, where the thin film surface was chemically functionalized[95], spin-coated by IPN[62]or crosslinked by UV[46]. The aforestated obtained wrinkles appeared and disappeared upon exposure to the solvent, moisture, and heating stimuli. Such wrinkles are reported to be employed in anti-counterfeit tabs, encryption devices, antiglare films, water indicators, optical devices and smart displays. The wrinkles could be tuned by changing the thickness of the thin film, the chemical compounding on the surface or the pre-stain before deposition of the thin film. Nevertheless, the aforementioned wrinkles were not *in-situ* tunable and reversible.

Such dynamic tunable patterns on a surface, where wrinkles could be *in-situ* tunable, were not reported on a bilayer structure composed of a thin metal film and a compliant substrate. This feature can be used for smart surfaces, where altering topographies are needed on the metal/conductive surface employed in optical and electrical fields. In addition, *in-situ* tunable surface roughness on the metal surface is also beneficial for tunable frictional drag in an aerodynamic field and fluid mechanics[96] (Figure 12).

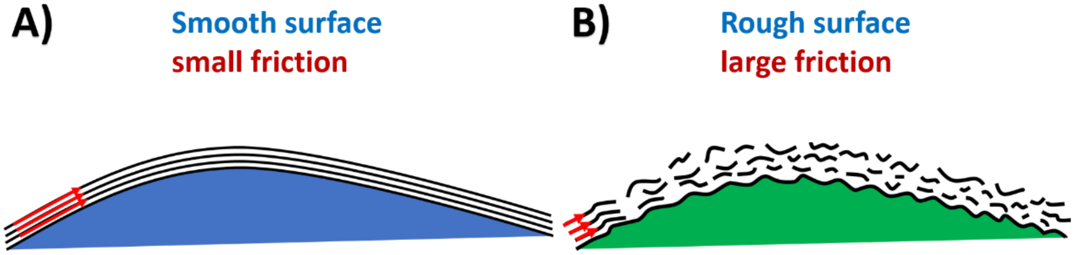

Figure 12. An illustration showing the effect of smooth and rough surfaces on a frictional drag utilizing in an aerodynamic field. As an object moves through a fluid, or as a fluid moves past an object, A) a laminar boundary flow is created on a smooth surface, which is a result of small friction and B) a turbulent boundary flow is formed on a rough/patterned surface originated by large friction.

In the third section of this thesis, the third system was devoted to investigating the possibility of imposing self-assembly wrinkling (on/off switch) on a bilayer construct having a 10 nm gold film sputtered on a 1 mm programmed rbSME of the network of cPEVA.

In the studied system, a bilayer construct including the 10 nm gold film sputtered on the substrate, which was encoded by 6% reversible strain exposed to the 3 thermal cycles, which led to the self-assembly parallel wrinkling upon heating to T_{sep} = 60 °C with the wavelength of 1.5 ± 0.3 µm and amplitude of 240 ± 4 nm. Wrinkles were diminished to an almost flat surface by cooling at 25 °C. The obtained wrinkles were also tunable by altering the temperature considered as T_{sep} in the second curve of DSC correlated to the rbSME, where divided crystalline domains to ADs and SGDs. The obtained wrinkles were homogenous and uniform on the Au surface. In 2019, Wang et al.[68] reported the self-dynamic wrinkles using a wire embedded in the substrate inducing Joule heating (Figure 13A) in the system. Joule heating or ohmic heating is a physical process, in which the energy of electrical current is converted to thermal energy by passing through a resistance. The reported substrate was a SMP with a T_g of 42 °C, programmed by 5% strain in uniaxial direction at 60 °C and fixed at 25 °C. Subsequently, the thin film of 100 nm of Al was sputtered upon the substrate. By exposing the bilayer structure to 60 °C, the recovery occurred and parallel wrinkles appeared on the surface with a wavelength of 7.1 µm and an amplitude of 255 nm. Turning on the DC current of 0.45 A for 3 min via embedded wire and inducing Joule heating into the substrate, local thermal expansion on the SMP led to the erasing of the wrinkles in the local place. Wrinkles appeared again on the Al surface upon turning off the current and cooling the system after 5 min. The reported reversible wrinkle and flat surface was repeated for 2 more cycles. Optical microscopy of the obtained wrinkles also exhibited that, the surface of the Al became almost flat in cycles, with topographies with an amplitude of 25 nm, indicating the general plastic deformation of the metal, which was also observed in the studied system in this thesis. The induced flat surface was local. The non-uniform wrinkles but symmetric amplitude distribution occurred around the center of the heating spot, where the wavelength was constant, but the amplitude was reported 255 nm (same dimension before applying Joule heating) at 4 mm (the location of measurement from the position of heating wire), 175 nm at 3 mm, 83 nm at 2 mm, 61 nm at 1 mm, and 25 nm at the flat surface. The measurement indicated that the induced heating temperature decreased with the distance from the heating source led to the symmetric but non-uniform thermal expansion of the SMP. Such an on/off mode on surfaces was a candidate for a micromirror.

The reported repeatable and reversible wrinkles were similar to the system explored in this thesis, however, in Wang et al.’s work, the reversibility occurred at the local place of inserted wire and not on the whole surface. The mentioned wrinkles were tunable with the classical variation of altering the thickness of the metal film and programmed strains referring to Equations 2 to 4 stated in the introduction chapter.

In the work presented in this thesis, a free-standing reversible multi-pattern was also presented by applying sequential and simultaneously bidirectional programming on a substrate encoded rbSME before sputtering, in which by altering the temperature from 60 °C to 40 °C, the patterns were changed from parallel wrinkles to diamond wrinkles, in two thermal cycles. Such reversible hybrid patterns via altering temperature were correlated to the superposition of formed wrinkles induced by variation of the direction of compression strain originated from TSME and rbSME on the substrate having a broad ΔT_m.

In 2021, Wang et al.[97] reported a non-reversible but hybrid multi-pattern on a surface of bilayer structure having a SMP substrate with a 6% pre-strain programmed and 150 nm of Al film on top. Contrary to their last work, the wire was embedded (Figure 13B) in the substrate in another direction. Applying Joule heating via wire induced local hybrid patterns on the Al surface in a constrained circular form with the center of the heating source exhibiting outer ring pattern and inner spoke pattern. The size of wrinkles was reported adjustable by controlling the heat input, which affected the E_s in the spot of the heating source, consequently altering the ε_c and tuning A and λ.

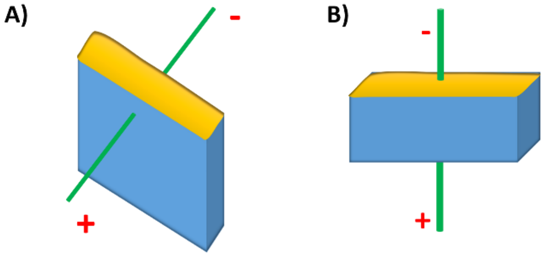

Figure 13. A simple cartoon illustrates the embedment of wire in the substrate inducing Joule heating reported in the literature of A) Wang et al, 2019[68] B) Wang et al, 2021[97].

Zhao et al.[69] investigated the effect of recovery time (t_r) and recovery temperature (T_r) of SME on the formed wrinkles on a bilayer structure having a crosslinked polyethylene (T_g = 105 °C) substrate and a 10 nm Au film. Analyzing the wrinkle dimension in different recovery times from 2s to 10s implied the sharp transition from nanoscale to micro scale at t_r = 5s. SME was programmed in three modes of uniaxial, simultaneously and subsequently biaxial tension at a temperature of 110 °C before the sputtering process. The simultaneously bidirectional release led to a random labyrinth pattern and the subsequent release in bi-directions reached the irreversible patterns with oriented labyrinth patterns. Furthermore, the sequential pre-strain along the same axis and two steps recovery at t_r = 2 s and t_r = 10 s led to the formation of multi-scale hierarchical wrinkles with a microscale wave-like buckle and nanoscale of random wrinkles in one direction.

In addition, reversible multi patterns (parallel wrinkles to herringbone wrinkles) were observed[98] in sequential biaxial release in bilayer structure of a PDMS substrate and crosslinked surface, where loading sequential bidirectional led to the reversible herringbone pattern under a stretching/releasing/re-stretching cycle, while formed labyrinth patterns were non-reversible under simultaneously bidirectional release. However, such reversible sequential release of the aforementioned system was not considered self-assembly as it was dependent on the applied stress.

Supporting a thin metal film by a compliant substrate enhances the elongation of break (ε_b) of the film reported by up to 20% [99], although a comparable free-standing metal thin film rupture was around 1-2%.[100] It is also reported that the E of gold for bulk ($\approx$ 78 GPa) is decreased to $\approx$ 40 GPa for a 10 nm gold film because of the grain-related effect.[101] This synergetic property capacitates biosensors and electronic devices for high compliance and flexibility. Because of the conductivity of the gold metal film in electronic devices under thermo-mechanical behavior, the fatigue behavior of gold metal is investigated by researchers in the electronic field. Dynamic wrinkling on a metal film layer of bilayer structure caused formation of cracks,[102] which are related to the thermomechanical fatigue behavior of metal. The fatigue behavior of metal on substrates is dependent on the thickness of the metal film at the submicron, as the mechanism of behavior is different from the bulk. The fatigue-life time of metal in the film form (where the thickness is less than 1µm) is generally enhanced by decreasing the thickness of the film and reduction of the grain size and dislocation mechanism of the grains in metal.[103] The fatigue test of films can be estimated by micro beam-bending test and cyclic tensile test.[104] Considering spontaneous crack formation on the metal surface while appearing wrinkles, the dynamic wrinkles on metal layers cannot be designed over a large surface area.[50]

Furthermore, the sputtering method for deposition of metal film induces heating and consequently thermal compression upon the substrate.[105] Depending on the T_{sw} or T_{sep} and T_{reset} of the substrate and the sort of programming of the substrate, this method of deposition influences some instability on the oriented crystalline of the substrate inducing thermal compression. This effect is a challenge to consider for a programmed substrate, where the thermal transition temperatures are around room temperature.

Exploiting self-assembly reversible patterns in the direction of medical and health technology requires a substrate showing rbSME at body temperature. In this regard, two semi-crystalline copolymer networks from a combination of oligomers of oligo(ε-caprolactone) (OCL) with different average molecular mass ($\overline{M_n}$) and *n*-butyl acrylate (BA) were synthesized. A network of C(2,15)B25 containing a mixture of OCLs with $\overline{M_n}$ of 2.3 and 15.2 kg/mol and 25 wt% BA revealed a broad ΔT_m ranging from 2 °C to 50 °C. The second network, C(3,4,8)B25, was synthesized from a mixture of OCLs with $\overline{M_n}$ of 3, 3.8,7.5 kg/mol and 25 wt% BA showed also a broad ΔT_m ranging from -10 °C to 37 °C. Both networks were programmed (ε_{prog} = 40%) at T_{high} = 60 °C showing rbSME at physiological temperature (T = 37 °C), in which ε_{rev} of network C(2,15)B25 and C(3,4,8)B25 were quantified as 3.2 ± 0.1% and 17.1 ± 0.1%, respectively. A degree of crystallinity (DOC) of 24% at T_{low} = 0 °C was quantified for C(3,4,8)B25, where at 37 °C was shown 0% (amorphous state). However, C(2,15)B25 showed a DOC of 22% at T_{low} = 0 °C and 7% at T = 37 °C. The increased difference in DOC between T_{low} and switching temperature (37 °C) for C(3,4,8)B25 indicated an increased quantity of ADs, which led to the higher ε_{rev}. This work also highlighted the point that ADs could also be kept oriented in the viscoelastic state, which was attributed to the orientational memory of the molten ADs, where the switching temperature exceeded $T_{m,\ offset}$. In this regard, the triggering temperature of rbSME can be adjusted not only with a broad ΔT_m peak, but also in the temperature range close to or even above $T_{m,\ offset}$. These networks are considered the first co-polymer networks showing rbSME around body temperature.[106] Nevertheless, very few semi-crystalline networks were realized, where rbSME can be triggered at 37 °C. In 2017, Yang et al.[78] reported two copolymer networks of methacrylate-terminated poly(ethylene glycol) (PEG) with broad molecular weight distributions and 20 wt.% BA, where the transition temperatures were adjusted to the body temperature. A network of PEG -2, 4, 10 kDa and PEG-2, 6, 10 kDa displayed broad ΔT_ms ranging from 5 °C to 50 °C and 10 °C to 51 °C, respectively. Both networks were programmed (ε_{prog} = 20%) at T = 75 °C and exhibited rbSM (0 °C ↔ 37 °C) with ε_{rev} of 8.2% for PEG-2, 4, 10 kDa network and 6.2% for PEG-2, 6, 10 kDa network. In 2021[79], random crosslinked hydrophobic polytetrahydrofuran (PTHF) and PEG networks exhibited rbSME (-15 °C ↔ 37 °C), in which ε_{rev} reached up to 25.2% (ε_{prog} = 50% at T_{prog} = 50 °C).

This work highlighted that combination of an individual layer with distinct porosity/moduli within a bilayer system could fabricate new functions exhibited either nano/micro scale patterns on the surface of bilayer or acted as the reinforcing agent in a special bending deformation.

Chapter 10. Summary and Outlook

In this thesis, generating new functions in bilayer structures through combining layers of different moduli and/or porosity was studied. Besides, for each layered construct, a suitable processing technique was developed.

The focus was on the formation of the three distinct bilayer constructs: the bilayer porous structure, the porous layer supported by the compact layer, and the bilayer structure, where one layer is a metal film deposited on a polymeric substrate.

Firstly, a bilayer porous structure composed of two different PUs was formed via melt-blending of PVA and PUs in a co-continuous phase, sequential injection molding and immersion in water washing out PVA, subsequently. Pore size in both layers ranged from 1 µm to 100 µm with an average of 22 ± 10 µm at a porosity of 50 ± 5% in combination with a high interconnectivity. The pore diameters were adjusted by applying annealing treatment before the leaching step. The average pore diameters were decreased to 20 ± 10 µm and 15 ± 8 µm after applying annealing treatment at 110 °C and 130 °C for one hour, respectively quantified by SEM and ImageJ software. Such bilayer constructs could serve as a model system for determining structure-property relationships considering porosity, pore sizes and mechanical properties enabling a knowledge-based design of porous layered structures.

The second bilayer construct was fabricated by sequential injection molding of PCL and PLLA and soaking into the $scCO_2$ autoclave at T = 45 °C and P = 100 bar led to the selectively foaming of PCL layer, while PLLA layer remained compact. The obtained foamed PCL layer was a porous core and a skin layer, where the porosity of PCL was calculated as 80 ± 5%. Increasing the soaking time from 1 h to 4 h at the constant condition altered the pore shape of foamed PCL layer from circular shape with the average size of 190 ± 90 µm to anisotropic lamellar shape having pores diameter of 220 ± 90 µm quantified by SEM and μCT. Altering the shape of pores affected the compression elastic modulus from 2300 ± 500 kPa to 700 ± 100 kPa. In addition, foaming process affected the mechanical properties of the compact PLLA layer by decreasing Young's modulus and increasing elongation at break. Although introducing pores decreases the density and subsequently the mechanical strength, having a compact layer supported the porous layer acts as a reinforcement agent in bending deformation to prevent the yielding of the porous layer. This construct might be a model for such a reinforced porous structure.

In both aforestated studies, an environmental pollution factor was considered by avoiding utilizing toxic solvents in the formation processes.

To apply above methods to complex geometries, a new design of a mold for injection molding is required. Using a selectively foaming technique can also be applied in three-layer structures, where the middle layer would be foamed, which would lead to the formation of sandwich structure without using any organic solvent.

The third bilayer structure in this thesis was composed of a cPEVA substrate and a 10 nm gold film. By encoding rbSME on the cPEVA substrate via uniaxial programming of 50% strain at 100 °C prior to the sputtering of the gold film, the *in-situ* reversible wrinkles on a nanoscale were achieved. These on/off wrinkles were observed in stress-free thermal cycles between 25 °C and 60 °C, where the dimension of the obtained parallel wrinkles on the surface of the gold film at 60 °C was quantified with $\lambda = 1.5 \pm 0.3$ µm and $A = 240 \pm 40$ nm. In addition, applying such a concept on a pre-patterned surface resulted in the creation of the reversible multi-patterns where the patterns fluctuated *in-situ* between diamond-like patterns at 60 °C and parallel wrinkles at 25 °C. Altering T_{sep} changed the $\varepsilon_{\mathrm{rev}}$ of the substrate and subsequently adjusted the dimension of the wrinkles.

The SEM platform with a heating and cooling stage was used as the main platform to observe the obtained wrinkles and the wrinkle were quantified by applying 2DFFT method on the obtained SEM images.

Appearing patterns on surfaces affects any surface-related properties. Such dynamic wrinkles can be considered a smart surface and might have potential in optical grating, stretchable electronics, smart adhesion, anti-fouling, anti-counterfeiting products, anti-glare film, smart windows for energy saving in architecture and vehicle application and triboelectric nanogenerator, where micro/nano structures on surface increase charge.

Since gold is recognized as non-toxic material, such topographies formed on studied bilayer structure might be employed as a guidance cue for controlling cell behavior. To do so, a substrate is required to show rbSME around body temperature. In the last phase of this work, copolymer networks were synthesized from a mixture of crystallizable OCLs with different $\overline{M}_{\mathrm{n}}$s and BA. OCLs with lower $\overline{M}_{\mathrm{n}}$s hindered the crystallization of OCLs with high $\overline{M}_{\mathrm{n}}$s, which resulted in the shift of the T_{m} to the lower temperature ranges and tuning the triggering temperature around 37 °C. Both networks also revealed broad ΔT_{m}s from 2 °C to 50 °C and -10 °C to 37 °C. In cyclic, thermomechanical experiments, rbSME was implemented in copolymer networks by programming of networks at T_{high} = 60 °C and $\varepsilon_{\mathrm{prog}}$ = 40% and was displayed between 20 °C and 37 °C. There is only a big challenge that remained for utilizing this specific network in wrinkling studies. The sputtering technique inducing heating during the deposition process of the gold film erased the encoded programming of the substrate, subsequently diminishing the rbSME of the substrate. To overcome this problem, a new technique of deposition of the metal film along with controlling the induced temperature while sputtering is demanded.

References

1. Holzapfel GA, Sommer G, Gasser CT, Regitnig P. Determination of layer-specific mechanical properties of human coronary arteries with nonatherosclerotic intimal thickening and related constitutive modeling. *Am J Physiol - Hear Circ Physiol*. 2005;289(5 58-5):2048-2058. doi:10.1152/ajpheart.00934.2004
2. M.D Humzah R. S. Human intervertebral disc: Structure and function. *Anat Rec*. 1988;220(4):337-356. http://dx.doi.org/10.1002/ar.1092200402
3. Genzer J, Groenewold J. Soft matter with hard skin: From skin wrinkles to templating and material characterization. *Soft Matter*. 2006;2(4):310. doi:10.1039/b516741h
4. O'Shea TM, Miao X. Bilayered scaffolds for osteochondral tissue engineering. *Tissue Eng Part B Rev*. 2008;14(4):447-464. doi:10.1089/ten.teb.2008.0327
5. Harley B a, Lynn AK, Wissner-Gross Z, Bonfield W, Yannas I V, Gibson LJ. Design of a multiphase osteochondral scaffold III: Fabrication of layered scaffolds with continuous interfaces. *J Biomed Mater Res A*. 2010;92(3):1078-1093. doi:10.1002/jbm.a.32387
6. Titov VN. The functional role of arterial intima. Endogenous and exogenous pathogens and specificity of atheromatosis as an inflammation. *Klin Lab Diagn*. 2003;(2):23—4, 33—7. http://europepmc.org/abstract/MED/12688211
7. Sarkar S, Schmitz-Rixen T, Hamilton G, Seifalian AM. Achieving the ideal properties for vascular bypass grafts using a tissue engineered approach: a review. *Med Biol Eng Comput*. 2007;45(4):327-336. doi:10.1007/s11517-007-0176-z
8. Behl M, Razzaq MY, Lendlein A. Multifunctional shape-memory polymers. *Adv Mater*. 2010;22(31):3388-3410. doi:10.1002/adma.200904447
9. Lendlein A, Balk M, Tarazona NA, Gould OEC. Bioperspectives for Shape-Memory Polymers as Shape Programmable, Active Materials. *Biomacromolecules*. 2019;20(10):3627-3640. doi:10.1021/acs.biomac.9b01074
10. Lendlein A, Trask RS. Multifunctional materials: Concepts, function-structure relationships, knowledge-based design, translational materials research. *Multifunct Mater*. 2018;1(1). doi:10.1088/2399-7532/aada7b
11. Wischke C, Neffe AT, Hanh BD, et al. A multifunctional bilayered microstent as glaucoma drainage device. *J Control Release*. 2013;172(3):1002-1010. doi:10.1016/j.jconrel.2013.10.021
12. Hutmacher DW, Schantz JT, Xu C, Lam F, Tan KC, Lim TC. State of the art and future directions of scaffold-based bone engineering from a biomaterials perspective. *J Tissue Eng Regen Med*. 2007;1(June):245-260. doi:10.1002/term
13. Hutmacher DW, Schantz T, Zein I, Ng KW, Teoh SH, Tan KC. Mechanical properties and cell cultural response of polycaprolactone scaffolds designed and fabricated via fused deposition modeling. *J Biomed Mater Res*. 2001;55(2):203-216. http://www.ncbi.nlm.nih.gov/pubmed/11255172
14. Mikos a G, Sarakinos G, Leite SM, Vacanti JP, Langer R. Laminated three-dimensional

biodegradable foams for use in tissue engineering. *Biomaterials*. 1993;14(5):323-330. http://www.ncbi.nlm.nih.gov/pubmed/8507774

15. Mao JS, Zhao LG, Yin YJ, Yao K De. Structure and properties of bilayer chitosan–gelatin scaffolds. *Biomaterials*. 2003;24(6):1067-1074. http://www.ncbi.nlm.nih.gov/pubmed/12504529

16. Ghosh S, Viana JC, Reis RL, Mano JF. Bi-layered constructs based on poly(l-lactic acid) and starch for tissue engineering of osteochondral defects. *Mater Sci Eng C*. 2008;28(1):80-86. doi:10.1016/j.msec.2006.12.012

17. Yunos DM, Ahmad Z, Salih V, Boccaccini a R. Stratified scaffolds for osteochondral tissue engineering applications: electrospun PDLLA nanofibre coated Bioglass®-derived foams. *J Biomater Appl*. 2013;27(5):537-551. doi:10.1177/0885328211414941

18. Reignier J, Huneault M. Preparation of interconnected poly(ε-caprolactone) porous scaffolds by a combination of polymer and salt particulate leaching. *Polymer (Guildf)*. 2006;47(13):4703-4717. doi:10.1016/j.polymer.2006.04.029

19. Sca M, Mendibil X, Virginia S, Viteri D, Ugartemendia JM. High Throughput Manufacturing of Bio-Resorbable. *Polymers (Basel)*. 2020;12(34).

20. Washburn NR, Simon CG, Tona A, Elgendy HM, Karim A, Amis EJ. Co-extrusion of biocompatible polymers for scaffolds with co-continuous morphology. *J Biomed Mater Res*. 2001;60:21-29. doi:10.1002/jbm.10049

21. Oh S. Fabrication and characterization of hydrophilic poly(lactic-co-glycolic acid)/poly(vinyl alcohol) blend cell scaffolds by melt-molding particulate-leaching method. *Biomaterials*. 2003;24(22):4011-4021. doi:10.1016/S0142-9612(03)00284-9

22. Sarazin P, Roy X, Favis BD. Controlled preparation and properties of porous poly(L-lactide) obtained from a co-continuous blend of two biodegradable polymers. *Biomaterials*. 2004;25(28):5965-5978. doi:10.1016/j.biomaterials.2004.01.065

23. Sun ZB, Song YN, Ma GQ, et al. Imparting Gradient and Oriented Characters to Cocontinuous Structure for Improving Integrated Performance. *Macromol Chem Phys*. 2021;222(10):1-10. doi:10.1002/macp.202100012

24. Liu Q, Liu Y, Jiang C, Zheng S. Modeling and simulation of weld line location and properties during injection molding based on viscoelastic constitutive equation. *Rheol Acta*. 2020;59(2005):109121. doi:https://doi.org/10.1007/s00397-019-01182-8

25. Vendan, S.A., Natesh, M., Garg, A., Gao L. Polymer Welding Techniques and Its Evolution. In: *Onfluence of Multidisciplinary Sciences for Polymer Joining.* Springer, Singapore; 2019. doi:https://doi.org/10.1007/978-981-13-0626-6_2

26. Haugen H, Will J, Fuchs W, Wintermantel E. A Novel Processing Method for Injection-Molded Polyether – Urethane Scaffolds . Part 1 : Processing. *J Biomed Mater Res B Appl Biomater*. 2006;77(1):65-72. doi:10.1002/jbm.b.30396

27. Jiang J, Li Z, Yang H, Wang X, Li Q, Turng L-S. Microcellular injection molding of polymers: a review of process know-how, emerging technologies, and future directions. *Curr Opin Chem Eng*. 2021;33:100694. doi:10.1016/j.coche.2021.100694

28. Ding Y, Hassan MH, Bakker O, Hinduja S, Bártolo P. A review on microcellular injection moulding. *Materials (Basel)*. 2021;14(15). doi:10.3390/ma14154209

29. Guarino V, Guaccio A, Ambrosio L. Manipulating co-continuous polymer blends to create pcl scaffolds with fully interconnected and anisotropic pore architecture. *J Appl Biomater Biomech*. 2011;9(1):34-39. doi:10.5301/JABB.2011.6473

30. Kramschuster A, Turng L-S. An injection molding process for manufacturing highly porous and interconnected biodegradable polymer matrices for use as tissue engineering scaffolds. *J Biomed Mater Res B Appl Biomater*. 2010;92(2):366-376. doi:10.1002/jbm.b.31523

31. Quirk R a., France RM, Shakesheff KM, Howdle SM. Supercritical fluid technologies and tissue engineering scaffolds. *Curr Opin Solid State Mater Sci*. 2004;8(3-4):313-321. doi:10.1016/j.cossms.2003.12.004

32. Goel SK, Beckman EJ. Generation of Microcellular Polymeric Foams Using Supercritical Carbon Dioxide. I: Effect of Pressure and Temperature on. *Polym Eng Sci*. 1994;34(74):1137-1147.

33. Chen C-X, Liu Q-Q, Xin X, Guan Y-X, Yao S-J. Pore formation of poly(ε-caprolactone) scaffolds with melting point reduction in supercritical CO 2 foaming. *J Supercrit Fluids*. 2016;117:279-288. doi:10.1016/j.supflu.2016.07.006

34. Song C, Luo Y, Liu Y, et al. Fabrication of PCL Scaffolds by Supercritical CO2 Foaming Based on the Combined Effects of Rheological and Crystallization Properties. *Polymers (Basel)*. 2020;12(4):780. doi:10.3390/polym12040780

35. Guo H, Jiang J, Li Z, et al. Solid-State Supercritical CO2 Foaming of PCL/PLGA Blends: Cell Opening and Compression Behavior. *J Polym Environ*. 2020;28(7):1880-1892. doi:10.1007/s10924-020-01732-9

36. Georgiou G, Mathieu L, Pioletti DP, et al. Polylactic Acid – Phosphate Glass Composite Foams as Scaffolds for Bone Tissue Engineering. *J Biomed Mater Res Part B*. 2006;80:322-331. doi:10.1002/jbmb

37. Guarino V, Causa F, Taddei P, et al. Polylactic acid fibre-reinforced polycaprolactone scaffolds for bone tissue engineering. *Biomaterials*. 2008;29(27):3662-3670. doi:10.1016/j.biomaterials.2008.05.024

38. Kang Y, Scully A, Young D a, et al. Enhanced mechanical performance and biological evaluation of a PLGA coated β-TCP composite scaffold for load-bearing applications. *Eur Polym J*. 2011;47(8):1569-1577. doi:10.1016/j.eurpolymj.2011.05.004

39. Park J-E, Todo M. Development of layered porous poly(l-lactide) for bone regeneration. *J Mater Sci*. 2010;45(14):3966-3968. doi:10.1007/s10853-010-4564-7

40. Sanz-Horta R, Elvira C, Gallardo A, Reinecke H, Rodríguez-Hernández J. Fabrication of 3d-printed biodegradable porous scaffolds combining multi-material fused deposition modeling and supercritical Co2 techniques. *Nanomaterials*. 2020;10(6). doi:10.3390/nano10061080

41. Song C, Li S, Zhang J, et al. Controllable fabrication of porous PLGA/PCL bilayer membrane for GTR using supercritical carbon dioxide foaming. *Appl Surf Sci*. 2019;472:82-92. doi:10.1016/j.apsusc.2018.04.059

42. Higham TE, Russell AP, Niewiarowski PH, Wright A, Speck T. The Ecomechanics of Gecko Adhesion: Natural Surface Topography, Evolution, and Biomimetics. *Integr Comp Biol*. 2019;59(1):148-167. doi:10.1093/icb/icz013

43. Ensikat HJ, Ditsche-Kuru P, Neinhuis C, Barthlott W. Superhydrophobicity in perfection: the outstanding properties of the lotus leaf. *Beilstein J Nanotechnol*. 2011;2:152-161. doi:10.3762/bjnano.2.19

44. Wu K, Sun Y, Yuan H, Zhang J, Liu G, Sun J. Harnessing Dynamic Wrinkling Surfaces for Smart Displays. *Nano Lett*. 2020;20(6):4129-4135. doi:10.1021/acs.nanolett.9b05279

45. Dean B, Bhushan B. Shark-skin surfaces for fluid-drag reduction in turbulent flow: a review. *Philos Trans R Soc A Math Phys Eng Sci*. 2010;368(1929):4775-4806. doi:10.1098/rsta.2010.0201

46. Songshan Zeng,Rui Li,Stephan G. Freire,Vivian M. M. Garbellotto,Emily Y. Huang,Andrew T. Smith,Cong Hu,William R. T. Tait,Zichao Bian,Guoan Zheng,Dianyun Zhang LS. Moisture-Responsive Wrinkling Surfaces with Tunable Dynamics. *Adv Mater*. 2017;29(24):1700828. doi:https://doi.org/10.1002/adma.201700828

47. Ma L, He L, Ni Y. Tunable hierarchical wrinkling: From models to applications. *J Appl Phys*. 2020;127(11). doi:10.1063/1.5143651

48. Ware CS, Smith-Palmer T, Peppou-Chapman S, et al. Marine Antifouling Behavior of Lubricant-Infused Nanowrinkled Polymeric Surfaces. *ACS Appl Mater Interfaces*. 2018;10(4):4173-4182. doi:10.1021/acsami.7b14736

49. Bae HJ, Bae S, Park C, et al. Biomimetic Microfingerprints for Anti-Counterfeiting Strategies. *Adv Mater*. 2015;27(12):2083-2089. doi:10.1002/adma.201405483

50. Raj SS, Mathew RM, Nair Y, S. T. A, T. P. V. Fabrication and Applications of Wrinkled Soft Substrates: An Overview. *ChemistrySelect*. 2022;7(16):1-6. doi:10.1002/slct.202200714

51. Nomin-Erdene Oyunbaatar, Pooja P. Kanade D-WL. Stress-assisted gold micro-wrinkles on a polymer cantilever for cardiac tissue engineering. *Colloids Surfaces B Biointerfaces*. 2022;209:112210. doi:https://doi.org/10.1016/j.colsurfb.2021.112210

52. IM S, HUANG R. Wrinkle patterns of anisotropic crystal films on viscoelastic substrates. *J Mech Phys Solids*. 2008;56(12):3315-3330. doi:10.1016/j.jmps.2008.09.011

53. Park J-Y, Chae HY, Chung C-H, et al. Controlled wavelength reduction in surface wrinkling of poly(dimethylsiloxane). *Soft Matter*. 2010;6(3):677. doi:10.1039/b916603c

54. Chen Z, Young Kim Y, Krishnaswamy S. Anisotropic wrinkle formation on shape memory polymer substrates. *J Appl Phys*. 2012;112(12):124319. doi:10.1063/1.4770483

55. Chen X, Hutchinson JW. A family of herringbone patterns in thin films. *Scr Mater*. 2004;50(6):797-801. doi:10.1016/j.scriptamat.2003.11.035

56. Wang Z, Hansen C, Ge Q, et al. Programmable, pattern-memorizing polymer surface. *Adv Mater*. 2011;23(32):3669-3673. doi:10.1002/adma.201101571

57. Xie T. Tunable polymer multi-shape memory effect. *Nature*. 2010;464(7286):267-270. doi:10.1038/nature08863

58. Lin G, Li J, Xu Z, Ge D, Sun W, Chen P. Hierarchical Surface Patterns via Global Wrinkling on Curved Substrate for Fluid Drag Control. *Adv Mater Interfaces*. 2021;8(1):2001489. doi:10.1002/admi.202001489

59. Al-Rashed R, López Jiménez F, Marthelot J, Reis PM. Buckling patterns in biaxially pre-stretched bilayer shells: wrinkles, creases, folds and fracture-like ridges. *Soft Matter*. 2017;13(43):7969-7978. doi:10.1039/C7SM01828B

60. Li F, Hou H, Yin J, Jiang X. Near-infrared light–responsive dynamic wrinkle patterns. *Sci Adv*. 2018;4(4). doi:10.1126/sciadv.aar5762

61. Zong C, Zhao Y, Ji H, et al. Tuning and Erasing Surface Wrinkles by Reversible Visible-Light-Induced Photoisomerization. *Angew Chemie Int Ed*. 2016;55(12):3931-3935. doi:10.1002/anie.201510796

62. Zhou L, Ma T, Li T, Ma X, Yin J, Jiang X. Dynamic Interpenetrating Polymer Network (IPN) Strategy for Multiresponsive Hierarchical Pattern of Reversible Wrinkle. *ACS Appl Mater Interfaces*. 2019;11(17):15977-15985. doi:10.1021/acsami.8b22216

63. van den Ende D, Kamminga J-D, Boersma A, Andritsch T, Steeneken PG. Voltage-Controlled Surface Wrinkling of Elastomeric Coatings. *Adv Mater*. 2013;25(25):3438-3442. doi:10.1002/adma.201300459

64. Wang Y, Xiao J. Programmable, reversible and repeatable wrinkling of shape memory polymer thin films on elastomeric substrates for smart adhesion. *Soft Matter*. 2017;13(31):5317-5323. doi:10.1039/c7sm01071k

65. Li W, Liu Y, Leng J. Harnessing Wrinkling Patterns Using Shape Memory Polymer Microparticles. *ACS Appl Mater Interfaces*. 2021;13(19):23074-23080. doi:10.1021/acsami.1c00623

66. SUN L, ZHAO Y, HUANG WM, PURNAWALI H, FU YQ. WRINKLING ATOP SHAPE MEMORY MATERIALS. *Surf Rev Lett*. 2012;19(02):1250010. doi:10.1142/S0218625X12500102

67. SUN L, WANG TX, BIN MOHD ZAKEE MHI, BIN ROSLI MS, LEE YX, HUANG WM. SELF-SURFACE WRINKLING ATOP ACRYLONITRILE BUTADIENE STYRENE (ABS) VIA HEATING-RESPONSIVE SHAPE MEMORY EFFECT. *Surf Rev Lett*. 2019;26(08):1950044. doi:10.1142/S0218625X19500446

68. Wang Y, Villada A, Zhai Y, et al. Tunable surface wrinkling on shape memory polymers with application in smart micromirror. *Appl Phys Lett*. 2019;114(19):1-6. doi:10.1063/1.5096767

69. Zhao L, Zhang L, Zhao J, et al. Engineering Surface Patterns with Shape Memory Polymers: Multiple Design Dimensions for Diverse and Hierarchical Structures. *ACS Appl Mater Interfaces*. 2019;11(1):1563-1570. doi:10.1021/acsami.8b15535

70. Hu J, Zhu Y, Huang H, Lu J. Recent advances in shape–memory polymers: Structure, mechanism, functionality, modeling and applications. *Prog Polym Sci*. 2012;37(12):1720-1763. doi:10.1016/j.progpolymsci.2012.06.001

71. Lendlein A, Gould OEC. Reprogrammable recovery and actuation behaviour of shape-memory polymers. *Nat Rev Mater*. 2019;4(2):116-133. doi:10.1038/s41578-018-0078-8

72. Behl M, Kratz K, Noechel U, Sauter T, Lendlein A. Temperature-memory polymer actuators. *Proc Natl Acad Sci U S A*. 2013;2013:1-5. doi:10.1073/pnas.1301895110

73. Westbrook KK, Mather PT, Parakh V, et al. Two-way reversible shape memory effects in a free-standing polymer composite. *Smart Mater Struct*. 2011;065010. doi:10.1088/0964-1726/20/6/065010

74. Wang K, Jia Y, Zhu XX. Two-Way Reversible Shape Memory Polymers Made of Cross-Linked Cocrystallizable Random Copolymers with Tunable Actuation Temperatures. *Macromolecules*. 2017;50(21):8570-8579. doi:10.1021/acs.macromol.7b01815

75. Behl M, Kratz K, Zotzmann J, Nöchel U, Lendlein A. Reversible Bidirectional Shape-Memory Polymers. *Adv Mater*. 2013;25(32):4466-4469. doi:10.1002/adma.201300880

76. Gao Y, Liu W, Zhu S. Reversible Shape Memory Polymer from Semicrystalline Poly(ethylene- co -vinyl acetate) with Dynamic Covalent Polymer Networks. *Macromolecules*. 2018;51(21):8956-8963. doi:10.1021/acs.macromol.8b01724

77. Chen, YujieChen, ChiRehman HU. Shape-Memory Polymeric Artificial Muscles: Mechanisms, Applications and Challenges. *Molecules*. 2020;25(18):4246. doi:10.3390/molecules25184246

78. Yang G, Liu X, Tok AIY, Lipik V. Body temperature-responsive two-way and moisture-responsive one-way shape memory behaviors of poly(ethylene glycol)-based networks. *Polym Chem*. 2017;8(25):3833-3840. doi:10.1039/c7py00786h

79. Liang R, Yu H, Wang L, et al. Triple and Two-Way Reversible Shape Memory Polymer Networks with Body Temperature and Water Responsiveness. *Chem Mater*. 2021;33(4):1190-1200. doi:10.1021/acs.chemmater.0c03860

80. Sauter T, Lützow K, Schossig M, et al. Shape-Memory Properties of Polyetherurethane Foams Prepared by Thermally Induced Phase Separation. *Adv Eng Mater*. Published online May 24, 2012:n/a-n/a. doi:10.1002/adem.201200127

81. Altpeter H, Bevis MJ, Grijpma DW, Feijen J. Non-conventional injection molding of poly(lactide) and poly(epsilon-caprolactone) intended for orthopedic applications. *J Mater Sci Mater Med*. 2004;15(2):175-184. http://www.ncbi.nlm.nih.gov/pubmed/15330053

82. Saatchi M, Behl M, Lendlein A. Manufacturing and characterization of controlled foaming of single layers in bilayer constructs differing in pore morphology. *Macromol Symp*. 2013;334(1):33-39. doi:10.1002/masy.201300151

83. Saatchi M, Behl M, Lendlein A. Double layer porous structures by an injection molding/particulate leaching approach. *Macromol Symp*. 2014;346(1):100-107. doi:10.1002/masy.201400158

84. Chen Y, Chen C, Rehman HU, et al. Shape-Memory Polymeric Artificial Muscles: Mechanisms, Applications, and Challenges. *Molecules*. 2020;25(18):4246. doi:10.3390/molecules25184246

85. Kramschuster A, Turng L-S. An injection molding process for manufacturing highly porous and interconnected biodegradable polymer matrices for use as tissue engineering scaffolds. *J Biomed Mater Res B Appl Biomater*. 2010;92(2):366-376. doi:10.1002/jbm.b.31523

86. Ten E, Jiang L, Zhang J, Wolcott MP. Mechanical performance of polyhydroxyalkanoate (PHA)-based biocomposites. In: *Biocomposites*. Elsevier; 2015:39-52. doi:10.1016/B978-1-78242-373-7.00008-1

87. Kuang T, Chen F, Chang L, et al. Facile preparation of open-cellular porous poly (l-lactic acid) scaffold by supercritical carbon dioxide foaming for potential tissue engineering applications. *Chem Eng J*. 2017;307:1017-1025. doi:10.1016/j.cej.2016.09.023

88. Muñoz-Bonilla A, Fernández-García M, Rodríguez-Hernández J. Towards hierarchically ordered functional porous polymeric surfaces prepared by the breath figures approach. *Prog Polym Sci*. 2014;39(3):510-554. doi:10.1016/j.progpolymsci.2013.08.006

89. Karimi M, Heuchel M, Weigel T, Schossig M, Hofmann D, Lendlein A. Formation and size distribution of pores in poly(ε-caprolactone) foams prepared by pressure quenching using supercritical CO2. *J Supercrit Fluids*. 2012;61:175-190. doi:10.1016/j.supflu.2011.09.022

90. Harte AM, Namara JFM. Overinjection of thermoplastic composites I . Processing and testing of components. *J Mater Process Technol*. 2007;182(1-3):12-20. doi:https://doi.org/10.1016/j.jmatprotec.2006.06.016.

91. Zhang X, Jiang G, Wu H, Guo S. Effect of the temperature gradient on the interfacial strength of polyethylene/polyamide 6 during the sequential injection molding. *High Perform Polym*. 2014;26(2):135-143. doi:10.1177/0954008313501531

92. Giusti R, Lucchetta G. Modeling the Adhesion Bonding Strength in Injection Overmolding of Polypropylene Parts. *Polymers (Basel)*. 2020;12(9):2063. doi:10.3390/polym12092063

93. Ho ST, Hutmacher DW. A comparison of micro CT with other techniques used in the characterization of scaffolds. *Biomaterials*. 2006;27(8):1362-1376. doi:10.1016/j.biomaterials.2005.08.035

94. Jenkins D, Salhadar K, Ashby G, et al. PoreScript: Semi-automated pore size algorithm for scaffold characterization. *Bioact Mater*. 2022;13:1-8. doi:10.1016/j.bioactmat.2021.11.006

95. Carmen M. González-Henríquez, Gonzalo E. Medel-Molina, Fernando E. Rodríguez-Umanzor, Claudio Terraza Inostroza, Mauricio A. Sarabia-Vallejos JR-H. Thermoresponsive microwrinkled hydrogel surfaces with modulated chemical composition. *Polymer (Guildf)*. 2021;231:124109. doi:https://doi.org/10.1016/j.polymer.2021.124109

96. Bai T, Liu J, Zhang W, Zou Z. Effect of surface roughness on the aerodynamic performance of turbine blade cascade. *Propuls Power Res*. 2014;3(2):82-89. doi:10.1016/j.jppr.2014.05.001

97. Wang Y, Xiao J. Confined thin film wrinkling on shape memory polymer with hybrid surface morphologies. *Acta Mech Sin*. 2021;37(7):1063-1071. doi:10.1007/s10409-021-01106-x

98. Yin J, Yagüe JL, Boyce MC, Gleason KK. Biaxially Mechanical Tuning of 2-D Reversible and Irreversible Surface Topologies through Simultaneous and Sequential Wrinkling. *ACS Appl Mater Interfaces*. 2014;6(4):2850-2857. doi:10.1021/am4054207

99. Li T, Huang Z, Suo Z, Lacour SP, Wagner S. Stretchability of thin metal films on elastomer substrates. *Appl Phys Lett*. 2004;85(16):3435. doi:10.1063/1.1806275

100. Lacour SP, Chan D, Wagner S, Li T, Suo Z. Mechanisms of reversible stretchability of thin metal films on elastomeric substrates. *Appl Phys Lett*. 2006;88(20):204103. doi:10.1063/1.2201874

101. Plank H, Güntner R, Scherf U, List EJW. The influence of the metal grain size on polymer/metal bilayer wrinkling. *Soft Matter*. 2007;3(6):713. doi:10.1039/b617211n

102. Wu K, Xia Y, Zhang DK, et al. Fatigue-free Cu films on wrinkled soft substrates. *Thin Solid Films*. 2022;746:139137. doi:10.1016/j.tsf.2022.139137

103. Luo X, Zhang B, Zhang G. Fatigue of metals at nanoscale: Metal thin films and conductive interconnects for flexible device application. *Nano Mater Sci*. 2019;1(3):198-207. doi:10.1016/j.nanoms.2019.02.003

104. Kraft O, Schwaiger R, Wellner P. Fatigue in thin films : lifetime and damage formation. *Mater Sci Eng A*. 2001;321:919-923.

105. Yu S, Sun Y, Li S, Ni Y. Harnessing fold-to-wrinkle transition and hierarchical wrinkling on soft material surfaces by regulating substrate stiffness and sputtering flux. *Soft Matter*. 2018;14(32):6745-6755. doi:10.1039/C8SM01287C

106. Saatchi M, Behl M, Nöchel U, Lendlein A. Copolymer networks from oligo (ε -caprolactone) and n -butyl acrylate enable a reversible bidirectional shape-memory effect at human body temperature. *Macromol Rapid Commun*. 2015;36(10):880-884. doi:10.1002/marc.201400729

107. Genzer J, Groenewold J. Soft matter with hard skin: From skin wrinkles to templating and material characterization. *Soft Matter*. 2006;2(4):310. doi:10.1039/b516741h

108. DAHL-YOUNG KHANGHANQING JIANGYOUNG HUANGAND JOHN A. ROGERS. A Stretchable Form of Single-Crystal Silicon for High-Performance Electronics on Rubber Substrates. *Science (80-)*. 2006;311:208. doi:10.1126/science.11214

109. Uttayarat P, Toworfe GK, Dietrich F, Lelkes PI, Composto RJ. Topographic guidance of endothelial cells on silicone surfaces with micro- to nanogrooves: Orientation of actin filaments and focal adhesions. *J Biomed Mater Res Part A*. 2005;75A(3):668-680. doi:10.1002/jbm.a.30478

110. Chung JY, Youngblood JP, Stafford CM. Anisotropic wetting on tunable micro-wrinkled surfaces. *Soft Matter*. 2007;3(9):1163. doi:10.1039/b705112c

111. Cerda E, Mahadevan L. Geometry and Physics of Wrinkling. *Phys Rev Lett*. 2003;90(7):074302. doi:10.1103/PhysRevLett.90.074302

112. Breid D, Crosby AJ. Effect of stress state on wrinkle morphology. *Soft Matter*. 2011;7(9):4490. doi:10.1039/c1sm05152k

113. Ling Zhang, Weishan Yan, Naikun Gao, Wenyao Luo, Dongdong Zhang, Xi Li DL. Reversible strain-dependent properties of wrinkled Au/PDMS surface. *Mater Lett*. 2018;218:317-320. doi:https://doi.org/10.1016/j.matlet.2018.02.035

114. Wang Y, Xiao J. Programmable, reversible and repeatable wrinkling of shape memory polymer thin films on elastomeric substrates for smart adhesion. *Soft Matter*. 2017;13(31):5317-5323. doi:10.1039/c7sm01071k

115. Efimenko K, Rackaitis M, Manias E, Vaziri A, Mahadevan L, Genzer J. Nested self-similar wrinkling patterns in skins. *Nat Mater*. 2005;4(4):293-297. doi:10.1038/nmat1342

116. Fu C-C, Grimes A, Long M, et al. Tunable Nanowrinkles on Shape Memory Polymer Sheets. *Adv Mater*. 2009;21(44):4472-4476. doi:10.1002/adma.200902294

117. Cai S, Breid D, Crosby a. J, Suo Z, Hutchinson JW. Periodic patterns and energy states of buckled films on compliant substrates. *J Mech Phys Solids*. 2011;59(5):1094-1114.

doi:10.1016/j.jmps.2011.02.001

118. Nöchel U, Kumar UN, Wang K, Kratz K, Behl M, Lendlein A. Triple-shape effect with adjustable switching temperatures in crosslinked poly[ethylene-co-(vinyl acetate)]. *Macromol Chem Phys*. 2014;215(24):2446-2456. doi:10.1002/macp.201400445

119. Yang P, Baker RM, Henderson JH, Mather PT. In vitro wrinkle formation via shape memory dynamically aligns adherent cells. *Soft Matter*. 2013;9(18):4705. doi:10.1039/c3sm00024a

120. Li J, An Y, Huang R, Jiang H, Xie T. Unique aspects of a shape memory polymer as the substrate for surface wrinkling. *ACS Appl Mater Interfaces*. 2012;4(2):598-603. doi:10.1021/am201727a

121. Becker S, Combeaud C, Fournier F, Rodriguez J, Billon N. Biaxial tension on polymer in thermoforming range. *EPJ Web Conf*. 2010;6:25003. doi:10.1051/epjconf/20100625003

122. Spaepen F. Interfaces and stresses in thin films. *Acta Mater*. 2000;48(1):31-42. doi:10.1016/S1359-6454(99)00286-4

123. Li B, Cao YP, Feng XQ, Gao H. Mechanics of morphological instabilities and surface wrinkling in soft materials: A review. *Soft Matter*. 2012;8(21):5728-5745. doi:10.1039/c2sm00011c

124. Ou X, Cakmak M. Influence of biaxial stretching mode on the crystalline texture in polylactic acid films. *Polymer (Guildf)*. 2008;49(24):5344-5352. doi:10.1016/j.polymer.2008.09.053

125. Windischmann H. Intrinsic stress in sputter-deposited thin films. *Crit Rev Solid State Mater Sci*. 1992;17(6):547-596. doi:10.1080/10408439208244586

126. Chen A, Lieu DK, Freschauf L, et al. Shrink-film configurable multiscale wrinkles for functional alignment of human embryonic stem cells and their cardiac derivatives. *Adv Mater*. 2011;23(48):5785-5791. doi:10.1002/adma.201103463

127. Alves NM, Pashkuleva I, Reis RL, Mano JF. Controlling cell behavior through the design of polymer surfaces. *Small*. 2010;6(20):2208-2220. doi:10.1002/smll.201000233

Appendix

100 | Macromol. Symp. 2014, 346, 100–107 DOI: 10.1002/masy.201400158

Double Layer Porous Structures by an Injection Molding/Particulate Leaching Approach

Mersa Saatchi,[1,2,3] *Marc Behl,*[1,3] *Andreas Lendlein**[1,2,3]

Summary: Scaffolds as a temporary substitute for the extracellular matrix should provide interconnected pores and often require a multilayer design to mimic the geometry and biomechanics of the target tissue. Here, it was explored whether bilayer porous structures can be obtained by a process free of organic solvents and how the individual layers contribute to the overall elastic properties. Porous layers were obtained from polyurethane (PU) blends with polyvinyl alcohol (PVA), which were immersed in water after sequential injection molding. Pore sizes in both layers ranged from 1 μm to 100 μm with an average of 22 ± 1 μm at a porosity of 50 ± 5% in combination with a high interconnectivity. The pore sizes were tailored by applying an annealing treatment, while the porosity was kept constant. Mechanical properties of the individual layers and the double layer constructs as determined by tensile tests suggested that the overall elasticity of the compact bilayer construct and porous bilayer construct was in agreement with the predicted overall elasticity according to the rule of mixtures. The porous bilayer model system will serve as a basis for determining structure-property relationships with respect to pore size, porosity as well as mechanical properties of individual layers and in this way enable a knowledge-based design of layered scaffolds.

Keywords: annealing; bilayer scaffold; injection molding; melt blending; polyurethane; particulate leaching material; polymer processing; polymeric scaffold

Introduction

Porous, polymeric scaffolds are explored as temporary substitutes for the extracellular matrix to grow tissues in bioreactors or *in vivo* after implantation.[1–5] The porosity and interconnectivity of the pores enable the mass transfer and influence the cell adhesion and migration of cells into the scaffolds for generation of new tissue.[6,7] Several natural tissues such as blood vessels, intervertebral discs, or osteochondral tissues are organized in layered structures, in which each layer has specific biomechanical properties to perform a physiological function. Mimicking the biomechanics of such multilayer structures in tissue engineering requires multilayer scaffolds with selective layers having porosity and adequate elasticity.[8–10] Scaffolds are often created by processes employing organic solvents (e.g. solvent casting, freeze-drying, and electrospinning).[11–15] However, removal of the residual traces of organic solvent, which often are toxic, can become a hurdle for scaffolds intended for biomedical application. Therefore, the creation of scaffolds using nontoxic solvents as well as providing layered structure is still a major challenge.

An alternative approach for the creation of porous structures avoiding non-toxic

---

[1] Institute of Biomaterial Science and Berlin-Brandenburg Center for Regenerative Therapies, Helmholtz-Zentrum Geesthacht, Kantstraße 55 14513, Teltow, Germany

[2] Institute of Chemistry, University of Potsdam, 14469, Potsdam, Germany

[3] Tianjin University–Helmholtz-Zentrum Geesthacht, Joint Laboratory for Biomaterials and Regenerative Medicine
E-mail: andreas.lendlein@hzg.de

substances is the application of immiscible polymer blends with co-continuous morphology, in which one phase is subsequently extracted.[16,17] Co-continuous, also known as fully continuous phase morphology, can be obtained by immiscible binary blends of polymer A and polymer B, where the concentration of polymer A compared to polymer B is lower and it forms droplets dispersed in polymer B. Increasing the concentration of polymer A results in phase inversion, where polymer B forms droplets. Near the phase inversion point, both polymers A and B provide the fully continuous phase. An interconnected pore structure can be generated by extraction of one phase by a specific solvent for that phase.[18] To avoid any trace of toxic organic solvents, nontoxic solvents such as water can be used for the extraction.

The obtained pore sizes can be controlled by tailoring the binary morphology in the melt blending process. Such a binary morphology is in non-equilibrium state and is not stable during further processes such as injection molding. Stability of the binary morphology can be achieved by reduction of the interfacial area between the two phases, which minimizes the free energy of these systems due to coarsening phenomena, which can be obtained by quiescent annealing of the co-continuous blend in a short time period.[19–23] In addition, various parameters such as annealing temperature, annealing time, the physical state of the materials as well as compositions of the blends influence the morphology as well and result in different pore sizes upon subsequent leaching.[23,24]

Here, we explored whether injection molding could be used as a process to form a double layer porous structure and whether the particulate leaching technique could introduce pores in such bilayer system. In addition, we investigated how the overall elasticity of the double layer structure was influenced by the contribution of the elasticity of the individual layers. Furthermore, the tailoring of pore sizes using annealing treatment was examined. In this study, the melt blending of binary polymer mixtures of scaffold forming polyether urethane (PU) and polyvinyl alcohol (PVA) as a water-soluble particulate leaching material[25] was investigated as a model system. The resulting bilayer structures consisted of two layers with identical PU/PVA ratios, in which two PUs differing in hard segment content were used. Finally, porous bilayer structures were achieved using sequential injection molding followed by leaching in water. Pore morphology and mechanical properties of single and double layers were characterized. Furthermore, the contributions of the mechanical properties of single layers in bilayer constructs were explored in the compact and porous structures and the overall elasticity of compact and porous bilayer structures was compared with the predicted overall elasticity determined by rule of mixtures.

The elastic modulus of composite materials such as layered constructs can be predicted by employing a concept of rule of mixtures, which determines the upper bound (Equation 1) and lower bound (Equation 2) elastic modulus of layered structures, E_b is the elasticity of the bilayer structure, E_1 and E_2 denote the elasticity of the constructive layers, and f_1 is the volume fraction of one layer within the bilayer structure.[26–30]

$$E_b = f_1 E_1 + (1 - f_1) E_2 \tag{1}$$

$$\frac{1}{E_b} = \frac{f_1}{E_1} + \frac{1 - f_2}{E_2} \tag{2}$$

The morphology of blends in single layers was studied by employing quiescent annealing at two different temperatures and subsequent characterization of the obtained pore morphologies.

Experimental Part

Materials

The aliphatic polyether urethanes (PUs) Tecoflex® EG72D with $M_w = 64{,}000\ \mathrm{g \cdot mol^{-1}}$ and Tecoflex® 100A with $M_w = 57{,}000\ \mathrm{g \cdot mol^{-1}}$ were obtained from Noveon (Wilmington, MA, USA). Polyvinyl alcohol (PVA) of $M_w = 87{,}000\ \mathrm{g \cdot mol^{-1}}$ was purchased from Kurraray (Mowiflex® TC 251, Chiyoda, Tokyo, Japan). The materials were received as pellets and were used without any further purification.

^{1}H NMR Spectroscopy

^{1}H NMR spectroscopy was performed on a 500 MHz Avance spectrometer (Bruker, Karlsruhe, Germany) at 25 °C using tetramethylsilane as internal standard and deuterated chloroform as solvent. The weight content of the hard segment (H_{12}MDI/1,4-BD segment) of PUs was calculated by using the integrals of characteristic signals from the PUs according to the chemical structure (Figure 1), from which the repeating units of the PUs could be associated to the hard segment (H_{12}MDI/1,4-BD segment) or the soft segment (H_{12}MDI/PTMEG segment) as described in reference.[31]

Blending of PUs and PVA

The PUs as well as PVA were dried for four hours at 60 °C and blended for 10 min using a co-extrusion Minilab CTW5 (Thermo Electron GmbH, Karlsruhe, Germany) with a screw speed of 100 rpm and a processing temperature of 180 °C for Tecoflex® EG72D and 170 °C for Tecoflex® 100A.

Bilayer Formation

The double layer constructs were created by sequential injection molding with a HAAKE Minijet (Thermo Electron Corporation, Newington, NH, USA). A first layer was injected in a mold for test specimens of type DIN EN ISO 1BB (length = 20 mm, width = 2 mm, thickness = 1 mm). After cooling to the room temperature, the obtained polymer layer was placed in a mold of similar shape but of 2 mm thickness. The bilayer constructs were created by injecting the second layer on top of the first layer.

Creation of the Porous Bilayer Structure

PVA was leached out from the blends by immersing the double layer constructs in deionized water at 70 °C for 72 h. Finally, the obtained porous bilayer constructs were dried in a vacuum oven for 24 h at 50 °C. Compact bilayers as control samples were prepared without the addition of PVA and omitting the leaching process. Figure 2 illustrates the preparation process and provides the process parameters.

Morphological Analysis

The morphology of the porous single layer and bilayer constructs was analyzed by scanning electron microscopy (SEM). Cross sections of the samples were coated with a 2 nm conductive layer of Iridium and images were taken at 50 – 2000X, at 3 kV using a Zeiss Supra 40 VP (Zeiss, Jena, Germany). Several SEM images were taken for each porous layer. The sizes of at least 500–800 pores per layer were measured using ImageJ software (ImageJ 1.46 r, National Institutes of Health, Bethesda, Mary land, USA) from which the average pore size was calculated. Porosity was calculated using the following equation, where ρ_p and ρ were the apparent density of porous layer and compact layer, in which the apparent density was determined by measuring the dimensions and mass of the porous structures.[32]

Figure 1.

Chemical structure of PUs representing the repeating units, which comprises the hard and soft segment with different units (x, y) used as matrix in the bilayer constructs.

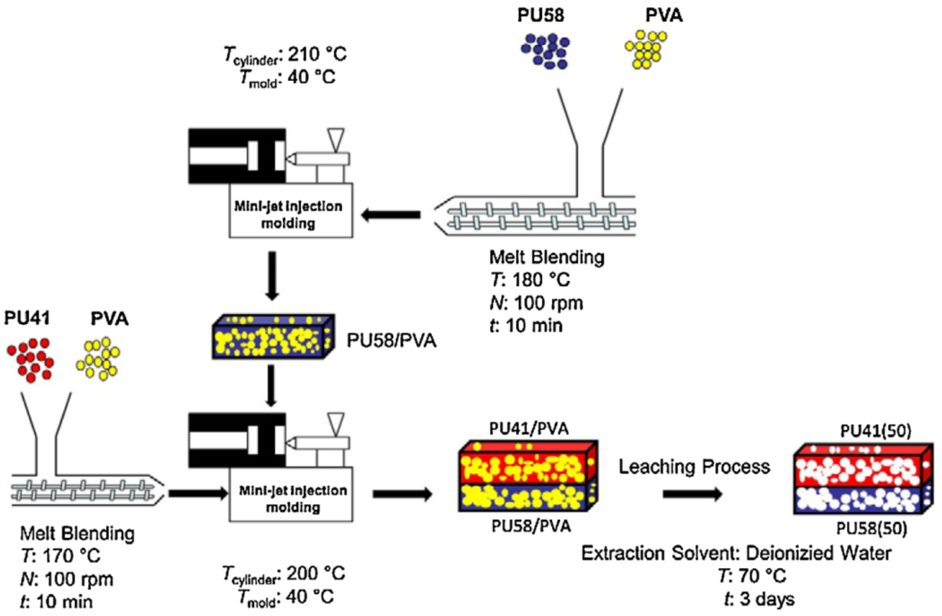

Figure 2.
Schematic representation of the melt blending, the sequential injection molding, and the leaching process for the formation of porous bilayer structures.

$$\text{Porosity} = \left(1 - \frac{\rho_P}{\rho}\right) \times 100 \qquad (3)$$

Mechanical Characterization

Compact single layer and bilayer constructs as well as porous single layer and bilayer constructs (DIN EN ISO 1BB specimen) were tested on a Z005 Zwick (Zwick GmbH, Ulm, Germany) with a strain rate of 5 mm $\cdot$ min^{-1} at 37 °C.

Annealing

Annealing treatment was conducted on obtained single layers in an oven for 30 min and subsequent quenching with liquid nitrogen to freeze the morphologies. 110 °C and 130 °C were selected as two different annealing temperatures.

Results and Discussion

The chemical composition of the two PUs was determined by ^{1}H NMR. The $H_{12}MDI$/1,4-BD hard segment contents were 58 and 41 wt% for Tecoflex® EG72D and for Tecoflex® 100A, respectively. The porous single and double layers were named as PUm(n), where m indicated the hard segment content in wt% and n denoted the amount of blended PVA in wt%. The porosity of 50 ± 5% for single layers as well as bilayers was calculated based on the apparent density. The analyses of the morphology of individual layers and bilayer constructs confirmed an interconnected porous structure (Figure 3). The image-based analysis revealed that the porous layer of PU58(50) had a pore size distribution ranging between 1 μm and 100 μm with an average size about 23 ± 10 μm and the pore size of porous layer of PU41(50) ranged between 1 μm and 100 μm with an average diameter of around 22 ± 12 μm.

The influence of the presence of pores on the mechanical properties of each layer was studied by tensile tests at 37 °C. Young's modulus (E) decreased from 110 ± 10 MPa to 50 ± 20 MPa for the PU58 layer and from 20 ± 3 MPa to 10 ± 4 MPa for the PU41 layer. The introduction of the pores also affected

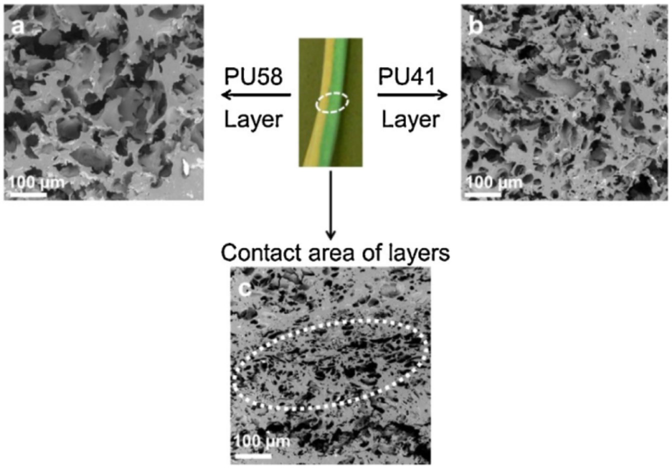

Figure 3.
SEM images of porous bilayer structure PU58(50)-PU41(50). a) Porous layer of PU58(50); b) Porous layer of PU41 (50); c) Contact area of the two layers.

the elongation at break (ε_B), which decreased from 390 ± 40% to 120 ± 50% for the PU58 layer and from 500 ± 20% to 130 ± 50% for the PU41 layer. The reduction of E and ε_B of both layers was correlated to the decrease of volume fraction of solid (density) of the material.[33–35] Furthermore, the contribution of each layer to the mechanical properties of bilayer constructs was studied by tensile tests. E of compact bilayers of PU41(0)-PU58(0) was 53 ± 3 MPa, where E of each individual layer was 20 ± 3 MPa for the PU41(0) layer and 110 ± 10 MPa for the PU58(0) layer. The porous bilayer constructs of PU58(50)-PU41(50) exhibited an E of 13 ± 3 MPa, where the E of each individual porous layer was 10 ± 4 MPa for the PU41(50) layer and 50 ± 20 MPa for the PU50(50) layer. These results were in agreement with the predicted overall elasticity using the rule of mixtures, where the upper and lower bound moduli were 53 MPa and 13 MPa for the compact PU41(0)-PU58(0) structure and 33 MPa and 16 MPa for the porous PU41 (50)-PU58(50) structure. On the other hand, the ε_B of compact bilayer of PU41 (0)-PU58(0) was 450 ± 40%, while the ε_B of a single compact layer were 390 ± 40% for PU58(0) and 500 ± 20% for PU41(0). In addition, the ε_B of porous bilayer of PU58(50)-PU41(50) was 70 ± 40%, while the ε_B of individual porous layers were 120 ± 50% for PU58(50) and 130 ± 50% for PU41(50). These results indicated that the formation of bilayer porous structures decreased slightly the overall deformation capability, which could be attributed to the distribution of pore sizes within each layer.

Annealing Studies on Pore Sizes

Pore sizes were tailored by employing an annealing treatment before the leaching process was conducted. Figure 4 and Table 1 indicate that the coarsening in PU matrices in co-continuous phases occurred upon application of the annealing treatment at two different temperatures resulting in smaller pore sizes. Nevertheless, the porosity of singles layers stayed constant, which was attributed to the constant weight content of PVA in each layer. Alternatively to the method described here, the pore sizes can be controlled by tailoring the obtained binary morphology in the melt blending process. Not only component properties such as viscosity and elasticity ratio of two components influence the obtained morphology but also the process parameters such as

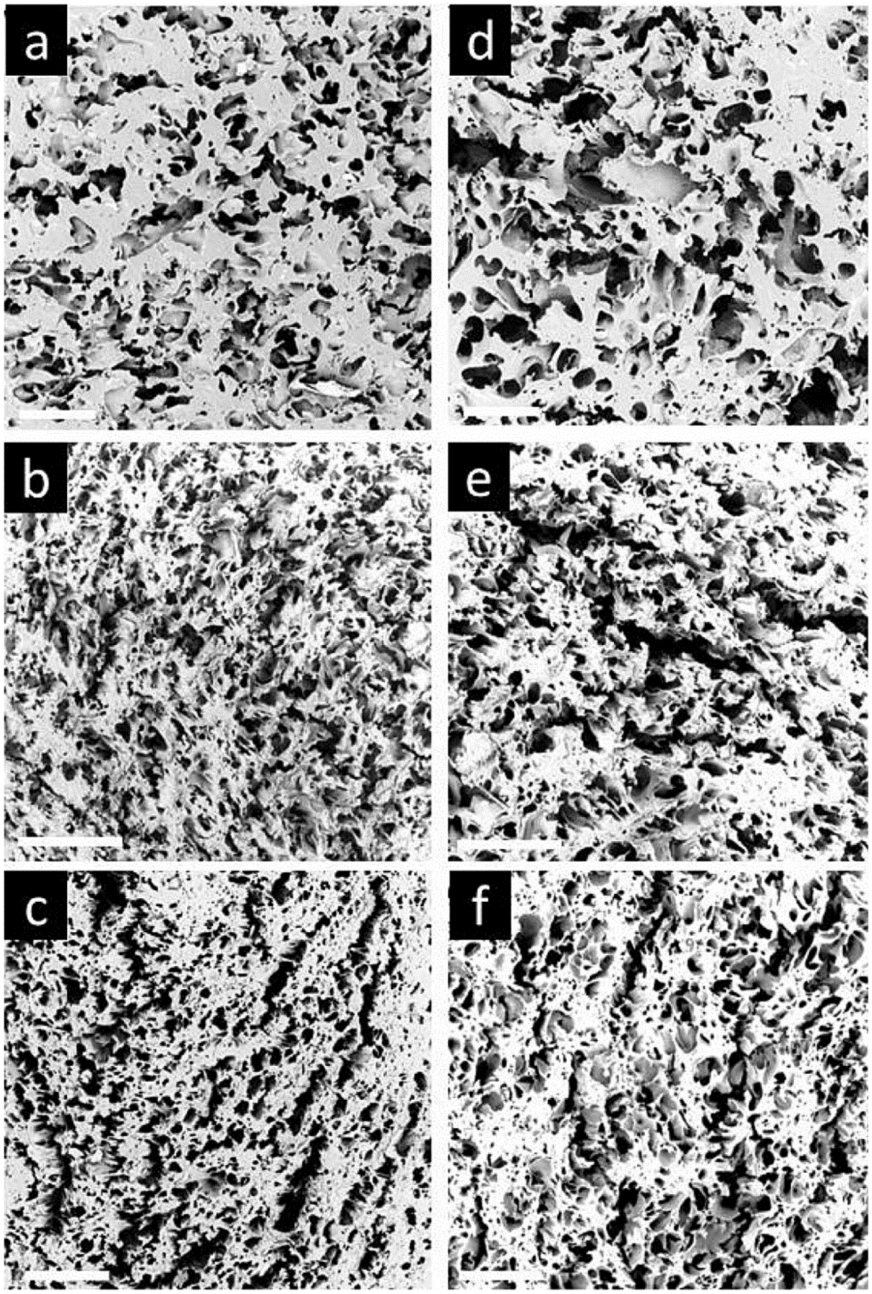

Figure 4.
SEM images of porous layer of PU58 (50) a) Non-annealed sample; b) Annealed at 110 °C; c) Annealed at 130 °C and SEM images of porous layer of PU41(50) d) Non-annealed sample; e) Annealed at 110 °C; f) Annealed at 130 °C. Scale bar is 100 μm.

applied shear rate by controlling the screw speeds (N), and the blending time (t) affect the binary morphology.[36–38] In addition, choosing other blending methods such as mechanical mixing, dissolution in co-solvent, and fine powder mixing could result into different morphology and alter the pore sizes.

In summary, mechanical properties of layered structures can be adjusted and

Table 1.
Comparison of characterization of porous layers before and after annealing treatment.

Layer ID	Pore Diameter		
	Mean [µm]	SD [µm]	Porosity [%]
PU58(50)			
Non-annealed	23.2	10.4	50 ± 5
Annealed at 110 °C	20.9	9.9	50 ± 10
Annealed at 130 °C	15.6	8.8	50 ± 5
PU41(50)			
Non-annealed	22.2	12.6	50 ± 5
Annealed at 110 °C	20.7	10.1	50 ± 5
Annealed at 130 °C	17.8	9.6	50 ± 10

predicted by choice of appropriate polymers and the porosity introduced. In addition, the pore sizes could be tailored by variation of annealing temperature.

Conclusion

Porous bilayer scaffolds could be obtained by melt blending of PU/PVA, followed by sequential injection molding and leaching the PVA phase in deionized water. In this way the usage of potentially toxic organic solvents was avoided. A porosity of 50 ± 5% for single and bilayer constructs were determined and interconnected pores for single and bilayer structures was confirmed by means of SEM. The mechanical properties of single and bilayer constructs of compact as well as porous structures were investigated by tensile tests at 37 °C, which proved that the overall elasticity of the compact and porous bilayer structures were consistent with the values obtained by the rule of mixtures. In addition, pores sizes were tailored without changes in the composition of blends by controlling the morphology of blends using an annealing treatment before leaching process. These bilayer constructs could serve as model systems for determining structure-property relationships considering porosity, pore sizes, and mechanical properties of the individual layers enabling a knowledge-based design of layered scaffold.

[1] M. Horst, S. Madduri, V. Milleret, T. Sulser, R. Gobet, D. Eberli, *Biomaterials* **2013**, *34*, 1537.

[2] D. W. Park, S.-H. Ye, H. B. Jiang, D. Dutta, K. Nonaka, W. R. Wagner, K. Kim, *Biomaterials* **2014**,

[3] F. Ajalloueian, M. L. Lim, G. Lemon, J. C. Haag, Y. Gustafsson, S. Sjöqvist, A. Beltrán-Rodríguez, C. Del Gaudio, S. Baiguera, A. Bianco, P. Jungebluth, P. Macchiarini, *Biomaterials* **2014**, *35*, 5307.

[4] H. Lee, H. Hwang, Y. Kim, H. Jeon, G. Kim, *Chem. Eng. J.* **2014**, *250*, 399.

[5] K. Whang, K. E. Healy, D. R. Elenz, E. K. Nam, D. C. Tsai, C. H. Thomas, G. W. Nuber, F. H. Glorieux, R. Travers, S. M. Sprague, *Tissue Eng.* **1999**, *5*, 35.

[6] H. Tai, M. L. Mather, D. Howard, W. Wang, L. J. White, J. A. Crowe, S. P. Morgan, A. Chandra, D. J. Williams, S. M. Howdle, K. M. Shakesheff, *Eur. Cell. Mater.* **2007**, *14*, 64.

[7] M. C. Wake, C. W. Patrick, Jr., A. G. Mikos, *Cell Transplant* **1994**, *3*, 339.

[8] B. A. Harley, A. K. Lynn, Z. Wissner-Gross, W. Bonfield, I. V. Yannas, L. J. Gibson, *J. Biomed. Mater. Res. A* **2010**, *92*, 1078.

[9] G. A. Holzapfel, G. Sommer, C. T. Gasser, P. Regitnig, *Am. J. Physiol. Heart Circ. Physiol.* **2005**, *289*, H2048.

[10] M. D. Humzah, R. W. Soames, *Anat. Rec.* **1988**, *220*, 337.

[11] T. Weigel, G. Schinkel, A. Lendlein, *Expert. Rev. Med. Devices* **2006**, *3*, 835.

[12] K. Hassan, S. Kim, I. Park, S. Lee, S. Kim, Y. Jung, S.-H. Kim, S. Kim, *Macromol. Res.* **2011**, *19*, 122.

[13] J. S. Mao, L. G. Zhao, Y. J. Yin, K. D. Yao, *Biomaterials* **2003**, *24*, 1067.

[14] A. G. Mikos, G. Sarakinos, S. M. Leite, J. P. Vacant, R. Langer, *Biomaterials* **1993**, *14*, 323.

[15] D. M. Yunos, Z. Ahmad, V. Salih, A. R. Boccaccini, *J. Biomater. Appl.* **2013**, *27*, 537.

[16] P. Sarazin, X. Roy, B. D. Favis, *Biomaterials* **2004**, *25*, 5965.

[17] N. R. Washburn, C. G. Simon, A. Tona, H. M. Elgendy, A. Karim, E. J. Amis, *J. Biomed. Mater. Res.* **2002**, *60*, 20.

[18] V. Guarino, A. Guaccio, L. Ambrosio, *J. Appl. Biomater. Funct. Mater.* **2011**, *9*, 34.

[19] R. C. Willemse, E. J. J. Ramaker, J. Van Dam, A. P. De Boer, *Polym. Eng. Sci.* **1999**, *39*, 1717.

[20] Z. Yuan, B. D. Favis, *AIChE J.* **2005**, *51*, 271.

[21] X.-Q. Liu, R.-H. Li, R.-Y. Bao, W.-R. Jiang, W. Yang, B.-H. Xie, M.-B. Yang, *Soft Matter* **2014**, *10*, 3587.

[22] Z. Yuan, B. D. Favis, *Biomaterials* **2004**, *25*, 2161.

[23] G. S. Y. Yeh, R. Hosemann, J. Loboda-Čačković, H. Čačković, *Polymer* **1976**, *17*, 309.

[24] A. T. Lorenzo, M. L. Arnal, J. J. Sánchez, A. J. Müller, *J. Polym. Sci. Part B: Polym. Phys.* **2006**, *44*, 1738.

[25] A. Kramschuster, L. S. Turng, *J. Biomed. Mater. Res. B* **2010**, *92B*, 366.

[26] R. K. Cullen, M. M. Singh, J. Summerscales, *J. Comp.* **2013**, 416501.

[27] Y. Fukui, K. Takashima, C. B. Ponton, *J. Mater. Sci.* **1994**, *29*, 2281.
[28] C. P. Wong, R. S. Bollampally, *J. Appl. Polym. Sci.* **1999**, *74*, 3396.
[29] P. J. Roe, M. P. Ansell, *J. Mater. Sci.* **1985**, *20*, 4015.
[30] P. J. Herrera-Franco, A. Valadez-González, *Composites Part A* **2004**, *35*, 339.
[31] J. Cui, K. Kratz, M. Heuchel, B. Hiebl, A. Lendlein, *Polym. Advan. Technol.* **2011**, *22*, 180.
[32] S. Ghosh, J. C. Viana, R. L. Reis, J. F. Mano, *Acta Biomaterialia* **2008**, *4*, 887.
[33] L. J. Gibson, *J. Biomech.* **2005**, *38*, 377.
[34] M. F. Ashby, *Philos. Trans. R. Soc. London, Ser. A* **2006**, *364*, 15.
[35] L. J. Gibson, M. F. Ashby, *Proc. R. Soc. Lond., Ser. A: Biol. Sci.* **1982**, *382*, 43.
[36] P. Sarazin, B. D. Favis, *Biomacromolecules* **2003**, *4*, 1669.
[37] S. Steinmann, W. Gronski, C. Friedrich, *Polymer* **2001**, *42*, 6619.
[38] S. H. Oh, S. G. Kang, E. S. Kim, S. H. Cho, J. H. Lee, *Biomaterials* **2003**, *24*, 4011.

Manufacturing and Characterization of Controlled Foaming of Single Layers in Bilayer Constructs Differing in Pore Morphology

Mersa Saatchi,[1,2,3] *Marc Behl,*[1,3] *Andreas Lendlein**[1,2,3]

Summary: Bilayer porous constructs from degradable polymers are considered as scaffold materials with beneficial elastic properties for cell culture application in tissue engineering. Here, we explored whether such bilayer constructs, in which only one layer was porous while the other layer enhanced the compressive mechanical properties, could be created by specific foaming of one layer with supercritical carbon dioxide ($scCO_2$). The bilayer constructs of a poly(*L*-lactide) (PLLA) and a poly(ε-caprolactone) (PCL) layer were prepared by sequential injection molding and subsequent specific foaming with $scCO_2$. Foaming conditions of $T = 45\,^\circ C$ and $P = 100$ bar resulted in the formation of a porous PCL layer and a non-porous PLLA layer. When the time intervals of the foaming process were increased the pore size was increased and the shape of the pores was changed from a circular to an unidirectional lamellar shape, which reduced the compressive elastic modulus of the porous PCL layer. Furthermore, the foaming process increased the adhesion force between the PLLA and PCL layers, which was attributed to a higher degree of diffusion of molten PCL into the PLLA layer. In summary, it was demonstrated that $scCO_2$ foaming is a suitable method for the creation of layered scaffolds with only one foamed layer, in which the compressive elastic modulus and pore morphology of single porous layers can be controlled by the time interval of $scCO_2$ process.

Keywords: layered structure; poly(ε-caprolactone); poly(L-lactide); scaffold; supercritical carbon dioxide

Introduction

Poly(*L*-lactide) (PLLA) and poly(ε-caprolactone) (PCL) are biodegradable materials, which have a high application potential for polymeric scaffolds.[1–3] However, the preparation of scaffolds providing high porosity and mechanical strength compared to the surrounding tissue is still a challenge.[4,5] The compressive strength and the elastic modulus, in addition to the scaffolds stiffness could be increased by reinforcing elements, such as bioactive ceramics, fibers as well as layers to the scaffold matrix.[6,7,8,9] The incorporation of a compact PLLA layer in a PLLA scaffold, which was prepared by solid liquid phase separation and freeze-drying enhanced both compressive elastic modulus and compressive strength.[10,11]

Motivated by the potential toxicity of traces of the organic solvent, which might be left in a process employing organic solvent, we explored whether such bilayer constructs could be prepared in an organic solvent free process. $ScCO_2$ foaming is a non-toxic, low-cost process to introduce pores into solid polymers and consists of

---

[1] Institute of Biomaterial Science and Berlin-Brandenburg Center for Regenerative Therapies, Helmholtz-Zentrum Geesthacht, Kantstraße 55, 14513 Teltow, Germany
E-mail: andreas.lendlein@hzg.de

[2] Institute of Chemistry, University of Potsdam, 14469 Potsdam, Germany

[3] Tianjin University–Helmholtz-Zentrum Geesthacht, Joint Laboratory for Biomaterials and Regenerative Medicine

four steps: a) polymer plasticization due to $scCO_2$ diffusion into polymer matrix at high pressure, b) nucleation of bubbles and generation of pores upon depressurization, c) nucleation growth due to gas diffusion from the surrounding polymer, and d) fixation of pores as a result of increased glass transition temperature (T_g). [12 14]

In this way porous structure from semi-crystalline PCL can be prepared in a $scCO_2$ foaming process at a temperature around 40 °C.[12,14] In contrast, semi-crystalline PLLA features a low crystallization rate, which results in an amorphous, glassy state as injection molding has a rapid cooling rate. However, subsequent treatment with $scCO_2$ in the foaming process induces crystallization of lactide polymer chain segments, which hinder the diffusion of $scCO_2$ into the polymer matrix causing a non-porous structure.[15 17]

Here, it was explored whether bilayer constructs could be prepared, in which only the PCL layer is foamed by taking advantage of the different crystallization kinetics. In this way, the usage of potentially toxic organic solvents for the creation of scaffolds can be avoided. Sequential injection molding of PCL and PLLA was applied to create two layer constructs, on which the foaming by $scCO_2$ was explored. The foaming process was characterized by determining the morphology of the pores in the foamed layer and the mechanical properties of the layers. The non-porous layer was characterized by tensile tests and wide angle X-ray scattering. In addition, influence of the foaming condition was studied by determining the adhesion force between the two layers.

Experimental Part

Materials: PLLA (*meso*-lactide content 8mol%, $M_w = 116{,}000\ g \cdot mol^{-1}$, $T_g = 58\,°C$, $T_m = 160\,°C$) was purchased from NatureWorks (Ingeo^{TM} 3052D, Nebraska, USA). PCL ($M_w = 123{,}000\ g \cdot mol^{-1}$, $T_g = -60\,°C$, $T_m = 60\,°C$) was obtained from Perstorp (CAPA® 6800, Cheshire, UK). The materials were received as pellets and were used without any further purification.

Bilayer formation: The double layer constructs composed of PLLA and PCL layers were manufactured by sequential injection molding with a HAAKE Minijet machine (Thermo Electron Corporation, Newington, NH, USA). At first, a PCL layer was injected in a mold of test specimens type DIN EN ISO 1BB (length = 20 mm, width = 2 mm, thickness = 1 mm). After cooling, the prepared PCL layer was placed in a mold of similar shape but doubled thickness (length = 20 mm, width = 2 mm, thickness = 2 mm). PLLA was injected on the top of the PCL layer yielding a bilayer construct.

Controlled foaming of PCL layer: Bilayer constructs, in which only the PCL layer was foamed, were obtained by placing the double layer constructs in a $scCO_2$ autoclave as described in reference.[18] The constructs were placed in glass vials as sample vessels in the autoclave. Two different time intervals (1 h and 4 h) were applied, whereby pressure and temperature were kept constant (100 bar, 45 °C). Figure 1 illustrates the formation process and provides process parameters.

Characterization methods: The weight average molecular weight (M_w) of PLLA and PCL were analyzed by gel permeation chromatography (GPC). Multi detector GPC measurements were performed using chloroform at 35 °C as eluent with a flow rate of $1\ mL \cdot min^{-1}$ and 0.2 wt% toluene as internal standard to monitor the flow. The GPC system consisted of a precolumn, two 300 mm x 8.0 mm linear M columns (Polymer Standards Service GmbH, Mainz, Germany, PSS), an isocratic pump 2080, and an automatic injector AS 2050 (both Jasco, Tokyo, Japan). Two detectors were used: a RI detector Shodex RI-101 (Showa Denko, Japan) and the dual detector T60A (Viscotek Corp., USA), which were combined by a split. Molecular weights were determined by universal calibration applying polystyrene standards with M_n between $580\ g \cdot mol^{-1}$ and $975\,000\ g \cdot mol^{-1}$ (PSS) using the SEC software Unity (PSS). M_w

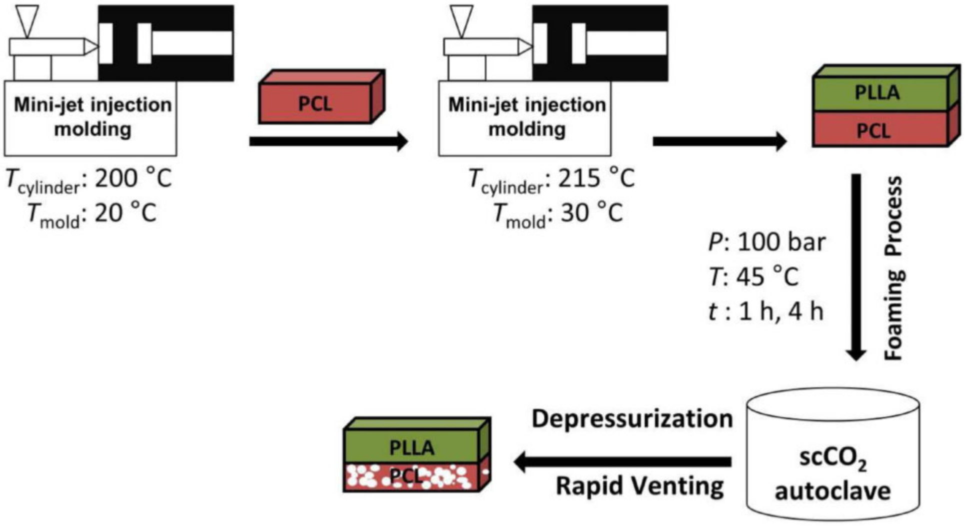

Figure 1.
Schematic presentation of the sequential injection molding for the formation of bilayer constructs and the subsequent controlled specific foaming process.

of the PLLA and the PCL layers were determined after each process step.

The thermal properties of PLLA and PCL after each process step were characterized by differential scanning calorimetry (DSC) (Netzsch DSC 204 Phoenix, Netzsch, Selb, Germany) from -10 to 200 °C with a heating rate of 10 $K \cdot min^{-1}$.

Morphological analysis of the double layer constructs were carried out by scanning electron microscopy (SEM). Cross sections of the samples were coated by a 4 nm conductive layer and images were taken at 50 - 2000X, 3 kV using Zeiss Supra 40 VP (Zeiss, Jena, Germany). The porosity and pore size were determined by X-ray computed microtomography (μ-CT, Procon X-ray GmbH, Garbsen, Germany). The single porous layer was fixed on a rotary stage and scanned inside the μ-CT apparatus using a voltage of 40 kV and a current of 0.19 mA.

Wide angle X-ray scattering (WAXS) measurements were performed at room temperature on a Bruker D8 Discover (Bruker AXS, Karlsruhe, Germany) to investigate the formation of crystalline domains in PLLA layers. The X-ray generator was operated at 40 kV and 40 mA on a copper-anode. The collimator was adjusted to 0.8 mm beam size. The two-dimensional detector (Hi-Star) was operated in 1024 × 1024 pixel mode. The distance sample-detector was 150 mm and the wavelength $\lambda = 0.15418$ nm. The detector was positioned at an angular positions $2\theta = 25°$ in order to cover an angular range from $2\theta = 7.2°$ to 43.5°. Exposure time was 300 s per scattering pattern.

Compression tests of single PCL porous layers were carried out on a Z005 Zwick (Zwick GmbH, Ulm, Germany) at room temperature. The porous structures were compressed up to 50% strain to measure the compressive elastic modulus followed by the unloading of the compressive stress to determine the elastic recovery of the pores.

Single PLLA layers were tested under tensile condition on a Z005 Zwick (Zwick GmbH, Ulm, Germany) with a strain rate of 5 $mm \cdot min^{-1}$ at room temperature.

Adhesion force between the two layers was examined with the Z005 Zwick tensile tester (Zwick GmbH, Ulm, Germany) by a T-Peel test [19] with a peeling rate of 20 $mm \cdot min^{-1}$ at room temperature.

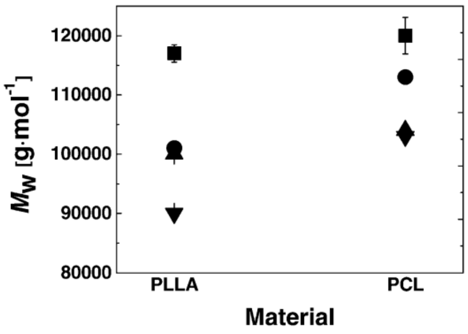

Figure 2.
Effect of different processing methods on the M_w of the polymer in each layer. M_w: ■ starting material; ● after injection molding; ▲ after foaming process for 1 h; ▼ after foaming process for 4 h.

Results and Discussion

The double layer constructs were named as BL(X), single layers of PLLA and PCL were defined as LPLA(X) and LPCL(X) and in addition, X indicated the time interval of foaming process in hours. M_w and thermal properties of PLLA and PCL layer were compared after each process step to the M_w and thermal properties of the starting material for exploring the degradation caused by heat and shear forces during the process. When the time intervals of the foaming process were increased from 1 h to 4 h the M_w of PLLA was decreased by 1000 g·mol^{-1} while the M_w of the PCL layer was not significantly influenced (Figure 2). Additionally, exposure to the scCO$_2$ autoclave did not influence the thermal properties of PLA and PCL layers (Figure 3).

Furthermore, when the time interval of the foaming process in the autoclave was extended from 1 h to 4 h, the shape of the pores determined by SEM was altered from a circular shape to an unidirectional lamellar shape (Figure 4). In addition, the average size of the pores increased from 190 ± 90 μm to 220 ± 90 μm while the porosity remained constant at 80 ± 5%. The scCO$_2$ foaming process induced crystalline domains in the PLLA layer from 0% (before scCO$_2$ process) to 50 ± 10% (after 1 h) and 33 ± 5% (after 4 h), which were further explored by WAXS measurements (Figure 5a). The lateral crystal size of the induced crystalline domains was determined as 8 ± 1 nm (after 1 h) and 16 ± 1 nm (after 4 h). Injection molding of PLLA prepared with a rapid cooling rate led to the formation of an amorphous solid. The exposure to high pressure during the scCO$_2$ foaming process induced crystalline domains, which was attributed to a reduction of T_g and rearrangement of polymer chains. These effects stabilized the amorphous domains and resulted in the formation of a non-porous PLLA layer. The Young's modulus of non-porous PLLA layers decreased from 1700 ± 100 MPa (before scCO$_2$ process) to 1600 ± 100 MPa

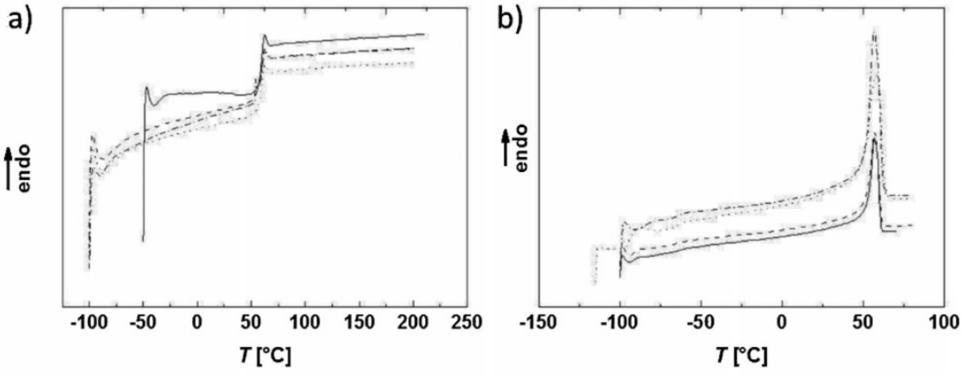

Figure 3.
Effect of the different processing methods on the thermal properties of the polymer in each layer. DSC thermograms of a) – starting material of PLA; - ···· PLA after injection molding; ···· LPLA(1); --- LPLA(4), b) ···· starting material of PCL;-····-PCL after injection molding; – LPCL(1); --- LPCL(4) on the second heating cycle.

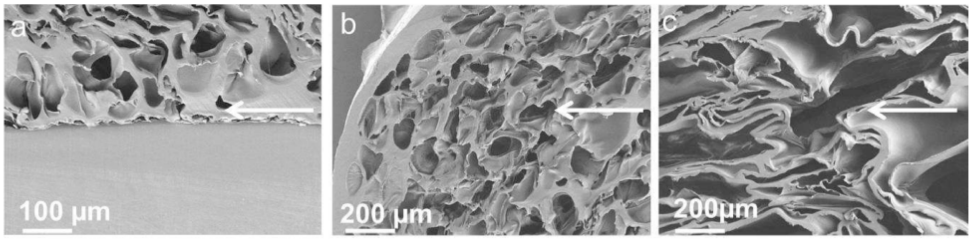

Figure 4.
SEM images of the double layer constructs. a) Double layer construct of BL(1), in which the PCL layer was foamed and the PLLA layer remained compact. b) Porous layer LPCL(1) with circular shaped pores. c) Porous layer of LPCL(4) with pores providing an unidirectional lamellar shape. Arrows indicate the direction of foaming.

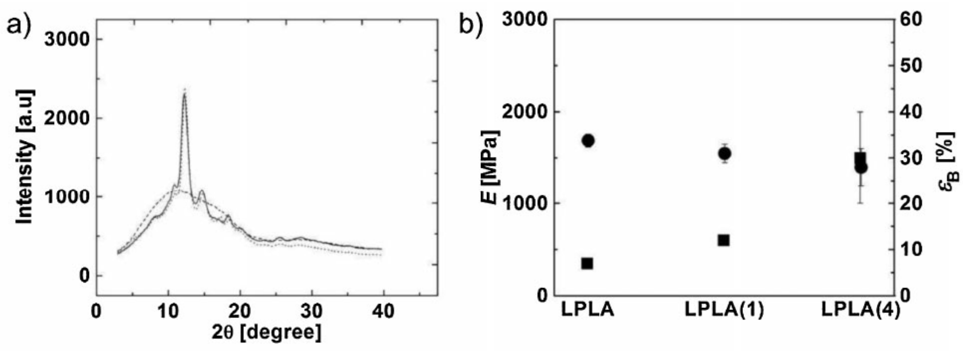

Figure 5.
a) WAXS analysis of PLLA before and after foaming process. -- LPLA; — LPLA(1); ···· LPLA(4). b) Tensile tests of PLLA before and after foaming process. ● E; ■ ε_B.

(after 1 h) and 1400 ± 100 MPa (after 4 h) as determined by tensile tests (Figure 5b). On the other hand, the elongation at break (ε_b) of non-porous PLLA layers increased from 7 ± 1% (before scCO$_2$ process) to 12 ± 1% (after 1 h) and 30 ± 10% (after 4 h). These results can be explained by the formation of crystalline domains and a correspondingly increased lateral size of the crystals during the foaming process (Table 1).

The mechanical properties of the PCL porous layer were analyzed by compression tests (Figure 6a). LPCL(1) exhibited a compressive elastic modulus (E_{comp}) of 2300 ± 500 kPa and an elastic recovery of 45 ± 3%. However, for LPCL(4) E_{comp} and elastic recovery were reduced to 700 ± 100 kPa and 25 ± 4%, respectively. When the time intervals of the foaming process was extended from 1 h to 4 h two differently shaped porous structures in the porous layers were obtained, which highly affected E_{comp} and elastic recovery. A compression up to 50% caused the bending of the circular pore walls. However, the deformation of the unidirectional lamellar pores led

Table 1.
Characterization of the PLLA layer before and after exposure in the scCO$_2$ autoclave.

Layer ID	DOC$^{a,b)}$ [%]	Lateral crystal size$^{b)}$ [nm]	$E^{c)}$ [MPa]	$\varepsilon_b{}^{d)}$ [%]
LPLA	0	0	1700 ± 100	7 ± 1
LPLA(1)	50 ± 10	8 ± 1	1600 ± 100	12 ± 1
LPLA(4)	33 ± 5	16 ± 1	1400 ± 100	30 ± 10

a) Degree of crystallinity; b) Determined by WAXS; c) Young's modulus determined by tensile tests at room temperature; d) Elongation at break determined by tensile tests at room temperature.

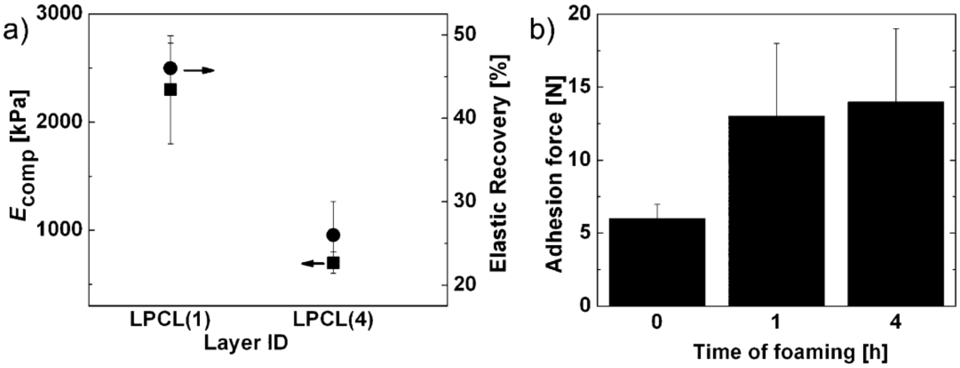

Figure 6.
a) Compression tests of the PCL porous layers ■ E_{comp}; ● Elastic recovery; b) T-Peel test of the bilayer constructs.

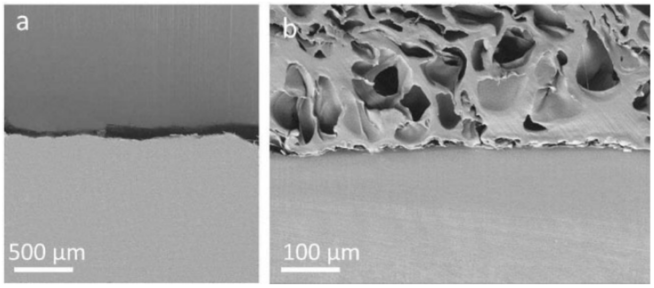

Figure 7.
SEM images of the bilayer construct interphase a) before and b) after applying $scCO_2$ conditions resulting in the foaming of the PCL layer.

to localized failure of the wall structure, which resulted in a lower E_{comp} and the elastic recovery.[20] The adhesion force between the PCL and PLLA layers was studied by T-Peel tests. Here, the adhesion force between the layers increased from 6 ± 1 N (before the foaming process) to 13 ± 4 N after the foaming process (Figure 6b). This can be attributed to a higher degree of diffusion of PCL into the interphase (on the micro level) of the bilayer constructs, which was confirmed by comparing SEM images of the bilayer constructs interphase before and after the foaming process (Figure 7).

Conclusion

Bilayer scaffolds could be obtained in a process without any organic solvent by controlled foaming of one layer of the bilayer constructs by rapid depressurization of $scCO_2$. In this way usage of potentially toxic solvents was avoided. When the time interval of the foaming process was increased the shape of the pores in the single porous layer could be tailored from circular pores to unidirectional lamellar pores, which caused the decrease of the compressive elastic modulus from 2300 ± 500 kPa to 700 ± 100 kPa. On the other hand, the $scCO_2$ process induced crystalline domains (50%) in the non-porous layer, which increased the ε_b from 7 ± 1 to 30 ± 10%. In addition, the adhesion between both layers was increased from 6 ± 1 N to 13 ± 4 N during the foaming process. In this way the controlled foaming of one layer of the bilayer constructs might enable new reinforced scaffolds in tissue engineering.

[1] W. Guobao, X. M. Peter, *Biomaterials.* **2004**, *25*, 4749.

[2] L. Xiaoming, F. Qingling, C. Fuzhai, *Mater. Sci. Eng. C.* **2006**, *26*, 716.

[3] Y. Kang, G. Yin, Q. Yuan, Y. Yao, Z. Huang, X. Liao, B. Yang, L. Liao, H. Wang, *Eur. Polym. J.* **2008**, *43*, 2029.

[4] T. Weigel, G. Schinkel, A. Lendlein, *Expert Rev. Med. Devices.* **2006**, *6*, 835.

[5] L. J. Gibson, M. F. Ashby, G. N. Karam, U. Wegst, H. R. Shercliff, *Proc. Math. Phys. Eng.* **1995**, *450*, 141.

[6] G. Georgiou, L. Mathieu, D. P. Pioletti, P. Bourban, J. E. Månson, J. C. Knowles, S. N. Nazhat, *J. Biomed. Mater. Res. Part B Appl. Biomater.* **2006**, *80*, 322.

[7] S. D. Mccullen, C. M. Haslauera, E. G. Loboa, *J. Mater. Chem.* **2010**, *20*, 877.

[8] Y. Kang, A. Scully, D. Young, S. Kim, H. Tsao, M. Sen, Y. Yang, *Europ. Polym. J.* **2011**, *47*, 1569.

[9] J.-E. Park, M. Todo, *J. Mater. Sci.* **2010**, *45*, 3966.

[10] J. E. Park, M. Todo, *Adv. Mater.* **2010**, *12*, 3303.

[11] J.-E. Park, M. Todo, *J. Mater. Sci. Mater. Med.* **2011**, *22*, 1171.

[12] A. Barry, M. Silva, V. Popov, M. Shakesheff, M. Howdle, *Phiosl. Trans. R. Soc. A.* **2006**, *364*, 249.

[13] H. Haugen, J. Will, W. Fuchs, E. Wintermantel, *J. Biomed. Mater. Res. Part B Appl. Biomater.* **2006**, *77*, 65.

[14] M. Jenkins, *Europ. Polym. J.* **2006**, *44*, 3145.

[15] T. Tabi, E. Sajo, *Express Poly. Lett.* **2010**, *4*, 659.

[16] B. Drumright, P. Gruber, D. Henton, *Adv. Mater.* **2002**, *48674*, 1841.

[17] D. Garlotta, *J. Polym. Environ.* **2002**, *9*, 63.

[18] K. Luetzow, F. Klein, T. Weigel, R. Apostel, A. Weiss, Andreas. Lendlein, *J. Biomech.* **2007**, *40*, S80.

[19] M. Mantel, F. Descaves, *J. Adhes. Sci. Technol.* **1991**, *6*, 357.

[20] M. Todo, H. Kuraoka, J. Kim, J. Taki, M. Ohshima, *J. Mater. Sci.* **2008**, *43*, 5644.

A General Approach Toward Multi-Pattern Memory Effect via Reversible Bidirectional Shape-Memory Substrates

Mersa Saatchi, Ulrich Nöchel, Marc Behl, and Andreas Lendlein

Institute of Active Polymers and Berlin-Brandenburg Center for Regenerative Therapies,
Helmholtz-Zentrum Hereon GmbH, Kantstraße 55, 14513 Teltow, Germany

Keywords: wrinkles, reversible bidirectional shape-memory polymers, thin gold film, bilayer structure

Abstract:

We demonstrate a simple approach to achieve reversible uniaxial wrinkles in a bilayer structure utilizing a substrate showing a reversible bidirectional shape-memory effect (rbSME), in which the formed wrinkles can be tuned by variation of separation temperature (T_{sep}). Furthermore, reversible multi-patterns (RMP) (i.e. complex and parallel wrinkles) can be formed by applying the concept of reversible uniaxial wrinkles on a pre-patterned surface. This was achieved by conducting a sequential biaxial (SEQB) stretching (programming) on a substrate having a broad melting temperature transition, which led to the formation of permanent wrinkles obtained by the first recovery of a triple shape-memory effect and temporary wrinkles caused by the rbSME. In this way, the application spectrum of rbSME can be extended to tunable material surfaces that are relevant in applications such as photonics, electronics, and aerodynamics.

Introduction:

Next generations of high-tech will demand intelligent materials with the ability to tune reversible surface morphology on the micro/nano scale in a controlled procedure.[107] Such a feature could be desirable for various applications such as micro optics[68], novel electronic devices[108], diffraction grating, pressure sensors, substrates for contact cue guidance of cell growth,[109] channels with microstructures walls for microfluidic devices[110], or functional coatings.[48]

Generally, wrinkling is a result of a physical mechanism in a bilayer construct consisting of a thin stiff film and a thick compliant substrate (Figure 1A)[50], generated by compressive strain either by employing thermal expansion mismatch, externally applied compressive force or differential swelling/shrinkage of the two layers.[107] Wrinkles arise from competition between the elastic bending energy of a stiff thin film and an elastic energy of deformation of the soft substrate, which the thin film is supported on.[111] The thin layer in the bilayer structure was created by solidifying the top-most part of the substrate (mostly used poly(dimethylsiloxane))[112] by applying a physical treatment such as oxygen plasma exposure and UV-ozone (UVO) treatment[53] as well as by deposition of a thin layer of metals such as gold, silver, and aluminum upon elastomeric[113] or shape-memory polymer (SMP) substrates.[54,114] The parametric studies showed that in the studies cases the wrinkle dimensions (wavelength (λ) and amplitude (A)) are controllable by the thickness of the metal thin film (h), the time of exposure to the oxygen plasma treatment, as well as the pre-strain applied before deposition of the metal layer or the oxygen plasma and UVO treatment.[115]

Different types of wrinkles have been generated ranging from homogenous parallel wrinkles (PLW) induced by uniaxial compressive strain to complex structure wrinkles such as square checkerboard, hexagonal, triangular, and herringbone patterns, which resulted from applying biaxial compressive strain to the substrate of the bilayer structure.[54,116,117] Nevertheless, to our knowledge, all research works reported the empowering of one-way SMP as a substrate led to the one-way wrinkling pattern generated upon heating above the switching temperature of substrate and remained on surface after cooling due to the erasing of temperature-memory effect (TME) of substrate.

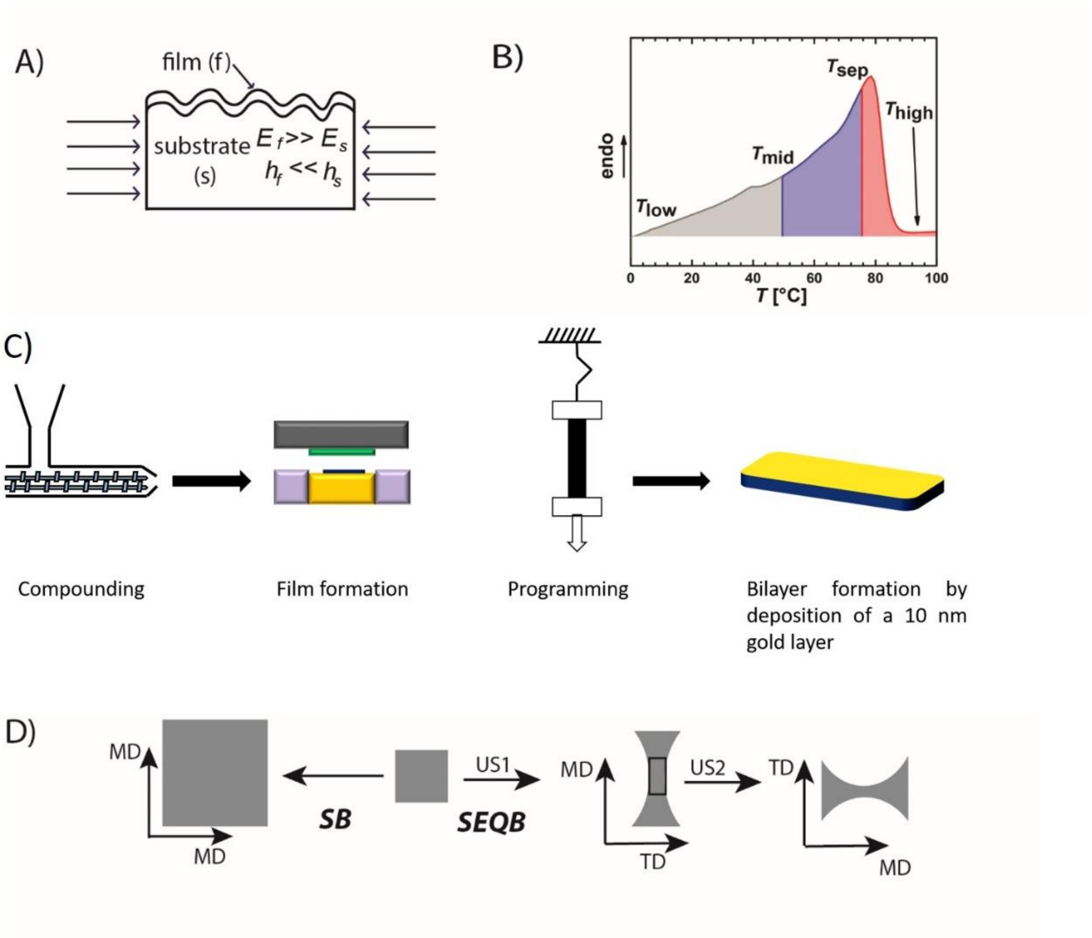

Figure 1. A) Scheme presenting the obtained wrinkles on a thin film on top of a thick compliant substrate in a bilayer structure; B) A broad melting temperature (ΔT_m) range required for rbSME and TSME, and the relevant temperatures; C) Schematic illustration of the fabrication process of the bilayer structure showing the preparation of the substrate and the programming step followed by deposition of a 10 nm gold layer; D) Two different biaxial programming modes applied on the substrates. SB: simultaneous biaxial stretching, where deformations were applied at X and Y direction simultaneously at T_{prog} = 100 °C and SEQB: sequential biaxial stretching at two different temperatures. The substrate was stretched at T_{prog} = 100 °C by a first uniaxial stretching (US1). The second uniaxial stretching (US2) consisted of applying a stretching perpendicularly to the first stretching direction at T_{sep} (MD: machine direction; TD: transverse direction).

Inspired by the anisotropic surface properties found in nature such as self-cleaning lotus effect[43] and shark skin effect[45] originated via periodic micro/nano size surface patterns, we hypothesized that by using a substrate exhibiting a reversible bidirectional shape-memory effect (rbSME)[75,76] coated with a thin gold layer, reversible parallel wrinkling (PLW) might be achieved (wrinkles on/off), whereby the wrinkles' dimensions could be *in-situ* tuned by adjusting a specific separation temperature (T_{sep}) in a broad melting temperature range of substrate.[106]

The rbSME was observed in semi-crystalline co-polymer networks having a broad melting temperature range (ΔT_{m}) (Figure 1B) after a specific thermo-mechanical treatment called programming. Selecting a T_{sep} within ΔT_{m} dividing crystalline domains to actuator domains (AD) and shifting-geometry determining domains (SGD) provided the feasibility to control the partial melting of the crystallizable domains, where heating to T_{sep} resulted in melting induced contraction (MIC) and cooling to T_{low} caused crystallization induced elongation (CIE) (Figure 1B).[75,72] Exploiting such an effect by applying a uniaxial stretching (US) as a programming procedure on a substrate before sputtering process would result in a reversible self-assembly *in-situ* parallel wrinkles (PLW) (switching patterns on/off based on the *in-situ* on/off compressive strain on the substrate), where the dimension of wrinkles can be tuned upon variation of the temperature between T_{low} and T_{sep}.

Furthermore, a triple shape-memory effect (TSME) was also observed in copolymer networks with a broad ΔT_{m} enabling to alter the shapes from permanent shape (C) to the first temporary shape (B) and finally second temporary shape (A).[118,79]

In addition, we hypothesized that reversible *in-situ* multi-patterns (RMP) (complex wrinkles <=> PLW) could be obtained by introducing the second generation of wrinkles (wr_{2G}) of PLW via superposition on the first generation of wrinkles (wr_{1G}) locked earlier on the surface (considered as a pre-patterned surface). Our strategy for doing so was to utilize the TSME of the substrate by permitting the full recovery of shape B as irreversible compressive strain, which would lead to permanent wrinkles (wr_{1G}) on the surface of the bilayer structure. The partial recovery of shape (C) would then implement the capability of rbSME in the substrate. Thermal cycles would then result in a transition between complex wrinkles and PLW on the surface of the bilayer structure. To fulfill the above mentioned requirement, we empowered a sequential biaxial stretching (SEQB) programming on the substrate before sputtering process. To have comprehensive understanding, simultaneous biaxial stretching (SB) was also applied before sputtering process to compare the obtained patters at different temperature-cycles.

As a material basis for both aims, we selected a crosslinked network of poly[ethylene-*co*-(vinyl acetate)], which exhibited a pronounced rbSME[75] and TSME[118] as the compliant substrate and a 10 nm gold layer as the thin film. The influence of various parameters such as the thickness of the gold film or the programming strain on the wavelength and amplitude of the formed wrinkles has been already investigated in a bilayer system having one-way SMP substrates and the gold thin film. [116,119,120]

In this paper, two different copolymer network of poly[ethylene-*co*-(vinyl acetate)] were synthesized and characterized. Thermomechanical properties of the substrates were determined by tensile experiments and the crystalline nanostructures were explored by means of wide-angle X-ray scattering (WAXS). Uniaxial stretching (US), SEQB as well as SB (Figure1D) were performed on the substrate at $T \approx T_{\mathrm{high}}$ relevant to each substrate prior to the deposition of the 10 nm gold film. Reversible surface patterns at different temperatures were observed by means of scanning electron microscopy (SEM) and atomic force microscopy (AFM) and the formed wrinkles were characterized by quantification of the wavelength (λ) and amplitude (A).

Experimental Section

Preparation of the substrate: Two types of poly[ethylene-*co*-(vinyl acetate)] with a vinyl acetate content of 18% (Elvax®460, DuPont) for substrate A and 28% (Elvax®260, DuPont) for substrate B were compounded with 2 wt% dicymyl peroxide (Sigma Aldrich) using a EuroPrismLab twin-screw extruder (Thermo Fischer Scientific, Waltham, MA, USA) at 110 °C and 50 rpm. The substrates were compression molded into 15 cm × 15 cm films with 1 mm thickness at 200 °C with 20 bar for 25 min.

Characterization of the substrates: Two substrates A and B were characterized by determining the gel content (*G*) extracting in toluene as describe elsewhere.[106] Differential scanning calorimetry (DSC) was performed on a calorimeter DSC204 Phoenix (Netzsch, Selb, Germany) with a constant heating and cooling rate of 10 $\mathrm{K{\cdot}min^{-1}}$ in the temperature range between - 100 °C and 100 °C. Tensile tests were performed on a tensile tester Z1.0 (Zwick-Roell, Ulm, Germany) equipped with a thermo chamber and a temperature controller (Eurotherm e2408, Limburg, Germany) at a strain rate of 5 $\mathrm{mm{\cdot}min^{-1}}$ conducted at T_{sep}, and T_{mid} and 100 °C according to the second heating run of the DSC curve of each substrate.

Implementation and quantification of the rbSME of the substrates: the rbSME of two substrates was quantified by cyclic, thermomechanical tensile tests on the tensile tester as described before. Variation of T_{sep}: each measurement included an initial programming step applying a strain ε_{prog} = 50% for the substrate B and $\varepsilon_{\mathrm{prog}}$ = 75% for the substrate A at T_{high} = 100 °C and cooling to T_{low} = 0 °C for both substrates at constant strain, followed by four reversibility cycles under stress-free condition switching between different T_{sep} (55 °C, 60 °C and 65 °C) and T = 25 °C for the substrate B and also T_{sep}s of 65 °C,70 °C, 75 °C and T = 25 °C for the substrate A. Deformation fixation efficiency (Q_{ef}) as well as reversible strain ($\varepsilon_{\mathrm{rev}}$) was calculated as it was addressed in our previous work.[106] Sputtering process of the bilayer structures was performed after the first stress-free cycle as it is marked in Figure 3A.

Sequential biaxial stretching (*SEQB*): A 30 mm × 30 mm film of each substrate was mounted on a tensile tester Z1.0 (Zwick-Roell, Ulm, Germany) equipped with a thermo chamber and a temperature controller (Eurotherm e2408, Limburg, Germany). Firstly, the substrate was stretched uniaxial (US1) by 50% deformation at 100 °C with a strain rate of 5 mm·min^{-1} followed by cooling to 25 °C. Afterwards, the stretched film was re-stretched by applying the second uniaxial stretching of 50% (US2) at T_{sep} determined based on the ΔT_{m} of each substrate (Figure 1D), which was perpendicular to the US1 followed by quenching to 25 °C. The programmed substrates were named as A/B 50(T), where indicated 50% applied strain in US2 at T_{sep}.

Simultaneous biaxial stretching (*SB*): A specimen (cf. reference[121]) was mounted on an ETIFI biaxial stretching machine (CEMEF, Sophia Antipolise, France)[121] and 20% strains in both directions were applied at 100 °C on the substrate with a strain rate of 5 mm·min^{-1} and then cooled to 25 °C.

Preparation of bilayer systems: The programmed substrates were coated with a 10 nm gold layer by means of a sputter coater of Polaron SC7640 (Quorum Technologies Ltd., East Sussed, England) under vacuum at room temperature. The sputtering process was conducted in a four-step of coating process, in which the programmed substrate was covered with 2.5 nm layers of gold, subsequently.

Characterization of the surface: The formed *in-situ* wrinkles were characterized at different temperatures by means of scanning electron microscopy (SEM) on a microscope Phenom G2 pro (Oriel Laser Optik Technologies GmbH und Co. KG, Darmstadt, Germany) using 5 kV, which was equipped with a heating-cooling stage in a non-vacuum mode providing temperatures ranging from -10 °C to 90 °C.

Image analysis and determination of the wavelength of the wrinkles. The wavelength of the obtained wrinkles was estimated by 2D-fast Fourier transformation (2DFFT) method on SEM images using ImageJ software (ImageJ 1.46 r, National Institutes of Health, Bethesda, Maryland, USA).

Atomic force microcopy (AFM): The amplitude of the wrinkles was measured by a NanoScope V microscope (Bruker, Santa Barbara, US) using the tapping mode with a scan rate of 0.3 - 0.5 Hz. High resolution non-contact silicon cantilever (Al-coated) OMCT-AC200TS (spring constant of 9 N/m; resonant frequency of 150 kHz; Tip radius approximately 7 nm) from Olympus (Japan) was used. The taken images were processed by a plan-fit-operation (elimination of curvature and inclination) and were analyzed by the AFM program (Version 7.20 R1.30937).

Cyclic thermo-mechanical experiment: The SEQB programmed samples were tested on a tensile machine as described before under stress-free condition during temperature cycles. The changes in elongation were explored in the direction of US1 as well as US2.

Wide angle X-ray scattering (WAXS) was performed at different temperatures on a Bruker D8 Discover (Bruker AXS, Karlsruhe, Germany) to investigate the orientation of crystalline domains in networks. The X-ray generator was operated at 40 kV and 40 mA on a copper-anode. The collimator was adjusted to 0.8 mm beam size. The two-dimensional detector (Hi-Star) was operated in 1024*1024-pixel mode. The distance sample-detector was 150 mm and the wavelength was $\lambda = 0.15418$ nm. The detector was positioned at an angular position $2\theta = 25°$ in order to cover an angular range from $2\theta = 7.2°$ to 43.5°. Exposure time was 300 s per scattering pattern.

Contact angle measurement: The wettability of bilayer structures was determined by contact angle measurement using Wilhelmy plate method on a K100 at subsequent temperatures (Krüss, Hamburg, Germany).

Results and Discussion:

Two substrates A and B were prepared by compression molding. Substrate A and substrate B showed a broad ΔT_m in the second run of heating of DSC (Figure 2), where the substrate A with 18% of VA showed the broader melting temperature range and also higher overall melting enthalpy ΔH_m (the peak area), indicating the contribution of VA as amorphous segments and hence shorter PE segment in the shifting ΔT_m and lower the degree of crystallinity in the substrate B, which also reflected in the lower elongation at break (ε_B) at 100 °C in rubbery state for the substrate B (Table 1).

Referring to our strategy of programming before the sputtering step (Figure 1B), T_{mid} = 50 °C, T_{sep} = 75 °C for the substrate A as well as T_{mid} = 40 °C, T_{sep} = 60 °C for the substrate B were selected based on the second curve of heating run of DSC.

Table 1 exhibits the results of gel content (*G*) and the elongation at break (ε_B) characterized by tensile test for the substrates A and the substrate B at the defined temperatures. Value of the gel content of 97% for both substrates indicates an almost complete cross-linking reaction. ε_B at specified temperatures of each substrate elucidates the maximum deformation that substrates can tolerate, indicating the range of programming strain (ε_{prog}) before the sputtering process.

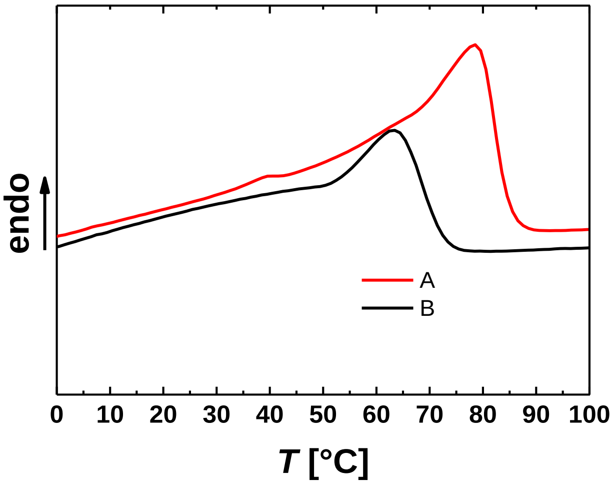

Figure 2. Second DSC heating runs of the substrates A and B showing broad melting temperature ranges. T_{mid} = 50 °C, T_{sep} = 75 °C for the substrate A as well as T_{mid} = 40 °C, T_{sep} = 60 °C for the substrate B were selected based on the DSC curve**.**

Table 1. Gel content, as well as elongation at break of substrate A and the substrate B at different temperatures.

Network ID (VA content [%])	$G^{a)}$ [%]	$\varepsilon_B^{b)}$ [%]	$\varepsilon_B^{c)}$ [%]	$\varepsilon_B^{d)}$ [%]
A (18)	97 ± 3	170 ± 30	330 ± 60	550 ± 60
B (28)	97 ± 1	110 ± 10	310 ± 50	540 ± 50

[a)] Gel content determined by extraction with Toluene at 80 °C, elongation at break (ε_B) determined by tensile tests [b)] at 100 °C, [c)] at $T_{sep,}$ where $T_{sep, A}$ = 75 °C, $T_{sep, B}$ = 60 °C, [d)] at $T_{mid,}$ where $T_{mid, A}$ = 50 °C, $T_{mid, B}$ = 40 °C.

To investigate our first hypothesis (wrinkling on/off), firstly, the rbSME was implemented and quantified for the substrate B by thermomechanical tensile test. In a first set of experiment (Figure 3), in which ε_{prog} = 50% was selected and rbSME was investigated between T_{sep} = 60 °C and 25 °C for four cycles, a uniaxial contraction and expansion of ε_{rev}= 6.6 ± 0.1% was observed upon heating and cooling, respectively (Figure 3A). The identical subsequent cooling-heating cycles was performed on the bilayer structure of programmed substrate B with 10 nm gold layer under SEM and the images of SEM exhibited that the PLW (λ = 1.5 ± 0.3 µm and A = 240 ± 40 nm) was formed on the gold layer surface upon heating cycle, in which the patterns were almost vanished upon cooling to 25 °C (Figure 3B) and this switch on/off PLW patterns were repeated in 3 cycles with the mentioned dimension (Figure 3B). As it is observed in the Figure 3B, from the first cooling cycle, the complete flat surface was not observed on the gold layer. This could be attributed to the different plastic and elastic deformation behaviour of gold layer and copolymer network, although the delamination of gold layer was not observed in any set of experiments, however reaching to the complete flat gold before applying contraction is not scientifically acceptable and was also reported in other study.[68]

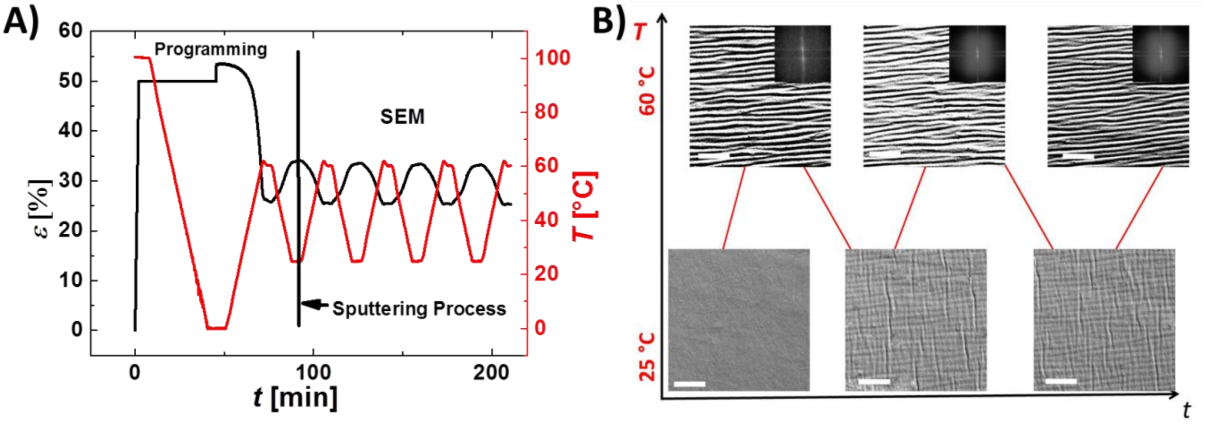

Figure 3. A set of investigations on a bilayer structure consisting of a programmed uniaxial substrate B and a 10 nm gold layer during heating–cooling cycles. A) Thermo-mechanical experiment and attributed post-processes; B) A series of SEM images of the formed PLW wrinkles on the surface of bilayer structure. Scale bar is 10 µm.

Considering the different plastic and elastic deformation behavior of the metallic film and the polymeric substrate in a bilayer structure as well as counting the minimum sufficient strain of 3% generating wrinkles from the studies of others[57] was the reason of choosing 25 °C as T_{low} in heating-cooling cycles to control the implement reversible strain of MIC and CIE into the lower value as 10 nm gold layer would not bear the higher deformation. It is important to keep in mind that increasing the number of thermal cycles on this bilayer structure would lead to the fatigue behavior and cracking and delamination of the gold thin film. Nevertheless, the substrate is able to bear higher cycle number based on the crystallization domains.[72]

In this study, the thickness of 10 nm gold film gold was not measured and quantified after the sputtering process. However, literature studies showed that the gradient thickness of gold film resulted to formation of hierarchical wrinkles[47], which was not observed here. Although there was no measurement of exact 10 nm gold film on the substrate, but due to the no evidence of hierarchical wrinkles on the surface, the uniform thickness of gold film could be assured. Contact angle measurement disclosed that by increasing the temperature from room temperature to 60 °C (Figure 3B), a lightly decrease of the advancing angle from 72 ± 2° to 68 ± 1° and the receding angle from 35 ± 1° to 24 ± 1° was observed in the subsequent heating-cooling cycles.

The above set of experiments were repeated for the bilayer structure of substrate B and 10 nm gold film, in which T_{sep} was varied, and the result is summarized in Table 2. Altering T_{sep} varied the reversible strains and fixation efficiency, where the highest Q_{ef} = 92 ± 2 % was observed at the T_{sep} = 55 °C and the relevant reversible strain was 4.5 ± 0.1 %, however, when T_{sep} was 65 °C, the lowest Q_{ef} = 38 ± 2 % with the relevant reversible stain of 5.3 ± 0.1 % was measured. Increasing T_{sep} from 55 °C to 65 °C altered also the dimension of PLW wrinkles, where λ was decreased from 1.6 ± 0.1 µm to 1.2 ± 0.4 µm and A was increased from 130 ± 30 nm to 270 ± 10 nm, respectively. These changes tailored lightly the wettability of the surface (Table 2), in which the PLW with smaller wavelengths and higher amplitudes presented a more hydrophilic surface, where θ_{A} was decreased from 70 ± 2 ° to 66 ± 1 ° and θ_{R} was also decreased from 25 ± 2 to 22 ± 3 (Table 2).

This result was also proved by investigations on set of experiments on the bilayer structure having a substrate A and a 10 nm gold layer (Table 3). For this bilayer system, increasing T_{sep} in 5 °C steps from 65 °C to 75 °C resulted in an increase of reversible strain from 6.1 ± 0.1% to 9.6 ± 0.1%, a decrease of the wavelength of the formed wrinkles from 1.6 ± 0.1 µm to 0.6 ± 0.1 µm as well as an increase of amplitude from 180 ± 50 nm to 370 ± 50 nm leading to the decrease of the advancing angle from 66 ± 1° to 51 ± 1° and receding angle from 35 ± 1° to 19 ± 1°.

Table 2. Correlation between the rbSME, formed PLW, and wettability of the surface as function of T_{sep} for the bilayer structure consisting of uniaxial programmed substrate B (ε_{prog} = 50%) and a 10 nm gold layer.

T_{sep} [°C]	ε_{rev}[a)] [%]	Q_{ef}[b)] [%]	λ[c)] [µm]	A[d)] [nm]	θ_A[e)] [°]	θ_R[f)] [°]
55	4.5 ± 0.1	92 ± 2	1.6 ± 0.1	130 ± 30	70 ± 2	25 ± 2
60	6.6 ± 0.1	72 ± 2	1.5 ± 0.2	190 ± 10	68 ± 1	24 ± 1
65	5.3 ± 0.1	38 ± 2	1.2 ± 0.4	270 ± 10	66 ± 1	22 ± 3

[a)] Reversible strain, [b)] Fixation efficiency, [c)] Wavelength, [d)] Amplitude [e)] Advancing contact angle, [f)] Receding contact angle.

Table 3. Correlation between the rbSME, formed PLW, and wettability of the surface as function of T_{sep} for the bilayer structure consisting of uniaxial programmed substrate A (ε_{prog} = 75%) and a 10 nm gold layer.

T_{sep} [°C]	ε_{rev}[a)] [%]	Q_{ef}[b)] [%]	λ[c)] [µm]	A[d)] [nm]	θ_A[e)] [°]	θ_R[f)] [°]
65	6.1 ± 0.1	70 ± 2	1.6 ± 0.1	180 ± 50	66 ± 1	35 ± 1
70	7.5 ± 0.1	40 ± 2	1.1 ± 0.1	240 ± 40	57 ± 1	32 ± 1
75	9.6 ± 0.1	20 ± 2	0.6 ± 0.1	370 ± 50	51 ± 1	19 ± 1

a) Reversible strain, [b)] Fixation efficiency, [c)] Wavelength, [d)] Amplitude [e)] Advancing contact angle, [f)] Receding contact angle

Comparing the result of Table 2 and Table 3 shows that there is no clear correlation between reversible strain and fixation efficiency on the wavelength and also the amplitude, however, the drastic decrease of Q_{ef} shows the drastic increase of amplitude, measured by AFM. This could be explained by a hidden stress trapped in the gold film during the elastic-plastic mechanical deformation and variation of ε_{rev} and Q_{ef} might affect the influence of this hidden stress on the dislocation of grain size, intragraunlar dislocation of gold grains and grain boundaries shear stress.[101,122] Understanding the correlation of these parameters requires deeper study to find the mechanism in nano scale. Nevertheless, we demonstrated the general approach for formation of switching on/off *in-situ* PLW on surface, which was confirmed on two double layer systems. The reversible self-assembly PLW was tunable by variation of temperature and affected the wettability of the surface.

In the second part of this paper, we investigate a general approach of generating a reversible *in-situ* multi-patterns (RMP) (complex wrinkles <=> PLW). We assumed that by choosing suitable temperatures for programming in two directions, the combination of rbSME and TSME could be implemented on the substrates. In order to do so, both substrates A and B were programmed prior to the sputtering process by SEQB stretching mode at defined temperatures (Figure 1D). For the substrate B, the first US1 stretching of 50% strain was applied at 100 °C and cooled down to 25 °C. Subsequently, the US2 of 50% was applied at T_{sep} = 60 °C and cooled down to the room temperature. By applying the first heating run to the T_{sep} on the bilayer structure of substrate B and the 10 nm gold layer, in which US2 was programmed, the first generation of PLW (wr_{1G}) were locked on the surface created the pre-patterned surface. Decreasing the temperature to T_{mid} (40 °C), the complex pattern (i.e. Diamond wrinkles) were appeared on the surface, which was vanished by heating to the T_{sep} = 60 °C. The RMP was repeated one more cycle with the same result. (Figure 4A).

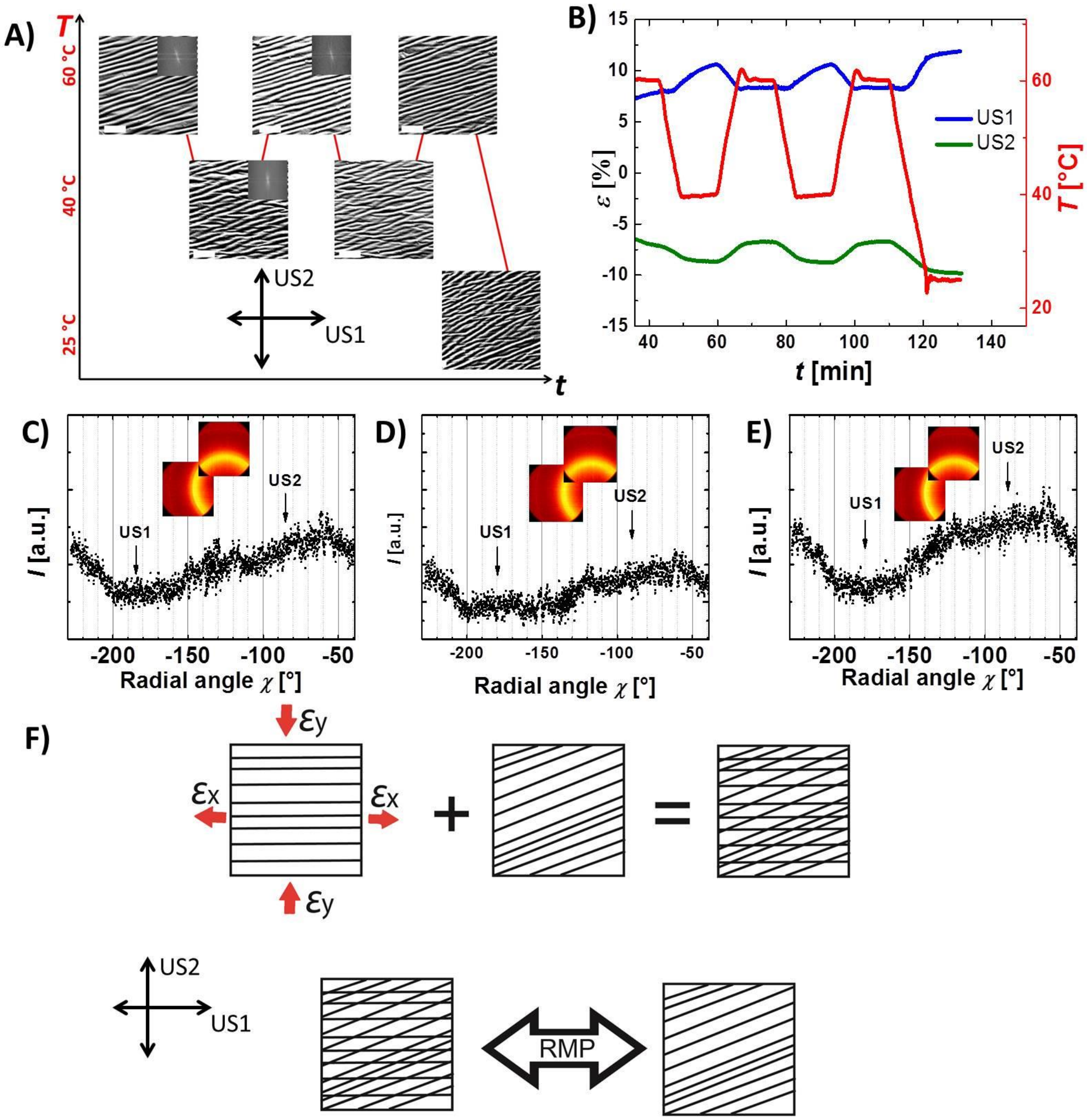

Figure 4. A) A series of SEM images of a SEQB programmed substrate B50(60) covered with a 10 nm gold layer during heating–cooling cycles revealing reversible self-assembly *in-situ* patterns (diamond-like wrinkles at 40 °C and PLW at 60 °C). Scale bar is 10 µm; B) Study on the behavior of the SEQB programmed substrate B50(60) within heating–cooling cycles following the same temperature cycles employed in SEM; Red line: temperature; blue line: elongation after SEQB upon heating in direction of US1; green line: elongation after SEQB upon heating in direction of US2; WAXS result of a SEQB programmed substrate: C) at 40 °C; D) at 60 °C; E) at 40 °C; F) Proposed mechanism for the creation of the permanent wrinkles (wr_{1G}) at T_{mid} induced by rbSME on the substrate. The superposition of the permanent (wr_{1G}) and temporary (wr_{2G}) wrinkles provided diamond-like wrinkles.

To understand the mechanism of the creation of the RMP based on the imposed changes in two dimensions and consequent strains upon altering temperature on the substrate, a programmed substrate B was cut in the direction of US1 and US2 and investigated in the analogous conditions (stress-free and subsequent heating–cooling cycles) via thermomechanical experiments (Figure 5). The result of stress-free thermomechanical test shows that, upon first heating from 25 °C to 60 °C, the sample showed an increase of 7% strain in the US1 sample and a decrease of 6% strain in US2, which was attributed to the full first recovery of shape (B) from TSME (Figure 5C and Figure 5D), which resulted in the formation of locking wr_{1G} on the bilayer structure (Figure 5B). Moreover, the wr_{1G} was created along the slanted direction between US1 and US2 at $T_{sep} = 60$ °C.

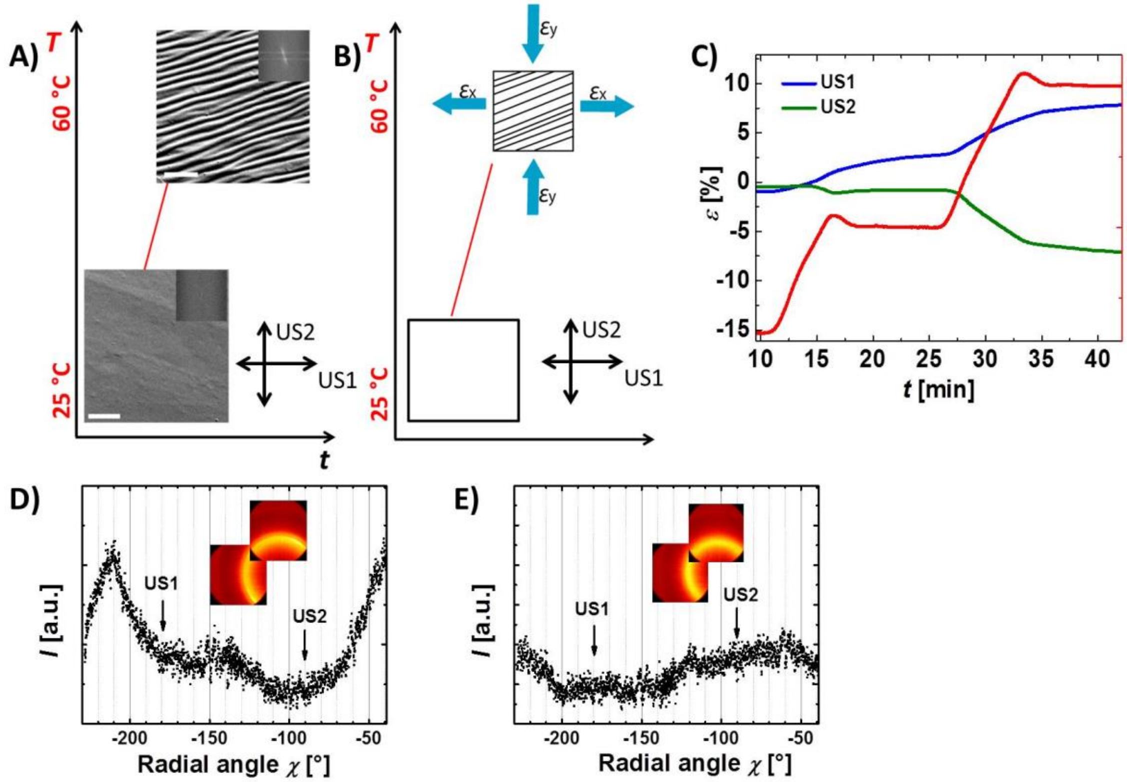

Figure 5. A) SEM images of a SEQB programmed substrate B50(60) covered with a 10 nm gold layer upon first heating. Scale bar is 10 µm. The inset (2DFFT) reveals the formation of permanent wrinkles (wr_{1G}) by first heating to T_{sep} = 60 °C; B) Proposed mechanism for the creation of the permanent wrinkles in the bilayer (top view) structures having a SEQB programmed substrate and 10 nm gold layer generated by total compressive strain induced at T_{sep} = 60 °C; C) Thermo-mechanical experiment on the SEQB programmed substrate B50(60) within the first heating run; Red line: temperature; blue line: elongation after SEQB upon heating in direction of US1; green line: elongation after SEQB upon heating in direction of US2; WAXS result of a SEQB programmed substrate: D) at room temperature and E) at T_{sep} = 60 °C

The orientation of the crystalline domains was explored via WAXS experiments by determining the radial (azimuthal) profile of the polyethylene (110) reflection, which is perpendicular to the molecular chain direction. After SEQB programming the profile exhibited some non-uniform 4-point character (Figure 3D) without distinct maxima in US1 or US2, which was attributed to the perpendicular 2-step programming at different temperatures, which could be related to some biaxial orientation of the crystalline domains. After the first heating to T_{sep} = 60 °C the radial profile exhibited a 2-point (sickle-like) character with maxima in the US2 direction (Figure 5E), which reflected the uniaxial orientation of the crystals with the molecular chain axis along the US1 direction. This was related to the full recovery of the temporary shape (B) of the TSME, where crystals oriented upon US2 melted and the uniaxial character from US1 was recovered. Figure 4 presented the result of SEM, thermo mechanical experiments for the following heating-cooling cycles between T_{sep} = 60 °C and T_{mid} = 40 °C resulted in the rbSME with a reversible strain of 2% in the direction of US1 (Figure 4B) leading to the formation of second generation of wrinkles (wr_{2G}) (reversible PLW). The orientation of the crystalline domains during stress-free heating-cooling cycles was explored by WAXS measurements. Figure 4C-E shows the radial profile of the polyethylene (110)-reflection. It was observed, that the uniaxial character with the molecular chain direction along US1 (peak maxima on US2) was not altered upon subsequent heating-cooling cycles, only the peak intensity (related to the degree of crystallinity) was changed. This was attributed to the uniaxial CIE/MIC mechanism of the rbSME as observed in previous works.[72] Figure 4F demonstrates a simple mechanism of the superposition of permanent wrinkles (wr_{1G}) and temporary wrinkles (wr_{2G}), where led to the formation of diamond-like wrinkles (complex wrinkles), in which the direction of wrinkles (PLW vs. diamond-like wrinkle) was confirmed by 2DFFT images (insets in Figure 4A). As a result, RMP was obtained. The wavelengths of the locked wr_{1G} of the bilayer structure having the substrate B50(60) were determined as 1.3 ± 0.1 µm (A = 540 ± 100 nm) at T_{sep} = 60 °C and 2.1 ± 0.1 µm (A = 430 ± 30 nm) at T_{mid} = 40 °C. Furthermore, the wavelength of the wr_{2G} of this substrate was 2.1 ± 0.1 µm (A = 230 ± 40 nm) generated at T_{mid} = 40 °C.

Formation of RMP was also observed for the bilayer structure having a A50(75) substrate and a 10 nm gold layer, where T_{sep} and T_{mid} were defined at 75 °C and 50 °C, respectively, in which reversible strain was 3% (Figure 6). In addition, the wavelength of the wr_{1G} in this bilayer structure was quantified as 1.3 ± 0.1 µm (A = 200 ± 30 nm) at T_{sep} = 75 °C and 1.6 ± 0.1 µm (A = 150 ± 20 nm) at T_{mid} = 50 °C. The temporary wrinkles (wr_{2G}) of this bilayer system had a wavelength of 2.1 ± 0.3 µm and amplitude of 100 ± 20 nm at T_{mid} = 50 °C.

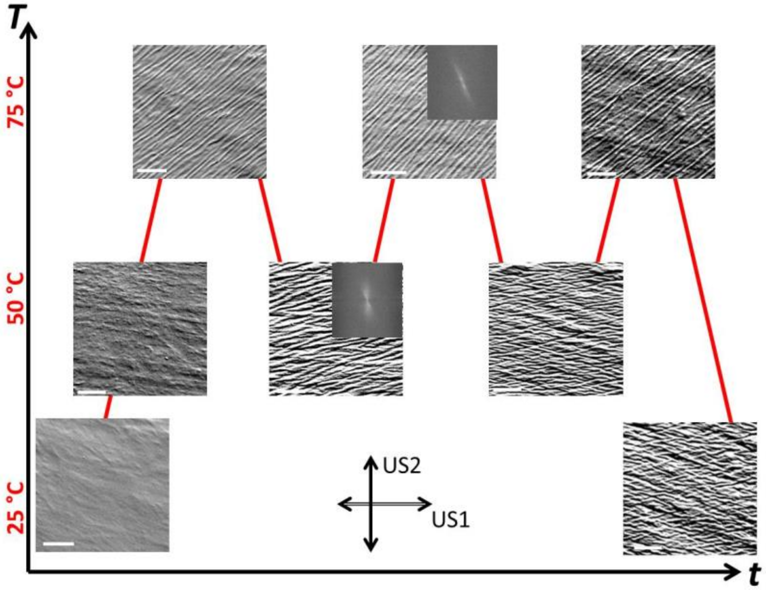

Figure 6. A series of SEM images of a SEQB programmed substrate A50(75) covered with a 10 nm gold layer during heating-cooling cycles. The inset (2DFFT) was obtained using ImageJ software. The scale bar is 10 µm.

The changes of dimension of wr_{1G} at two different temperatures could be attributed to the variation of total compressive strain during the generation of wr_{2G} and also by the variation of Young's modulus of the substrate as a function of temperature.[123,44]

Investigations of the influence of RMP on the wettability of the surface (Figure 7) indicated that despite of the different surface morphology at T_{sep} and T_{mid} (PLW and diamond-like wrinkles), the advancing and receding angle was not altered significantly, due to the presence of permanent wrinkles (wr_{1G}) on the surface.

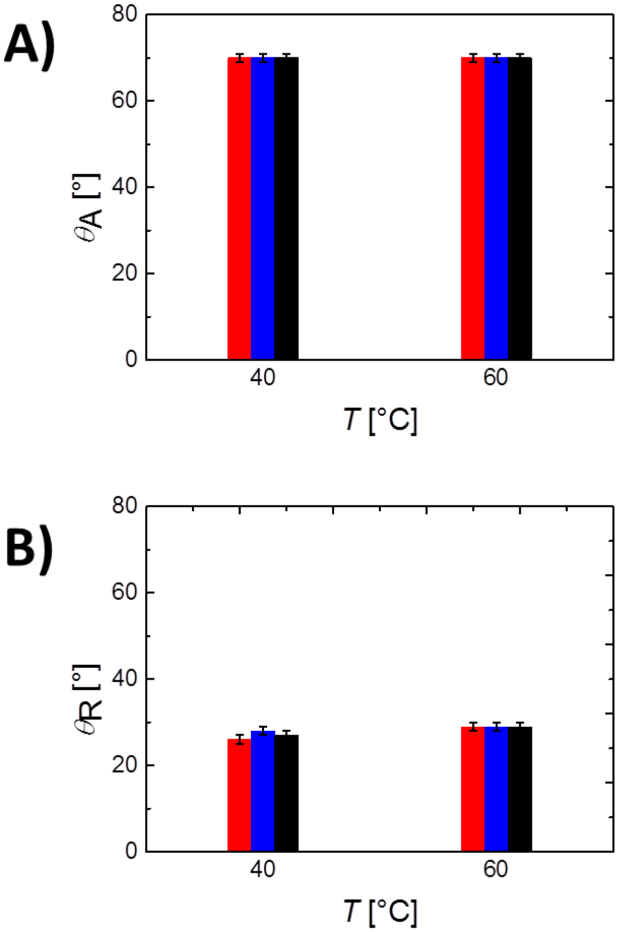

Figure 7. Advancing and receding angle of the surface of a bilayer structure having B50(40) substrate and a 10 nm gold layer in thermal cycles. Red: cycle 1; blue: cycle 2; black: cycle 3.

In order to compare different patterns created by SEQB and SB programming of substrates, a substrate (Figure 1D) was also programmed in SB mode as it was described in experimental section. Upon heating to T_{sep} on the bilayer structure on the SEM heating stage (Figure 8), various types of wrinkles ranging from PLW to labyrinth wrinkles were created depends on the distance from the center. There is a transition of patterns were observed, in which the patterns were transformed from patterns created by equi-biaxial strains located in the center to parallel wrinkles induced by uniaxial stretching at the edges. Such changes of patterns were also confirmed by WAXS experiment, which were based on the localized order of crystalline domains in the substrate (Figure 9). Furthermore, the obtained patterns did not change after cooling to T_{low} = 25 °C. This behavior was attributed to in-plane isotropy and poor crystalline order in the film stretched by SB (Figure 9). The obtained result is in full agreement with the poor crystalline domains studied in the biaxial films processing.[124]

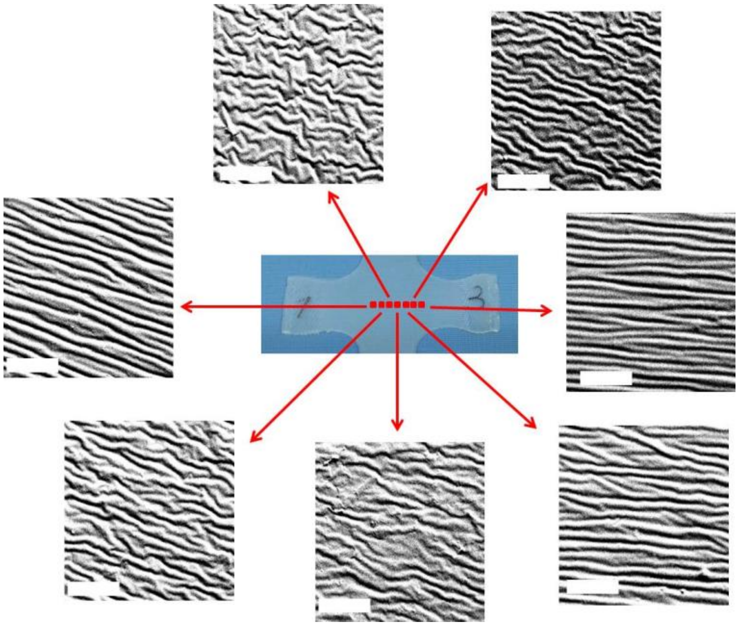

Figure 8. SEM images of the SB programmed substrate A at different positions in the central part. Scale bar is 50 µm.

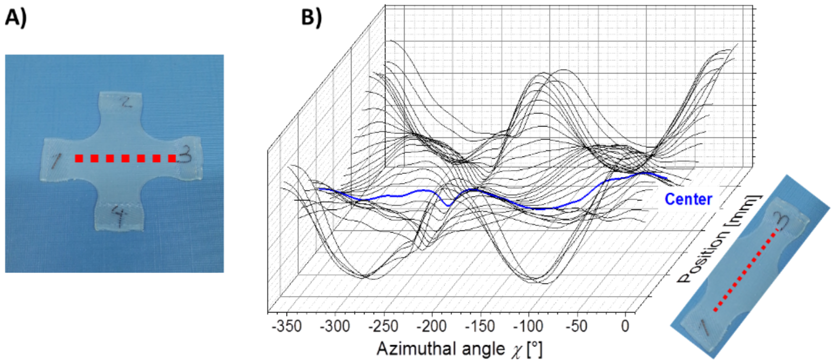

Figure 9. A) The SB programmed substrate A at room temperature before the sputtering process; B) Azimuthal (radial) profile of the PE (110) reflection of substrate A after SB programming. The positions of the measurements are indicated (equidistant points at 1 mm). The graph shows low degree of crystalline order in the central part.

In this way, bidirectional reversible surface morphology *in-situ* was generated in bilayer structure for the first time utilizing an implementation of rbSME on the substrate. *In-situ* transition of surface morphology only by variation of temperature can have enormous potential applications in many fields, which are based on the surface-properties ranging from hydrodynamic drag and friction to wettability of surfaces and roughness. Empowering this switch on/off patterns and RMP could be promising in biomedical application and cell culture environment in order to guide cells on the aligned desirable direction, if the relevant temperature of forming wrinkles can be designed at body temperature and the lower one (for cell-culturing). In order to achieve that, a substrate having rbSME at relevant physiological temperature [79,106,78] within the bilayer structure could be used on this system. In addition, gold is also considered as non-toxic material, which is suitable for health technology. The substrate adjusting rbSME around body temperature was presented in our last work.[106] Nevertheless, controlling the imposed temperature while sputtering would erase the programmed implemented on the substrate.[125] In the case of controlling the introduced temperature or an alternative way to deposit a gold film on the programmed substrate, this *in-situ* changing patterns could open a bright window for the investigation of cellular response to different topographies as well as biomedical applications in stem cell biology and tissue engineering.[126,127,51] This study was focused on the possibility of the formation on/off patterns *in-situ* by empowering rbSME on a substrate of the bilayer structure. The correlation of reversible strain and fixation efficiency in molecular level in the substrate as well as imposed strain on the gold metal film, the behavior of the elastic-plastic behavior of gold thin film in relation to the grain size and grain size boundaries of gold in different thickness during the reversible cycles and the factor of fatigue on metal behavior demand extensive parametric studies in experiment and numerical investigations.

Conclusion:

Two bilayer structures consisting of a substrate showing rbSME and a 10 nm gold layer enabled bidirectional reversible wrinkling patterns upon several heating-cooling cycles. Two substrates of poly[ethylene-*co*-(vinyl acetate)] with two different percentage of vinyl acetate content exhibited a broad melting range, which was the requirement of implementation of rbSME into the polymer networks. The substrates were programed in two different modes prior to sputtering process. The bilayer structure having a uniaxial direction programmed showed reversible wrinkles with a wavelength of 1.5 ± 0.3 µm and amplitude of 240 ± 40 nm upon heating to T_{sep} = 60 °C, whereas wrinkles were vanished while cooling down to 25 °C. The on/off wrinkles were repeated in the subsequent heating-cooling cycles, where affected the wettability of surface. Variation of T_{sep} changed the dimension of wrinkles. Moreover, applying sequential biaxial stretching prior to the sputtering process caused the combination of TSME and rbSME on the substrate in two different directions, resulted in to the locking of first generation wrinkles considered as permanent pattern in the first heating stress-free run and also second generation of wrinkles considered as temporary wrinkles upon cooling. The superposition of these wrinkles in cooling-heating cycles resulted in to the *in-situ* reversible multi-patterns. Also, it was found that employing simultaneous biaxial stretching led to poor order of crystalline domains, which caused irreversible heterogeneous patterns. In this way, bidirectional reversible morphology of surfaces can be a promising feature for smart applications based on the surface properties.

Acknowledgment:

The authors would like to thank Prof. Billon and Dr. Combeaud for offering an opportunity to use ETIFI machine at CEMEF campus of Paris Tech in this project.

References

1. Holzapfel GA, Sommer G, Gasser CT, Regitnig P. Determination of layer-specific mechanical properties of human coronary arteries with nonatherosclerotic intimal thickening and related constitutive modeling. *Am J Physiol - Hear Circ Physiol*. 2005;289(5 58-5):2048-2058. doi:10.1152/ajpheart.00934.2004
2. M.D Humzah R. S. Human intervertebral disc: Structure and function. *Anat Rec*. 1988;220(4):337-356. http://dx.doi.org/10.1002/ar.1092200402
3. Genzer J, Groenewold J. Soft matter with hard skin: From skin wrinkles to templating and material characterization. *Soft Matter*. 2006;2(4):310. doi:10.1039/b516741h
4. O’Shea TM, Miao X. Bilayered scaffolds for osteochondral tissue engineering. *Tissue Eng Part B Rev*. 2008;14(4):447-464. doi:10.1089/ten.teb.2008.0327
5. Harley B a, Lynn AK, Wissner-Gross Z, Bonfield W, Yannas I V, Gibson LJ. Design of a multiphase osteochondral scaffold III: Fabrication of layered scaffolds with continuous interfaces. *J Biomed Mater Res A*. 2010;92(3):1078-1093. doi:10.1002/jbm.a.32387
6. Titov VN. The functional role of arterial intima. Endogenous and exogenous pathogens and specificity of atheromatosis as an inflammation. *Klin Lab Diagn*. 2003;(2):23—4, 33—7. http://europepmc.org/abstract/MED/12688211
7. Sarkar S, Schmitz-Rixen T, Hamilton G, Seifalian AM. Achieving the ideal properties for vascular bypass grafts using a tissue engineered approach: a review. *Med Biol Eng Comput*. 2007;45(4):327-336. doi:10.1007/s11517-007-0176-z
8. Behl M, Razzaq MY, Lendlein A. Multifunctional shape-memory polymers. *Adv Mater*. 2010;22(31):3388-3410. doi:10.1002/adma.200904447
9. Lendlein A, Balk M, Tarazona NA, Gould OEC. Bioperspectives for Shape-Memory Polymers as Shape Programmable, Active Materials. *Biomacromolecules*. 2019;20(10):3627-3640. doi:10.1021/acs.biomac.9b01074
10. Lendlein A, Trask RS. Multifunctional materials: Concepts, function-structure relationships, knowledge-based design, translational materials research. *Multifunct Mater*.

2018;1(1). doi:10.1088/2399-7532/aada7b

11. Wischke C, Neffe AT, Hanh BD, et al. A multifunctional bilayered microstent as glaucoma drainage device. *J Control Release*. 2013;172(3):1002-1010. doi:10.1016/j.jconrel.2013.10.021
12. Hutmacher DW, Schantz JT, Xu C, Lam F, Tan KC, Lim TC. State of the art and future directions of scaffold-based bone engineering from a biomaterials perspective. *J Tissue Eng Regen Med*. 2007;1(June):245-260. doi:10.1002/term
13. Hutmacher DW, Schantz T, Zein I, Ng KW, Teoh SH, Tan KC. Mechanical properties and cell cultural response of polycaprolactone scaffolds designed and fabricated via fused deposition modeling. *J Biomed Mater Res*. 2001;55(2):203-216. http://www.ncbi.nlm.nih.gov/pubmed/11255172
14. Mikos a G, Sarakinos G, Leite SM, Vacanti JP, Langer R. Laminated three-dimensional biodegradable foams for use in tissue engineering. *Biomaterials*. 1993;14(5):323-330. http://www.ncbi.nlm.nih.gov/pubmed/8507774
15. Mao JS, Zhao LG, Yin YJ, Yao K De. Structure and properties of bilayer chitosan–gelatin scaffolds. *Biomaterials*. 2003;24(6):1067-1074. http://www.ncbi.nlm.nih.gov/pubmed/12504529
16. Ghosh S, Viana JC, Reis RL, Mano JF. Bi-layered constructs based on poly(l-lactic acid) and starch for tissue engineering of osteochondral defects. *Mater Sci Eng C*. 2008;28(1):80-86. doi:10.1016/j.msec.2006.12.012
17. Yunos DM, Ahmad Z, Salih V, Boccaccini a R. Stratified scaffolds for osteochondral tissue engineering applications: electrospun PDLLA nanofibre coated Bioglass®-derived foams. *J Biomater Appl*. 2013;27(5):537-551. doi:10.1177/0885328211414941
18. Reignier J, Huneault M. Preparation of interconnected poly(ε-caprolactone) porous scaffolds by a combination of polymer and salt particulate leaching. *Polymer (Guildf)*. 2006;47(13):4703-4717. doi:10.1016/j.polymer.2006.04.029
19. Sca M, Mendibil X, Virginia S, Viteri D, Ugartemendia JM. High Throughput Manufacturing of Bio-Resorbable. *Polymers (Basel)*. 2020;12(34).
20. Washburn NR, Simon CG, Tona A, Elgendy HM, Karim A, Amis EJ. Co-extrusion of biocompatible polymers for scaffolds with co-continuous morphology. *J Biomed Mater Res*. 2001;60:21-29. doi:10.1002/jbm.10049
21. Oh S. Fabrication and characterization of hydrophilic poly(lactic-co-glycolic acid)/poly(vinyl alcohol) blend cell scaffolds by melt-molding particulate-leaching method. *Biomaterials*. 2003;24(22):4011-4021. doi:10.1016/S0142-9612(03)00284-9
22. Sarazin P, Roy X, Favis BD. Controlled preparation and properties of porous poly(L-lactide) obtained from a co-continuous blend of two biodegradable polymers. *Biomaterials*. 2004;25(28):5965-5978. doi:10.1016/j.biomaterials.2004.01.065
23. Sun ZB, Song YN, Ma GQ, et al. Imparting Gradient and Oriented Characters to Cocontinuous Structure for Improving Integrated Performance. *Macromol Chem Phys*. 2021;222(10):1-10. doi:10.1002/macp.202100012
24. Liu Q, Liu Y, Jiang C, Zheng S. Modeling and simulation of weld line location and properties during injection molding based on viscoelastic constitutive equation. *Rheol Acta*. 2020;59(2005):109121. doi:https://doi.org/10.1007/s00397-019-01182-8
25. Vendan, S.A., Natesh, M., Garg, A., Gao L. Polymer Welding Techniques and Its Evolution. In: *Onfluence of Multidisciplinary Sciences for Polymer Joining.* Springer, Singapore; 2019. doi:https://doi.org/10.1007/978-981-13-0626-6_2

26. Haugen H, Will J, Fuchs W, Wintermantel E. A Novel Processing Method for Injection-Molded Polyether – Urethane Scaffolds . Part 1 : Processing. *J Biomed Mater Res B Appl Biomater*. 2006;77(1):65-72. doi:10.1002/jbm.b.30396
27. Jiang J, Li Z, Yang H, Wang X, Li Q, Turng L-S. Microcellular injection molding of polymers: a review of process know-how, emerging technologies, and future directions. *Curr Opin Chem Eng*. 2021;33:100694. doi:10.1016/j.coche.2021.100694
28. Ding Y, Hassan MH, Bakker O, Hinduja S, Bártolo P. A review on microcellular injection moulding. *Materials (Basel)*. 2021;14(15). doi:10.3390/ma14154209
29. Guarino V, Guaccio A, Ambrosio L. Manipulating co-continuous polymer blends to create pcl scaffolds with fully interconnected and anisotropic pore architecture. *J Appl Biomater Biomech*. 2011;9(1):34-39. doi:10.5301/JABB.2011.6473
30. Kramschuster A, Turng L-S. An injection molding process for manufacturing highly porous and interconnected biodegradable polymer matrices for use as tissue engineering scaffolds. *J Biomed Mater Res B Appl Biomater*. 2010;92(2):366-376. doi:10.1002/jbm.b.31523
31. Quirk R a., France RM, Shakesheff KM, Howdle SM. Supercritical fluid technologies and tissue engineering scaffolds. *Curr Opin Solid State Mater Sci*. 2004;8(3-4):313-321. doi:10.1016/j.cossms.2003.12.004
32. Goel SK, Beckman EJ. Generation of Microcellular Polymeric Foams Using Supercritical Carbon Dioxide. I: Effect of Pressure and Temperature on. *Polym Eng Sci*. 1994;34(74):1137-1147.
33. Chen C-X, Liu Q-Q, Xin X, Guan Y-X, Yao S-J. Pore formation of poly(ε-caprolactone) scaffolds with melting point reduction in supercritical CO 2 foaming. *J Supercrit Fluids*. 2016;117:279-288. doi:10.1016/j.supflu.2016.07.006
34. Song C, Luo Y, Liu Y, et al. Fabrication of PCL Scaffolds by Supercritical CO2 Foaming Based on the Combined Effects of Rheological and Crystallization Properties. *Polymers (Basel)*. 2020;12(4):780. doi:10.3390/polym12040780
35. Guo H, Jiang J, Li Z, et al. Solid-State Supercritical CO2 Foaming of PCL/PLGA Blends: Cell Opening and Compression Behavior. *J Polym Environ*. 2020;28(7):1880-1892. doi:10.1007/s10924-020-01732-9
36. Georgiou G, Mathieu L, Pioletti DP, et al. Polylactic Acid – Phosphate Glass Composite Foams as Scaffolds for Bone Tissue Engineering. *J Biomed Mater Res Part B*. 2006;80:322-331. doi:10.1002/jbmb
37. Guarino V, Causa F, Taddei P, et al. Polylactic acid fibre-reinforced polycaprolactone scaffolds for bone tissue engineering. *Biomaterials*. 2008;29(27):3662-3670. doi:10.1016/j.biomaterials.2008.05.024
38. Kang Y, Scully A, Young D a, et al. Enhanced mechanical performance and biological evaluation of a PLGA coated β-TCP composite scaffold for load-bearing applications. *Eur Polym J*. 2011;47(8):1569-1577. doi:10.1016/j.eurpolymj.2011.05.004
39. Park J-E, Todo M. Development of layered porous poly(l-lactide) for bone regeneration. *J Mater Sci*. 2010;45(14):3966-3968. doi:10.1007/s10853-010-4564-7
40. Sanz-Horta R, Elvira C, Gallardo A, Reinecke H, Rodríguez-Hernández J. Fabrication of 3d-printed biodegradable porous scaffolds combining multi-material fused deposition modeling and supercritical Co2 techniques. *Nanomaterials*. 2020;10(6). doi:10.3390/nano10061080
41. Song C, Li S, Zhang J, et al. Controllable fabrication of porous PLGA/PCL bilayer

membrane for GTR using supercritical carbon dioxide foaming. *Appl Surf Sci*. 2019;472:82-92. doi:10.1016/j.apsusc.2018.04.059

42. Higham TE, Russell AP, Niewiarowski PH, Wright A, Speck T. The Ecomechanics of Gecko Adhesion: Natural Surface Topography, Evolution, and Biomimetics. *Integr Comp Biol*. 2019;59(1):148-167. doi:10.1093/icb/icz013
43. Ensikat HJ, Ditsche-Kuru P, Neinhuis C, Barthlott W. Superhydrophobicity in perfection: the outstanding properties of the lotus leaf. *Beilstein J Nanotechnol*. 2011;2:152-161. doi:10.3762/bjnano.2.19
44. Wu K, Sun Y, Yuan H, Zhang J, Liu G, Sun J. Harnessing Dynamic Wrinkling Surfaces for Smart Displays. *Nano Lett*. 2020;20(6):4129-4135. doi:10.1021/acs.nanolett.9b05279
45. Dean B, Bhushan B. Shark-skin surfaces for fluid-drag reduction in turbulent flow: a review. *Philos Trans R Soc A Math Phys Eng Sci*. 2010;368(1929):4775-4806. doi:10.1098/rsta.2010.0201
46. Songshan Zeng,Rui Li,Stephan G. Freire,Vivian M. M. Garbellotto,Emily Y. Huang,Andrew T. Smith,Cong Hu,William R. T. Tait,Zichao Bian,Guoan Zheng,Dianyun Zhang LS. Moisture-Responsive Wrinkling Surfaces with Tunable Dynamics. *Adv Mater*. 2017;29(24):1700828. doi:https://doi.org/10.1002/adma.201700828
47. Ma L, He L, Ni Y. Tunable hierarchical wrinkling: From models to applications. *J Appl Phys*. 2020;127(11). doi:10.1063/1.5143651
48. Ware CS, Smith-Palmer T, Peppou-Chapman S, et al. Marine Antifouling Behavior of Lubricant-Infused Nanowrinkled Polymeric Surfaces. *ACS Appl Mater Interfaces*. 2018;10(4):4173-4182. doi:10.1021/acsami.7b14736
49. Bae HJ, Bae S, Park C, et al. Biomimetic Microfingerprints for Anti-Counterfeiting Strategies. *Adv Mater*. 2015;27(12):2083-2089. doi:10.1002/adma.201405483
50. Raj SS, Mathew RM, Nair Y, S. T. A, T. P. V. Fabrication and Applications of Wrinkled Soft Substrates: An Overview. *ChemistrySelect*. 2022;7(16):1-6. doi:10.1002/slct.202200714
51. Nomin-Erdene Oyunbaatar, Pooja P. Kanade D-WL. Stress-assisted gold micro-wrinkles on a polymer cantilever for cardiac tissue engineering. *Colloids Surfaces B Biointerfaces*. 2022;209:112210. doi:https://doi.org/10.1016/j.colsurfb.2021.112210
52. IM S, HUANG R. Wrinkle patterns of anisotropic crystal films on viscoelastic substrates. *J Mech Phys Solids*. 2008;56(12):3315-3330. doi:10.1016/j.jmps.2008.09.011
53. Park J-Y, Chae HY, Chung C-H, et al. Controlled wavelength reduction in surface wrinkling of poly(dimethylsiloxane). *Soft Matter*. 2010;6(3):677. doi:10.1039/b916603c
54. Chen Z, Young Kim Y, Krishnaswamy S. Anisotropic wrinkle formation on shape memory polymer substrates. *J Appl Phys*. 2012;112(12):124319. doi:10.1063/1.4770483
55. Chen X, Hutchinson JW. A family of herringbone patterns in thin films. *Scr Mater*. 2004;50(6):797-801. doi:10.1016/j.scriptamat.2003.11.035
56. Wang Z, Hansen C, Ge Q, et al. Programmable, pattern-memorizing polymer surface. *Adv Mater*. 2011;23(32):3669-3673. doi:10.1002/adma.201101571
57. Xie T. Tunable polymer multi-shape memory effect. *Nature*. 2010;464(7286):267-270. doi:10.1038/nature08863
58. Lin G, Li J, Xu Z, Ge D, Sun W, Chen P. Hierarchical Surface Patterns via Global Wrinkling on Curved Substrate for Fluid Drag Control. *Adv Mater Interfaces*. 2021;8(1):2001489. doi:10.1002/admi.202001489
59. Al-Rashed R, López Jiménez F, Marthelot J, Reis PM. Buckling patterns in biaxially pre-

stretched bilayer shells: wrinkles, creases, folds and fracture-like ridges. *Soft Matter*. 2017;13(43):7969-7978. doi:10.1039/C7SM01828B

60. Li F, Hou H, Yin J, Jiang X. Near-infrared light–responsive dynamic wrinkle patterns. *Sci Adv*. 2018;4(4). doi:10.1126/sciadv.aar5762
61. Zong C, Zhao Y, Ji H, et al. Tuning and Erasing Surface Wrinkles by Reversible Visible-Light-Induced Photoisomerization. *Angew Chemie Int Ed*. 2016;55(12):3931-3935. doi:10.1002/anie.201510796
62. Zhou L, Ma T, Li T, Ma X, Yin J, Jiang X. Dynamic Interpenetrating Polymer Network (IPN) Strategy for Multiresponsive Hierarchical Pattern of Reversible Wrinkle. *ACS Appl Mater Interfaces*. 2019;11(17):15977-15985. doi:10.1021/acsami.8b22216
63. van den Ende D, Kamminga J-D, Boersma A, Andritsch T, Steeneken PG. Voltage-Controlled Surface Wrinkling of Elastomeric Coatings. *Adv Mater*. 2013;25(25):3438-3442. doi:10.1002/adma.201300459
64. Wang Y, Xiao J. Programmable, reversible and repeatable wrinkling of shape memory polymer thin films on elastomeric substrates for smart adhesion. *Soft Matter*. 2017;13(31):5317-5323. doi:10.1039/c7sm01071k
65. Li W, Liu Y, Leng J. Harnessing Wrinkling Patterns Using Shape Memory Polymer Microparticles. *ACS Appl Mater Interfaces*. 2021;13(19):23074-23080. doi:10.1021/acsami.1c00623
66. SUN L, ZHAO Y, HUANG WM, PURNAWALI H, FU YQ. WRINKLING ATOP SHAPE MEMORY MATERIALS. *Surf Rev Lett*. 2012;19(02):1250010. doi:10.1142/S0218625X12500102
67. SUN L, WANG TX, BIN MOHD ZAKEE MHI, BIN ROSLI MS, LEE YX, HUANG WM. SELF-SURFACE WRINKLING ATOP ACRYLONITRILE BUTADIENE STYRENE (ABS) VIA HEATING-RESPONSIVE SHAPE MEMORY EFFECT. *Surf Rev Lett*. 2019;26(08):1950044. doi:10.1142/S0218625X19500446
68. Wang Y, Villada A, Zhai Y, et al. Tunable surface wrinkling on shape memory polymers with application in smart micromirror. *Appl Phys Lett*. 2019;114(19):1-6. doi:10.1063/1.5096767
69. Zhao L, Zhang L, Zhao J, et al. Engineering Surface Patterns with Shape Memory Polymers: Multiple Design Dimensions for Diverse and Hierarchical Structures. *ACS Appl Mater Interfaces*. 2019;11(1):1563-1570. doi:10.1021/acsami.8b15535
70. Hu J, Zhu Y, Huang H, Lu J. Recent advances in shape–memory polymers: Structure, mechanism, functionality, modeling and applications. *Prog Polym Sci*. 2012;37(12):1720-1763. doi:10.1016/j.progpolymsci.2012.06.001
71. Lendlein A, Gould OEC. Reprogrammable recovery and actuation behaviour of shape-memory polymers. *Nat Rev Mater*. 2019;4(2):116-133. doi:10.1038/s41578-018-0078-8
72. Behl M, Kratz K, Noechel U, Sauter T, Lendlein A. Temperature-memory polymer actuators. *Proc Natl Acad Sci U S A*. 2013;2013:1-5. doi:10.1073/pnas.1301895110
73. Westbrook KK, Mather PT, Parakh V, et al. Two-way reversible shape memory effects in a free-standing polymer composite. *Smart Mater Struct*. 2011;065010. doi:10.1088/0964-1726/20/6/065010
74. Wang K, Jia Y, Zhu XX. Two-Way Reversible Shape Memory Polymers Made of Cross-Linked Cocrystallizable Random Copolymers with Tunable Actuation Temperatures. *Macromolecules*. 2017;50(21):8570-8579. doi:10.1021/acs.macromol.7b01815
75. Behl M, Kratz K, Zotzmann J, Nöchel U, Lendlein A. Reversible Bidirectional Shape-

Memory Polymers. *Adv Mater*. 2013;25(32):4466-4469. doi:10.1002/adma.201300880
76. Gao Y, Liu W, Zhu S. Reversible Shape Memory Polymer from Semicrystalline Poly(ethylene- co -vinyl acetate) with Dynamic Covalent Polymer Networks. *Macromolecules*. 2018;51(21):8956-8963. doi:10.1021/acs.macromol.8b01724
77. Chen, YujieChen, ChiRehman HU. Shape-Memory Polymeric Artificial Muscles: Mechanisms, Applications and Challenges. *Molecules*. 2020;25(18):4246. doi:10.3390/molecules25184246
78. Yang G, Liu X, Tok AIY, Lipik V. Body temperature-responsive two-way and moisture-responsive one-way shape memory behaviors of poly(ethylene glycol)-based networks. *Polym Chem*. 2017;8(25):3833-3840. doi:10.1039/c7py00786h
79. Liang R, Yu H, Wang L, et al. Triple and Two-Way Reversible Shape Memory Polymer Networks with Body Temperature and Water Responsiveness. *Chem Mater*. 2021;33(4):1190-1200. doi:10.1021/acs.chemmater.0c03860
80. Sauter T, Lützow K, Schossig M, et al. Shape-Memory Properties of Polyetherurethane Foams Prepared by Thermally Induced Phase Separation. *Adv Eng Mater*. Published online May 24, 2012:n/a-n/a. doi:10.1002/adem.201200127
81. Altpeter H, Bevis MJ, Grijpma DW, Feijen J. Non-conventional injection molding of poly(lactide) and poly(epsilon-caprolactone) intended for orthopedic applications. *J Mater Sci Mater Med*. 2004;15(2):175-184. http://www.ncbi.nlm.nih.gov/pubmed/15330053
82. Saatchi M, Behl M, Lendlein A. Manufacturing and characterization of controlled foaming of single layers in bilayer constructs differing in pore morphology. *Macromol Symp*. 2013;334(1):33-39. doi:10.1002/masy.201300151
83. Saatchi M, Behl M, Lendlein A. Double layer porous structures by an injection molding/particulate leaching approach. *Macromol Symp*. 2014;346(1):100-107. doi:10.1002/masy.201400158
84. Chen Y, Chen C, Rehman HU, et al. Shape-Memory Polymeric Artificial Muscles: Mechanisms, Applications, and Challenges. *Molecules*. 2020;25(18):4246. doi:10.3390/molecules25184246
85. Kramschuster A, Turng L-S. An injection molding process for manufacturing highly porous and interconnected biodegradable polymer matrices for use as tissue engineering scaffolds. *J Biomed Mater Res B Appl Biomater*. 2010;92(2):366-376. doi:10.1002/jbm.b.31523
86. Ten E, Jiang L, Zhang J, Wolcott MP. Mechanical performance of polyhydroxyalkanoate (PHA)-based biocomposites. In: *Biocomposites*. Elsevier; 2015:39-52. doi:10.1016/B978-1-78242-373-7.00008-1
87. Kuang T, Chen F, Chang L, et al. Facile preparation of open-cellular porous poly (l-lactic acid) scaffold by supercritical carbon dioxide foaming for potential tissue engineering applications. *Chem Eng J*. 2017;307:1017-1025. doi:10.1016/j.cej.2016.09.023
88. Muñoz-Bonilla A, Fernández-García M, Rodríguez-Hernández J. Towards hierarchically ordered functional porous polymeric surfaces prepared by the breath figures approach. *Prog Polym Sci*. 2014;39(3):510-554. doi:10.1016/j.progpolymsci.2013.08.006
89. Karimi M, Heuchel M, Weigel T, Schossig M, Hofmann D, Lendlein A. Formation and size distribution of pores in poly(ε-caprolactone) foams prepared by pressure quenching using supercritical CO2. *J Supercrit Fluids*. 2012;61:175-190. doi:10.1016/j.supflu.2011.09.022
90. Harte AM, Namara JFM. Overinjection of thermoplastic composites I . Processing and

testing of components. *J Mater Process Technol*. 2007;182(1-3):12-20. doi:https://doi.org/10.1016/j.jmatprotec.2006.06.016.

91. Zhang X, Jiang G, Wu H, Guo S. Effect of the temperature gradient on the interfacial strength of polyethylene/polyamide 6 during the sequential injection molding. *High Perform Polym*. 2014;26(2):135-143. doi:10.1177/0954008313501531
92. Giusti R, Lucchetta G. Modeling the Adhesion Bonding Strength in Injection Overmolding of Polypropylene Parts. *Polymers (Basel)*. 2020;12(9):2063. doi:10.3390/polym12092063
93. Ho ST, Hutmacher DW. A comparison of micro CT with other techniques used in the characterization of scaffolds. *Biomaterials*. 2006;27(8):1362-1376. doi:10.1016/j.biomaterials.2005.08.035
94. Jenkins D, Salhadar K, Ashby G, et al. PoreScript: Semi-automated pore size algorithm for scaffold characterization. *Bioact Mater*. 2022;13:1-8. doi:10.1016/j.bioactmat.2021.11.006
95. Carmen M. González-Henríquez, Gonzalo E. Medel-Molina, Fernando E. Rodríguez-Umanzor, Claudio Terraza Inostroza, Mauricio A. Sarabia-Vallejos JR-H. Thermoresponsive microwrinkled hydrogel surfaces with modulated chemical composition. *Polymer (Guildf)*. 2021;231:124109. doi:https://doi.org/10.1016/j.polymer.2021.124109
96. Bai T, Liu J, Zhang W, Zou Z. Effect of surface roughness on the aerodynamic performance of turbine blade cascade. *Propuls Power Res*. 2014;3(2):82-89. doi:10.1016/j.jppr.2014.05.001
97. Wang Y, Xiao J. Confined thin film wrinkling on shape memory polymer with hybrid surface morphologies. *Acta Mech Sin*. 2021;37(7):1063-1071. doi:10.1007/s10409-021-01106-x
98. Yin J, Yagüe JL, Boyce MC, Gleason KK. Biaxially Mechanical Tuning of 2-D Reversible and Irreversible Surface Topologies through Simultaneous and Sequential Wrinkling. *ACS Appl Mater Interfaces*. 2014;6(4):2850-2857. doi:10.1021/am4054207
99. Li T, Huang Z, Suo Z, Lacour SP, Wagner S. Stretchability of thin metal films on elastomer substrates. *Appl Phys Lett*. 2004;85(16):3435. doi:10.1063/1.1806275
100. Lacour SP, Chan D, Wagner S, Li T, Suo Z. Mechanisms of reversible stretchability of thin metal films on elastomeric substrates. *Appl Phys Lett*. 2006;88(20):204103. doi:10.1063/1.2201874
101. Plank H, Güntner R, Scherf U, List EJW. The influence of the metal grain size on polymer/metal bilayer wrinkling. *Soft Matter*. 2007;3(6):713. doi:10.1039/b617211n
102. Wu K, Xia Y, Zhang DK, et al. Fatigue-free Cu films on wrinkled soft substrates. *Thin Solid Films*. 2022;746:139137. doi:10.1016/j.tsf.2022.139137
103. Luo X, Zhang B, Zhang G. Fatigue of metals at nanoscale: Metal thin films and conductive interconnects for flexible device application. *Nano Mater Sci*. 2019;1(3):198-207. doi:10.1016/j.nanoms.2019.02.003
104. Kraft O, Schwaiger R, Wellner P. Fatigue in thin films : lifetime and damage formation. *Mater Sci Eng A*. 2001;321:919-923.
105. Yu S, Sun Y, Li S, Ni Y. Harnessing fold-to-wrinkle transition and hierarchical wrinkling on soft material surfaces by regulating substrate stiffness and sputtering flux. *Soft Matter*. 2018;14(32):6745-6755. doi:10.1039/C8SM01287C
106. Saatchi M, Behl M, Nöchel U, Lendlein A. Copolymer networks from oligo (ε -

caprolactone) and n -butyl acrylate enable a reversible bidirectional shape-memory effect at human body temperature. *Macromol Rapid Commun*. 2015;36(10):880-884. doi:10.1002/marc.201400729

107. Genzer J, Groenewold J. Soft matter with hard skin: From skin wrinkles to templating and material characterization. *Soft Matter*. 2006;2(4):310. doi:10.1039/b516741h
108. DAHL-YOUNG KHANGHANQING JIANGYOUNG HUANGAND JOHN A. ROGERS. A Stretchable Form of Single-Crystal Silicon for High-Performance Electronics on Rubber Substrates. *Science (80-)*. 2006;311:208. doi:10.1126/science.11214
109. Uttayarat P, Toworfe GK, Dietrich F, Lelkes PI, Composto RJ. Topographic guidance of endothelial cells on silicone surfaces with micro- to nanogrooves: Orientation of actin filaments and focal adhesions. *J Biomed Mater Res Part A*. 2005;75A(3):668-680. doi:10.1002/jbm.a.30478
110. Chung JY, Youngblood JP, Stafford CM. Anisotropic wetting on tunable micro-wrinkled surfaces. *Soft Matter*. 2007;3(9):1163. doi:10.1039/b705112c
111. Cerda E, Mahadevan L. Geometry and Physics of Wrinkling. *Phys Rev Lett*. 2003;90(7):074302. doi:10.1103/PhysRevLett.90.074302
112. Breid D, Crosby AJ. Effect of stress state on wrinkle morphology. *Soft Matter*. 2011;7(9):4490. doi:10.1039/c1sm05152k
113. Ling Zhang, Weishan Yan, Naikun Gao, Wenyao Luo, Dongdong Zhang, Xi Li DL. Reversible strain-dependent properties of wrinkled Au/PDMS surface. *Mater Lett*. 2018;218:317-320. doi:https://doi.org/10.1016/j.matlet.2018.02.035
114. Wang Y, Xiao J. Programmable, reversible and repeatable wrinkling of shape memory polymer thin films on elastomeric substrates for smart adhesion. *Soft Matter*. 2017;13(31):5317-5323. doi:10.1039/c7sm01071k
115. Efimenko K, Rackaitis M, Manias E, Vaziri A, Mahadevan L, Genzer J. Nested self-similar wrinkling patterns in skins. *Nat Mater*. 2005;4(4):293-297. doi:10.1038/nmat1342
116. Fu C-C, Grimes A, Long M, et al. Tunable Nanowrinkles on Shape Memory Polymer Sheets. *Adv Mater*. 2009;21(44):4472-4476. doi:10.1002/adma.200902294
117. Cai S, Breid D, Crosby a. J, Suo Z, Hutchinson JW. Periodic patterns and energy states of buckled films on compliant substrates. *J Mech Phys Solids*. 2011;59(5):1094-1114. doi:10.1016/j.jmps.2011.02.001
118. Nöchel U, Kumar UN, Wang K, Kratz K, Behl M, Lendlein A. Triple-shape effect with adjustable switching temperatures in crosslinked poly[ethylene-co-(vinyl acetate)]. *Macromol Chem Phys*. 2014;215(24):2446-2456. doi:10.1002/macp.201400445
119. Yang P, Baker RM, Henderson JH, Mather PT. In vitro wrinkle formation via shape memory dynamically aligns adherent cells. *Soft Matter*. 2013;9(18):4705. doi:10.1039/c3sm00024a
120. Li J, An Y, Huang R, Jiang H, Xie T. Unique aspects of a shape memory polymer as the substrate for surface wrinkling. *ACS Appl Mater Interfaces*. 2012;4(2):598-603. doi:10.1021/am201727a
121. Becker S, Combeaud C, Fournier F, Rodriguez J, Billon N. Biaxial tension on polymer in thermoforming range. *EPJ Web Conf*. 2010;6:25003. doi:10.1051/epjconf/20100625003
122. Spaepen F. Interfaces and stresses in thin films. *Acta Mater*. 2000;48(1):31-42. doi:10.1016/S1359-6454(99)00286-4
123. Li B, Cao YP, Feng XQ, Gao H. Mechanics of morphological instabilities and surface

wrinkling in soft materials: A review. *Soft Matter*. 2012;8(21):5728-5745. doi:10.1039/c2sm00011c

124. Ou X, Cakmak M. Influence of biaxial stretching mode on the crystalline texture in polylactic acid films. *Polymer (Guildf)*. 2008;49(24):5344-5352. doi:10.1016/j.polymer.2008.09.053
125. Windischmann H. Intrinsic stress in sputter-deposited thin films. *Crit Rev Solid State Mater Sci*. 1992;17(6):547-596. doi:10.1080/10408439208244586
126. Chen A, Lieu DK, Freschauf L, et al. Shrink-film configurable multiscale wrinkles for functional alignment of human embryonic stem cells and their cardiac derivatives. *Adv Mater*. 2011;23(48):5785-5791. doi:10.1002/adma.201103463
127. Alves NM, Pashkuleva I, Reis RL, Mano JF. Controlling cell behavior through the design of polymer surfaces. *Small*. 2010;6(20):2208-2220. doi:10.1002/smll.201000233

Copolymer Networks From Oligo(ε-caprolactone) and *n*-Butyl Acrylate Enable a Reversible Bidirectional Shape-Memory Effect at Human Body Temperature

Mersa Saatchi, Marc Behl,* Ulrich Nöchel, Andreas Lendlein*

Exploiting the tremendous potential of the recently discovered reversible bidirectional shape-memory effect (rbSME) for biomedical applications requires switching temperatures in the physiological range. The recent strategy is based on the reduction of the melting temperature range (ΔT_m) of the actuating oligo(ε-caprolactone) (OCL) domains in copolymer networks from OCL and *n*-butyl acrylate (BA), where the reversible effect can be adjusted to the human body temperature. In addition, it is investigated whether an rbSME in the temperature range close or even above $T_{m,offset}$ (end of the melting transition) can be obtained. Two series of networks having mixtures of OCLs reveal broad ΔT_ms from 2 °C to 50 °C and from −10 °C to 37 °C, respectively. In cyclic, thermomechanical experiments the rbSME can be tailored to display pronounced actuation in a temperature interval between 20 °C and 37 °C. In this way, the application spectrum of the rbSME can be extended to biomedical applications.

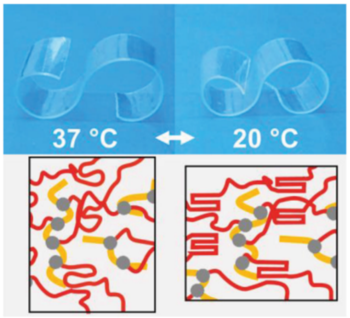

1. Introduction

The reversible bidirectional shape-memory effect (rbSME) was recently realized in polymer networks having crystallizable domains, which partially acted as actuator domains (AD) and partially as shifting-geometry determining domains (SGDs)[1–5] in semicrystalline polymer networks providing a broad melting temperature range (ΔT_m). Here, the assignment to ADs and SGDs was achieved by a thermomechanical programming procedure. The selection of a separation temperature (T_{sep}) within ΔT_m provided the feasibility to control the partial melting of the crystallizable domains and divided ΔT_m into an upper T_m range ($T > T_{sep}$) and a lower T_m range ($T < T_{sep}$). The crystallizable domains of the upper T_m range acted as SGD while the domains of the lower T_m range were assigned as AD. Once the temperature was increased to T_{sep}, the melting of the AD caused a melting-induced contraction (MIC) of the sample and when the temperature was decreased to T_{low}, crystallization-induced elongation (CIE) of the specimen was observed. However, all systems capable of rbSME reported so far required SGDs whose thermal transition was an

M. Saatchi, Dr. M. Behl, Dr. U. Nöchel, Prof. A. Lendlein
Institute of Biomaterial Science and Berlin-Brandenburg Center for Regenerative Therapies, Helmholtz-Zentrum Geesthacht, Kantstraße 55, 14513 Teltow, Germany
E-mail: marc.behl@hzg.de; andreas.lendlein@hzg.de
M. Saatchi, Prof. A. Lendlein
Institute of Chemistry, University of Potsdam, Karl-Liebknecht-Straße 24–25, 14476 Potsdam, Germany
M. Saatchi, Dr. M. Behl, Prof. A. Lendlein
Tianjin University–Helmholtz-Zentrum Geesthacht, Joint Laboratory for Biomaterials and Regenerative Medicine, Kantstraße 55, 14513 Teltow, Germany

Macromol. Rapid Commun. **2015**, DOI: 10.1002/marc.201400729

upper limit for the ADs. We have asked ourselves whether materials can be equipped with rbSME without providing SGDs. Additionally, in polymer systems capable of rbSME reported thus far, T_{sep} necessary to achieve a noticeable change in shape exceeded physiological relevant temperatures (i.e., 37 °C) as at least 42 °C were required, which hinders the utilization of the rbSME in biomedical applications.

The present study focuses on establishing 37 °C as T_{sep} for the rbSME in a polymer network and on exploring the upper ΔT_m region for utilization of T_{sep}. For doing so, at first, a material system with T_m = 37 °C has been targeted as a promising candidate material for exhibiting rbSME at body temperature, which would allow additionally to increase T_{sep} stepwise to $T_{m,offset}$ to determine the influence of the increased quantity of AD to the rbSME. As interesting finding, we detected reversible strain close to and even above $T_{m,offset}$ in thermomechanical tensile experiments, which inspired us to create an additional material system having $T_{m,offset}$ ≈37 °C. We hypothesized that when $T_{m,offset}$ would not be exceeded to large extent the orientation of the AD might be kept, similar to oriented melts.[6,7] This would permit to utilize the whole melting transition for the provision of ADs and in this way increase the reversible strain ε_{rev}. The second material system also exhibited reversible actuation between T_{low} and T_{sep} close to and above $T_{m,offset}$, where no crystalline SDG were present as the specimen was amorphous.

As a material basis for both material systems, we selected copolymer networks of *n*-butyl acrylate (BA) and oligo(ε-caprolactone) (OCL) prepared from diisocyanatoethyl dimethacrylate (OCLDIMA) acting as a chemical cross-linker, in which the crystalline domains of OCL act as switching segments.[2,8] We speculated that combining different molecular weights of OCL with $\bar{M}_n$ ranging from 2.3 to 15.2 kg mol^{-1} in polymer networks would result into a shift of the melting transition to lower temperature ranges, resulting from a hindered crystallization behavior of the domains provided by the OCL chain segments of higher $\bar{M}_n$ (Figure 1A).

Two series of homopolymer networks as well as copolymer networks of OCL and BA were synthesized providing a broad ΔT_m, in which the temperature of 37 °C was either within the ΔT_m or almost above ΔT_m. All polymer networks were characterized with respect to their gel content, degree of swelling, and thermal properties. In cyclic, thermomechanical experiments using a one-step initial programming followed by various heating–cooling cycles having different single T_{sep}s, the rbSME was quantified. Furthermore, in five subsequent heating–cooling cycles under stress-free conditions applying T_{sep} = 37 °C, the repeatability of the rbSME in the physiological relevant temperature interval was determined.

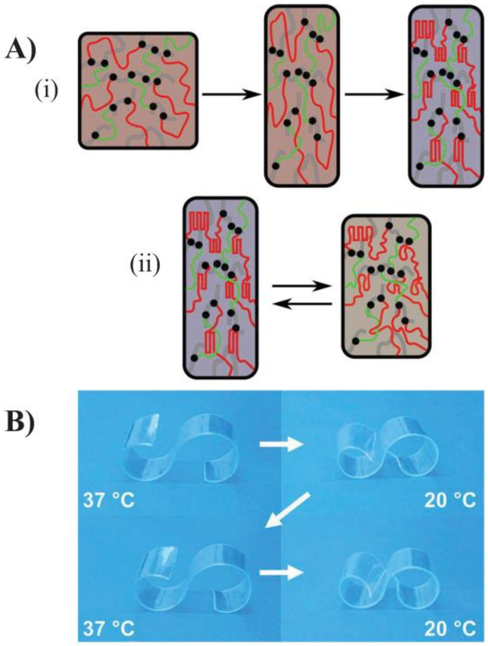

Figure 1. A) Schematic representation of the rbSME for copolymer networks with lower molecular weight (l$\bar{M}_n$) and high molecular weight (h$\bar{M}_n$) polymer chain segments: i) deformation at T_{high} = 60 °C and fixation T_{low} = 0 °C; ii) The rbSME is triggered by reversible crystallization and melting of oriented crystalline domains between T = 20 °C and T_{sep} = 37 °C. (red: h$\bar{M}_n$; green: l$\bar{M}_n$; black dots: chemical cross-links). B) Photo series presenting the reversible bidirectional shape-memory effect of C(2,15)B25 ribbon (70 mm × 15 mm × 0.5 mm). The reversibility was observed between an eight-shape (at 20 °C) and S-shape (at 37 °C).

2. Experimental Section

2.1. Materials

Oligo(ε-caprolactone) diols (OCL) with different number-average molecular weights of $\bar{M}_n$ = 2.3 kg mol^{-1}, $\bar{M}_n$ = 3.0 kg mol^{-1}, $\bar{M}_n$ = 3.8 kg mol^{-1}, and $\bar{M}_n$ = 7.5 kg mol^{-1} were purchased from Solvay Chemicals (Warrington, UK). Poly(ε-caprolactone) diol with $\bar{M}_n$ = 15.2 kg mol^{-1} was synthesized by ring-opening polymerization according to the procedure explained elsewhere.[9] End-group functionalization of all OCLs with 2-isocyanatoethyl methacrylate was performed according to the procedure described before.[10] *n*-butylacrylate (BA) was obtained from Sigma–Aldrich (St. Louis, MO, USA) and was purified using inhibitor-remover (Sigma–Aldrich, St. Louis, MO, USA).

2.2. Synthesis of the OCL Networks and OCL–BA Networks

Homopolymer networks of OCLs as well as copolymer networks of OCLs–BA having a mixture of OCL with different molecular weights were synthesized by melt blending of different of OCLs and BA at 80 °C. The mixtures were placed between two glass plates using a Teflon spacer with a thickness of 1 mm followed by photocuring for 1 h with a F300M (Fusion UV Systems, Gaithersburg, MD) system equipped with a high-pressure mercury lamp at a light intensity around 122 mW cm^{-1}. The first series of copolymer networks C(2,15)BX contained a mixture of OCLDIMA based on OCLs with $\bar{M}_n$ of 2.3 kg mol^{-1} and 15.2 kg mol^{-1} (1:1 wt%), while the second series of copolymer networks C(3,4,8)B*X* had a mixture of OCLDIMA based on OCLs with 3, 3.8, and 7.5 kg mol^{-1} (1:1:1 wt%). Here, *X* indicates the weight content of BA. In addition, homopolymer networks C(m)BX from OCLs used in the copolymer networks were synthesized, where m denotes the molecular weight of OCLs.

2.3. Characterization of the Networks

The obtained networks were characterized by determining the gel content (*G*) and the degree of swelling (*Q*) using chloroform as described elsewhere.[11] Thermal properties of all networks were determined by differential scanning calorimetry (DSC) on a calorimeter (Netzsch DSC204 Phoenix, Netzsch, Selb, Germany) from –100 °C to 100 °C with a heating rate of 10 K min^{-1}. Tensile tests were performed on a tensile tester Z1.0 (Zwick-Roell, Ulm, Germany) equipped with a thermo chamber and a temperature controller (Eurotherm e2408, Limburg, Germany) at 60 °C and a strain rate of 5 mm min^{-1}. The cross-link density (υ_c) was calculated based on the Mooney–Rivlin equation by employing the obtained stress–strain diagrams from tensile tests.[12,13]

Dynamic mechanical analysis (DMTA) was conducted on a Gabo Eplexor 25 N (Ahlden, Germany) using standard test specimen (ISO 527–2/1BB) for networks having BA compositions. All DMTA measurements were carried out in temperature sweep mode from –30 °C to 80 °C with a constant heating rate of 2 K min^{-1}. The oscillation frequency was 10 Hz and the storage modulus *E*′ was determined for 0 °C, 20 °C, and 37 °C.

2.4. Quantification of the rbSME

The rbSME of two copolymer networks was quantified by cyclic, thermomechanical tensile tests on the tensile tester as described before.

Variation of T_{sep}: Each measurement included an initial programming step applying a strain ε_{prog} = 40% at T_{high} = 60 °C and cooling to T_{low} = 0 °C at constant strain followed by subsequent reversible actuation cycles with different T_{sep}s ranging from 31 °C to 52 °C for C(2,15)B25 and from 28 °C to 40 °C for C(3,4,8)B25. Deformation fixation efficiency (Q_{ef}) was calculated according to Equation (1), where ε_A indicates the strain at T_{sep} and ε_{prog} indicates the programing strain (40%). In addition, the reversible strain (ε_{rev}) was determined by Equation (2), where l_B and l_A are the lengths of the specimen at T_{low} and T_{sep}, respectively.

$$Q_{ef} = \frac{\varepsilon_A}{\varepsilon_{prog}} \cdot 100 \tag{1}$$

$$\varepsilon_{rev} = \frac{l_B - l_A}{l_B} \cdot 100 \tag{2}$$

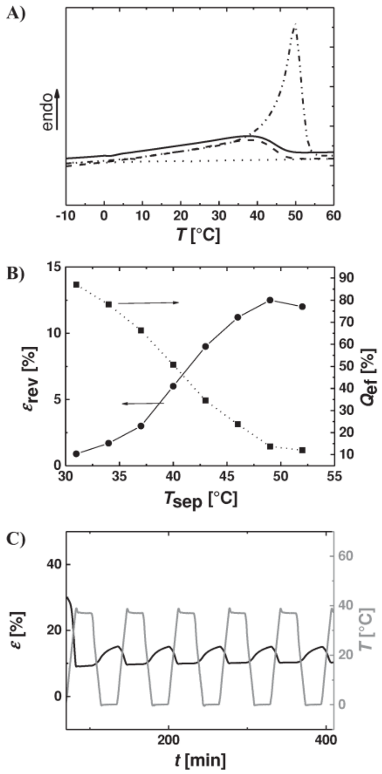

Figure 2. A) Contribution of different $\bar{M}_n$ of oligomers in networks to the shifting of the melting temperature peak and hindered crystallization; ‐·‐·‐·‐ C(15)B0; ······· C(2)B0; —— C(2,15)B0; ------ C(2,15)B25; B) Correlation between the reversible strain (ε_{rev}) and the deformation fixation efficiency (Q_{ef}) as a function of T_{sep} for C(2,15)B25. ■ Q_{ef}; ● ε_{rev}. C) Five actuation cycles of C) C(2,15)B25, where T_{sep} = 37 °C and T_{low} = 0 °C.

Constant T_{sep}: Same procedure as described above followed by subsequent reversible actuation cycles with constant T_{sep} = 37 °C for five cycles.

3. Results and Discussion

The possibility to shift the melting temperature peak (T_m) was investigated by means of DSC experiments on networks having different $\bar{M}_n$ of OCLs with $\bar{M}_n$ of 2.3 kg mol^{-1} C(2)B0 and 15.2 kg mol^{-1} C(15)B0 and having a mixture of $\bar{M}_n$ C(2,15)B0 as well as on a network C(2,15)B25 with 25 wt% BA content (Figure 2a). It was observed that although the C(2)B0 network with lower molecular weight (l$\bar{M}_n$) polymer chain segments showed no endotherm peak, the C(15)B0 network with higher molecular weight (h$\bar{M}_n$) polymer chain

Table 1. Characterization and mechanical properties of copolymer networks of C(2,15)B25 and C(3,4,8)B25.

Network	$2C_1 + 2C_2$[a)] [MPa]	υ_c[b)] [mol cm^{-3}]	E'[c)] [MPa]	E'[d)] [MPa]	E'[e)] [MPa]	E[f)] [MPa]	ε_b[g)] [%]
C(2,15)B25	1.60 ± 0.1	5.8×10^{-4}	44	31	24	3.9 ± 0.1	60 ± 10
C(3,4,8)B25	1.40 ± 0.2	5.2×10^{-4}	67	38	21	3.5 ± 0.3	55 ± 15

[a)]Mooney–Rivlin constants; [b)]Crosslink density calculated from the Mooney–Rivlin equation. (Estimation of error: 0.1×10^{-4} mol cm^{-3}); Storage modulus at [c)]0 °C; [d)]20 °C; [e)]37 °C (Estimation of error: 1 MPa); [f)]Young's modulus at 60 °C; [g)]Elongation at break at 60 °C.

segments exhibited a broad ΔT_m ranging from 2 °C to 57 °C, with T_m = 49 °C. Furthermore, by mixing OCLDIMAs comprising $l\bar{M}_n$ and $h\bar{M}_n$ in C(2,15)B0 crystallinity was reduced and ΔT_m ranged from 2 °C to 50 °C being T_m = 37 °C. This was attributed to the hindered crystallization of OCL with $h\bar{M}_n$ by the $l\bar{M}_n$, which could lead into a reduction of the melting endotherm and a shift of the T_m to lower temperatures (see for details, Table S1, Supporting Information, showing reduced crystallinity and crystal size, when the $l\bar{M}_n$ content was increased). This finding might indicate that OCL with $l\bar{M}_n$ interfere in the crystallization of OCL with $h\bar{M}_n$. Furthermore, the AB copolymer network of OCLs with 25 wt% of BA C(2,15)B25 showed further reduction of the melting endotherm, while the onset and offset of ΔT_m as well as T_m remained constant. C(2,15)B25 as well as networks without BA content (see for details Table S1, Supporting Information) were characterized by means of G and Q. C(2,15)B25 showed 95 ± 2% gel content and 660 ± 10% degree of swelling in chloroform. Values of the gel content for all networks ranged from 94% to 98% indicating an almost complete cross-linking reaction. In addition, υ_c was determined based on Mooney–Rivlin analysis and the mechanical properties of the network C(2,15)B25 were investigated by means of DMTA and tensile tests at 60 °C. Results are presented in Table 1.

C(2,15)B25 was explored for implementation and quantification of the rbSME by thermomechanical tensile tests as described in the experimental part and as shown schematically in Figure 1A. In a first experiment, in which ε_{prog} = 40% was selected, ε_{rev} and Q_{ef} were determined as function of T_{sep} (Figure 2b). ε_{rev} increased from 1.1 ± 0.1% to 12.5 ± 0.1% by increasing T_{sep} from 31 °C to 52 °C for the network C(2,15)B25. In addition, Q_{ef} was decreased from 87 ± 4% to 12 ± 1%. Moreover C(2,15)B25 exhibited a rbSME compatible with physiological temperature, where an identical reversible strain was observed during stress-free heating–cooling cycles (Figure 2c) when T_{sep} was kept constant at 37 °C.

Referring to the working principle of the rbSME, an increased quantity of AD between T_{low} and T_{sep} of C(2,15)B25 resulted in an increase of ε_{rev}. Surprisingly, the maximum ε_{rev} = 12.5 ± 0.1% was observed at 49 °C, where T_{sep} was close to the $T_{m,offset}$. By increasing T_{sep} to 52 °C (located after $T_{m,offset}$), ε_{rev} was 12.1 ± 0.1% and Q_{ef} was constant. This indicated that the ADs could be kept oriented in the viscoelastic state. We attributed this effect to the orientational memory, which was observed for oriented melts and resulted in oriented re-crystallization of crystalline domains upon cooling.[6,7] The conservation of the orientation was reflected by a non-zero Q_{ef} at $T_{sep} \geq T_{m,offset}$, and this way oriented crystallization of the ADs resulted in increased ε_{rev}.

To confirm the principle of preserving oriented ADs via orientational memory, a C(3,4,8)BA25 network having mixtures of OCLs with $\bar{M}_n$ of 3, 3.8, and 7.5 kg mol^{-1} with 25 wt% BA was synthesized. Q and G of C(3,4,8)BA25 was 98 ± 1% and 620 ± 10%, respectively, and the mechanical properties of this polymer network are reported in Table 1. The second DSC heating run revealed a broad ΔT_m ranging from −10 °C to 37 °C and T_m = 28 °C (Figure 3a). The rbSME was quantified for C(3,4,8)B25 by determining ε_{rev} and Q_{ef} as a function of T_{sep} (Figure 3b). C(3,4,8)B25 exhibited the highest value of ε_{rev} = 17.1 ± 0.1% for T_{sep} = 37 °C and when T_{sep} was increased from 28 °C to 40 °C, Q_{ef} was reduced from 77 ± 1% to 15 ± 1%. Furthermore, C(3,4,8)B25 likewise revealed a rbSME compatible with the human body temperature (Figure 3c) with an identical reversible strain during stress-free heating–cooling cycles for constant T_{sep} = 37 °C by utilizing orientational memory of the ADs to enhance ε_{rev} during actuation.

The differences in rbSME of both copolymer networks under identical conditions (constant T_{sep} = 37 °C) were attributed to the contribution of different crystallization kinetics for different chain lengths of OCL in the networks and will be subject of a more detailed investigation in the future.

From in situ X-ray scattering measurements on programmed samples (see for details Figure S1, Supporting Information), a degree of crystallinity (DOC) of 24% at T_{low} = 0 °C was observed for C(3,4,8)B25, which was amorphous at T_{sep} = 37 °C. A DOC = 22% at T_{low} = 0 °C and 7% at T_{sep} = 37 °C for C(2,15)B25 was determined. The increased difference in DOC between T_{low} and T_{sep} of C(3,4,8)B25 was related to an increased quantity of AD, which resulted in increased ε_{rev}.

Motivated by the promising results from the thermomechanical tensile tests, it was explored whether the rbSME could be conducted in a temperature interval between room temperature (T_{low} = 20 °C) and body temperature (T_{sep} = 37 °C). Figure 1b shows a series of photographs of

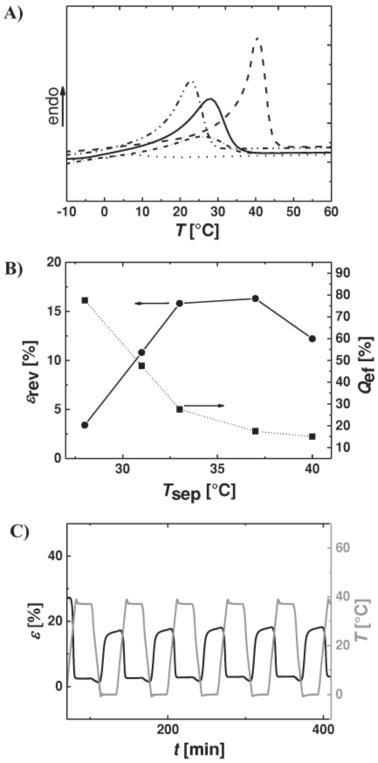

Figure 3. A) Contribution of different $\bar{M}_n$ of oligomers to the shifting of the melting temperature peak and hindrance crystallization; ······· C(3)B0; -·-·-·-·- C(4)B0; ----- C(8)B0; —— C(3,4,8)B0; -··-··- C(3,4,8)B25; B) Correlation between the reversible strain (ε_{rev}) and the deformation fixation efficiency (Q_{ef}) as a function of T_{sep} for A) C(3,4,8)B25. ■ Q_{ef}; ● ε_{rev}. C) Five actuation cycles of C) C(3,4,8)B25, where T_{sep} = 37 °C and T_{low} = 0 °C.

a ribbon of C(2,15)B25, in which the specimen could shift repeatedly between an open S-shape and a closed eight-shape. In this way, the rbSME could be realized for the first time in a temperature interval relevant for biomedical applications, e.g., devices for external short-term applications such as bandages or temporary fixation parts, where the rbSME would be activated upon exposure to human body temperature. The rbSME could further be utilized in gerontechnology for home-care products or active devices to support the daily life of disabled or elderly people.

4. Conclusion

Copolymer networks prepared from BA and mixtures of crystallizable OCLDIMA of various $\bar{M}_n$ permitted the implementation of a rbSME around body temperature. The C(2,15)B25 network contained a mixture of OCL with $\bar{M}_n$ of 2.3 and 15.2 kg mol^{-1} and 25 wt% BA, while a C(3,4,8) B25 network consisted of a mixture of $\bar{M}_n$ of 3, 3.8, and 7.5 kg mol^{-1} and 25 wt% BA. DSC revealed broad ΔT_ms for both networks from 2 °C to 57 °C and T_m at 49 °C for C(2,15) B25 and from −10 °C to 37 °C and T_m at 28 °C for C(3,4,8) B25. The rbSME was quantified in thermomechanical tensile tests by examining the correlation between reversible strain (ε_{rev}) and fixation efficiency (Q_{ef}). Also, it was found that not only crystalline SGD domains could preserve oriented ADs, but also an orientational memory of the molten ADs when exceeding $T_{m,offset}$ resulted in reversible actuation of the copolymer networks. In this way, technology of the rbSME could be adjusted towards a temperature range relevant for biomedical applications and potential applications such as reversible closure systems for shoes and clothes for handicapped people or reversible folding guides for nerve electrodes[14] can be anticipated.

Supporting Information

Supporting Information is available from the Wiley Online Library or from the author.

Received: December 18, 2014; Revised: February 5, 2015; Published online: ; DOI: 10.1002/marc.201400729

Keywords: body temperature; broad melting temperature range; orientational memory; reversible bidirectional shape-memory polymer; copolymer networks

[1] M. Behl, K. Kratz, J. Zotzmann, U. Nöchel, A. Lendlein, *Adv. Mater.* **2013**, *25*, 4466.
[2] M. Behl, K. Kratz, U. Noechel, T. Sauter, A. Lendlein, *Proc. Natl. Acad. Sci. USA* **2013**, *110*, 12555.
[3] T. Xie, J. J. Li, Q. Zhao, *Macromolecules* **2014**, *47*, 1085.
[4] J. Zhou, S. A. Turner, S. M. Brosnan, Q. X. Li, J. M. Y. Carrillo, D. Nykypanchuk, O. Gang, V. S. Ashby, A. V. Dobrynin, S. S. Sheiko, *Macromolecules* **2014**, *47*, 1768.
[5] A. Basit, G. L'Hostis, M. J. Pac, B. Durand, *Materials* **2013**, *6*, 4031.
[6] Y. P. Khanna, A. C. Reimschuessel, *J. Appl. Polym. Sci.* **1988**, *35*, 2259.
[7] N. Stribeck, U. Noechel, A. Almendarez Camarillo, S. V. Roth, M. Dommach, P. Boesecke, *Macromolecules* **2007**, *40*, 4535.
[8] A. Lendlein, A. M. Schmidt, R. Langer, *Proc. Natl. Acad. Sci. USA* **2001**, *98*, 842.
[9] A. Lendlein, P. Neuenschwander, U. W. Suter, *Macromol. Chem. Phys.* **2000**, *201*, 1067.
[10] U. N. Kumar, K. Kratz, W. Wagermaier, M. Behl, A. Lendlein, *J. Mater. Chem.* **2010**, *20*, 3404.
[11] H. Lange, *Colloid. Polym. Sci.* **1986**, *264*, 488.
[12] M. Mooney, *J. Appl. Phys.* **1940**, *11*, 582.
[13] T. Ha-Anh, T. Vu-Khanh, *Polym. Test* **2005**, *24*, 775.
[14] J. Reeder, M. Kaltenbrunner, T. Ware, D. Arreaga-Salas, A. Avendano-Bolivar, T. Yokota, Y. Inoue, M. Sekino, W. Voit, T. Sekitani, T. Someya, *Adv. Mater.* **2014**, *26*, 4967.

Macromolecular
Journals

Supporting Information

for *Macromol. Rapid Commun.*, DOI: 10.1002/marc.201400729

Copolymer Networks From Oligo(ε -caprolactone) and n -Butyl Acrylate Enable a Reversible Bidirectional Shape-Memory Effect at Human Body Temperature

Mersa Saatchi , Marc Behl ,* Ulrich Nöchel , Andreas Lendlein*

Supporting Information

for *Macromol. Rapid Commun.*, DOI: 10.1002/marc.201400729

Copolymer Networks From Oligo(ε-caprolactone) and n-Butyl Acrylate Enable a Reversible Bidirectional Shape-Memory Effect at Human Body Temperature

Mersa Saatchi, Marc Behl*, Ulrich Nöchel, and Andreas Lendlein*

Supporting Table S1. Contribution of different chain length segments to the crystallization of polymer networks at different temperatures as determined by WAXS (non-programmed samples).

Network ID	G[a] [%]	Q[b] [%]	ΔH_m[c] [J·g^{-1}]	T = 0 °C	
				DOC[d] [%]	l_c[e] [nm]
C(2)B0	98 ± 1	390± 10	0	0	0
C(15)B0	97 ± 1	860 ± 10	60	44.5 ± 1.4	14.7 ± 0.2
C(2,15)B0[f]	97 ± 2	540 ± 20	22	26.1 ± 0.8	12.7 ± 0.2
C(2,15)B0[g]	94 ± 2	630 ± 40	9	7.7 ± 0.3	11.3 ± 0.2
C(2,15)B25	95 ± 2	620 ± 20	27	17.3 ± 1.1	12.5 ± 0.2
C(3)B0	99 ± 1	450 ±10	3	0*	0*
C(4)B0	99 ± 1	500±10	40	20.4 ± 1.2	10.1 ± 0.2
C(8)B0	98 ± 1	640±10	50	25.6 ± 0.4	14.4 ± 0.2
C(3,4,8)B0[h]	98 ± 1	530±10	40	25.5 ± 0.1	10.8 ± 0.2
C(3,4,8)B25	98 ± 1	620±10	27	16.3 ± 1.1	11.1 ± 0.2

[a] Gel content; [b] Degree of swelling in chloroform; [c] Melting enthalpy calculated from second DSC heating run; [d] Degree of crystallinity determined from WAXS; [e] Average lateral crystal size determined from WAXS; [f] The network included a mixture of OCLs with M_n = 2.3 kg·mol^{-1} and M_n = 15.2 kg·mol^{-1} (1:1 wt%); [g] The network included a mixture of OCLs with M_n = 2.3 kg·mol^{-1} and M_n = 15.2 kg·mol^{-1} (3:1 wt%); [h] The network included a mixture of OCLs with M_n = 3, 3.8, 7.5 kg·mol^{-1} (1:1:1 wt%).* WAXS crystallinity was not detectable even the DSC showed 3 J·g^{-1}.

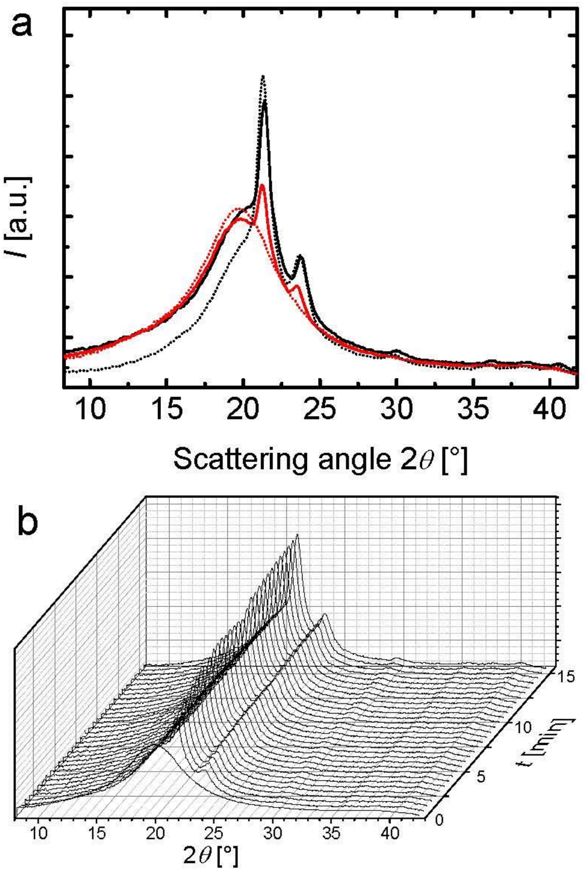

Supporting Figure S1: Wide-angle scattering curves of **a)** C(2,15)B25 (solid lines) at 0 °C (black) (DOC = 22%) and 37 °C (red) (DOC = 7%) as well as C(3,4,8)B25 (dotted lines) at 0 °C (black) (DOC = 24%) and 37 °C (red) (amorphous) recorded *in situ* during rbSME. **b)** Isothermal crystallization of C(3,4,8)B25 at 0 °C for 15 min.

Supporting Method Wide-Angle X-Ray Scattering (WAXS)

An X-ray diffractometer D8 Discover from Bruker AXS (Karlsruhe, Germany) was used for measurements in transmission geometry. The generator was operated at 40 kV and 40 mA on a copper-anode. The collimator was chosen 0.8 mm (beam size). The two-dimensional detector (Hi-Star) was operated in 1024*1024 pixel mode. The distance sample-detector was 150 mm and the wavelength $\lambda = 0.15418$ nm. The detector was positioned at an angular position $2\theta = 25°$ in order to cover an angular range from $2\theta = 7.2°$ to 43.5°.

An integration of the whole 2θ-range was performed in order to obtain 1D-scattering curves using 5-point normalized binning. Non valid data points outward of the detector were not considered (masked) for integration. The scattering curve was decomposed into individual peaks, belonging either to the amorphous or the crystalline phase using the Bruker-software TOPAS®. The peaks of the two phases (amorphous and crystalline) were fitted with Pearson VII functions. The relationship of the integrated areas determines the degree of crystallinity (DOC).